UNIVERSITY OF CALIFORNIA, SAN DIEGO

Some aspects of the structure and magnetization of the oceanic crust

A dissertation submitted in partial satisfaction of the
requirements for the degree
Doctor of Philosophy

in

Earth Sciences

by

Roi Granot

Committee in charge:

Steve C. Cande, Chair
Jeffrey S. Gee, Co-Chair
Donna K. Blackman
David A. Holway
Lisa Tauxe

2009

The dissertation of Roi Granot is approved, and it is acceptable in quality and form for publication on microfilm and electronically:

_____

_____

_____

_____
Co-Chair

_____
Chair

University of California, San Diego

2009

TABLE OF CONTENTS

LIST OF FIGURES

LIST OF TABLES

ACKNOWLEDGEMENTS

I would like to thank my advisors, Steve, Jeff, and Lisa, for their exceptional mentoring and support throughout my studies here at Scripps. Steve provided his time, patience, insights, modest approach, and has served as an excellent mentor. Jeff has patiently taught me endlessly on essentially everything. Jeff also gave his inspiration for many of the ideas presented in this dissertation. Lisa has been insightful, generous, enthusiastic, and a great friend. Lisa also gave me the initial opportunity to study at Scripps, a life-changing experience! They gave me the freedom to pursue my interests and ideas. They have also taught me how to be thorough and skeptical, yet still maintaing the initial scientific enthusiasm. I feel extremely lucky that I had the opportunity to learn under the guidance of these wonderful scientists and mentors. Donna was helpful and supportive along the way. I thank David for serving as a member of the committee.

I have had the opportunity to work with Joann Stock (Caltech), and greatly appreciate her generous help, and the opportunity to cross the southern ocean twice with her. Fred Davey (GNS, New Zealand) gave his advise on the interpretation of the seismic reflection data as well as the tectonics of the West Antarctic rift System. Chris Sorlien (UCSB) introduced me to advanced seismic processing techniques. I am also thankful for the help of Neal Driscoll for the insightful discussions we had on rifting and seismic stratigraphy. Bob Parker has been helpful in providing help with inversion codes. I am also thankful to Paul Henkart for his continuous support and help with SIOSEIS which helped tremendously on-board the Palmer (cruise NBP0701) and post-cruise processing.

I was fortunate to share my office with Julie Bowles, Kurt Schwehr, Ritayan Mitra, and Geoff Cromwell with whom I learned and shared many delightful moments. I thank Marcel Croon for many interesting discussions and help in maintaining many softwares and datasets. Thanks goes to Jason Steindorf for the help in lab. Other fellow students (and post-doc) who were great friends include Leah, Robin, Danny, Yariv, and many others.

Big thank you goes out to the UC Ship Funds program who gave me the opportunity to lead an expedition across the North Pacific the, R/V Melville. The

results from this cruise provided me with the data that enabled me to successfully complete the second chapter of this dissertation. I thank Bruce Appelgate, Elizabeth Rios, Rose Dufour, Graziella Bruni, and the crew aboard R/V Melville (cruise MGLN44MV) for their great support. Support from the Earth section enabled me to invite and create a helpful scientific party.

My research has been funded by grants from the National Science Foundation. I also thank the Earth Sciences department at the University of California, San Diego for supporting my teaching assistantships. Funding was also provided by the Graduate department at Scripps.

My family, located over on the other side of the planet, supported me in every way they could. I am lucky to be a member of this family and thankful for all the help and support. Last, but not least, much deserved thank you goes out to my beloved partner for life, my wife Efrat and our Eitani and Ilaichuck.

Chapter 1, in full, is a reprint of the material as it appears in *Earth and Planetary Science Letters*, R. Granot, L. Tauxe, J. S. Gee, and H. Ron, A view into the Cretaceous geomagnetic field from analysis of gabbros and submarine glasses, 256, 1-11, 2007. I collected, processed, and interpreted all of the data in this chapter. Lisa Tauxe provided significant advice on laboratory methods, data interpretation, and analysis. Jeff Gee provided continuous advice. Sampling in the field was carried out by myself and Hagai Ron.

Chapter 2, in full, is a reprint of the material as it appears in *Earth and Planetary Science Letters*, R. Granot, S. C. Cande, and J. S. Gee, The implications of long-lived asymmetry of remanent magnetization across the North Pacific fracture zones, doi:10.1016/j.epsl.2009.10.017, 2009. I have led the collection of the new and archival data. I also calculated all forward and inverse modeling, and interpreted the results. Steve Cande and Jeff Gee provided codes for the two- and three-dimensional forward and inverse modeling and gave continuous advise.

Chapter 3 is being prepared for submission to *Geochemistry, Geophysics,*

Geosystems, R. Granot, S. C. Cande, J. M. Stock, F. J. Davey, R. W. Clayton, Post-spreading rifting in the Adare Basin, Antarctica: Regional Tectonic Consequences. I processed, interpreted, and analyzed all of the seismic reflection data. I also picked the anomalies from the aeromagnetic dataset collected as part of GANOVEX IX 2005/06 (courtesy of Detlef Damaske). Principal investigators were Steve Cande and Joann Stock who also supervised this study. Fred Davey contributed to the seismic interpretation and general tectonic understanding. Rob Clayton helped processing the seismic data during the NBP0701 cruise.

VITA

2002	B.S. in Geology, Hebrew University of Jerusalem, Israel
2003-2004	M.S. in Geology *cum laude*, Hebrew University of Jerusalem, Israel
2004-2009	Graduate Student Researcher, Scripps Institution of Oceanography, University of California, San Diego
2009	Ph.D., Scripps Institution of Oceanography, University of California, San Diego

PUBLICATIONS

Granot, R., Abelson, M., Ron, H., and Agnon, A., The oceanic crust in 3D: Paleomagnetic reconstruction in the Troodos ophiolite gabbro, *Earth and Planetary Science Letters* 251, 280-292, 2006.

Granot, R., Tauxe, L., Gee, J. S., and Ron, H., A view into the Cretaceous geomagnetic field from analysis of gabbros and submarine glasses, *Earth and Planetary Science Letters*, 256, 1-11, 2007.

Granot, R., Cande S. C., Stock, J. M., Clayton, R. W., and Davey, F. J., Beyond seafloor spreading: Neogene deformation and volcanism in the Adare Basin, in A Keystone in a Changing World - Proceedings for the 10th International Symposium on Antarctic Earth Sciences: U.S.G.S., 2007.

Granot, R., Cande, S. C., Gee, J. S., The implications of long-lived asymmetry of remanent magnetization across the North Pacific fracture zones, *Earth and Planetary Science Letters*, doi:10.1016/j.epsl.2009.10.017, 2009.

ABSTRACT OF THE DISSERTATION

Some aspects of the structure and magnetization of the oceanic crust

by

Roi Granot

Doctor of Philosophy in Earth Sciences

University of California, San Diego, 2009

Steve C. Cande, Chair
Jeffrey S. Gee, Co-Chair

The structure and magnetization of the oceanic crust reflect its tectonic and magmatic evolution since its initial formation. The magnetization of the crust also provides a record of the polarity reversals and strength of the Earth's geomagnetic field. In this dissertation I first describe absolute paleointensity measurements made on gabbroic rocks collected from the lower oceanic crust of the Troodos ophiolite, Cyprus. The resultant data-set provides a view into the the geomagnetic field during the end of the Cretaceous normal polarity superchron (CNS, 120.6 to 83 million years ago). This data-set is then compared to the locally and globally existing data and predictions made by geodynamo numerical simulations. The results hint that the geomagnetic field had similar properties during times of frequent reversals and times of stable polarity. The second chapter of this dissertation is focused on the marine magnetic anomalies observed across the North Pacific fracture zones. Here I analyze archival and newly collected magnetic anomaly and bathymetric profiles measured across three fracture zones in the Cretaceous Quiet Zone (CNS in age). Forward and inverse modeling indicate that these anomalies

arise from remanent magnetization, with enhanced remanence located on one side of each fracture zone. These long-duration enhanced zones require some long-lived asymmetry in crustal construction processes near ridge-transform intersections. The calculated magnetization contrasts provide long-term constraints on the properties of the geomagnetic field during the Cretaceous superchron. Finally, using seismic reflection and magnetic anomaly grids collected in the Adare Basin, Antarctica, I explore the kinematic evolution of the West Antarctic rift system during the Neogene. Correlation of the Adare seismic sequence to the closest drill-holes and the Ross Sea seismic stratigraphy establishes the temporal framework of three regional tectonic events. Overall, minimal but significant extensional activity took place in the Adare Basin after seafloor spreading stopped. Comparison of the results with observations from the central and southern parts of the rift system suggests that a major change in plate motion took place in the middle miocene.

Chapter 1
A view into the Cretaceous geomagnetic field from analysis of gabbros and submarine glasses

Available online at www.sciencedirect.com
ScienceDirect
ELSEVIER
Earth and Planetary Science Letters 256 (2007) 1 – 11
EPSL
www.elsevier.com/locate/epsl

A view into the Cretaceous geomagnetic field from analysis of gabbros and submarine glasses

Roi Granot [a,*], Lisa Tauxe [a], Jeffrey S. Gee [a], Hagai Ron [b]

[a] *Scripps Institution of Oceanography, La Jolla, CA 92093, USA*
[b] *Institute of Earth Sciences, Hebrew University of Jerusalem, Jerusalem 91904, Israel*

Received 14 August 2006; received in revised form 23 December 2006; accepted 24 December 2006
Available online 5 January 2007
Editor: M.L. Delaney

Abstract

The nature of the geomagnetic field during the Cretaceous normal polarity superchron (CNS) has been a matter of debate for several decades. Numerical geodynamo simulations predict higher intensities, but comparable variability, during times of few reversals than times with frequent reversals. Published geomagnetic paleointensity data from the CNS are highly scattered suggesting that additional studies are required. Here we present new paleointensity results from 18 sites collected from the lower oceanic crust of the Troodos ophiolite, Cyprus (92.1 Ma old). Together with recently published data from the Troodos upper crust we obtain three independent paleointensity time-series. These sequences reveal quasi-cyclic variations of intensities about a mean value of 54±20 Z Am^2, providing insight into the fluctuating nature of the Cretaceous magnetic field. Our data suggest the CNS field was both weaker and more variable than predicted by geodynamo simulations. The large amplitudes of these variations may explain the wide range of dipole moments previously determined from the CNS.

Keywords: Cretaceous normal polarity superchron; paleointensity; Troodos ophiolite; paleomagnetism; geomagnetic field

1. Introduction

Convection within the liquid metal outer core is believed to generate the geomagnetic field [1]. Recent geodynamo numerical simulations have shown that heat flux distribution at the core–mantle boundary has a profound influence on the efficiency of convection within the core and therefore, on the character of the magnetic field [2,3]. In particular, the simulations predict that prolonged features in the history of the field, such as long times of stable polarity (superchrons), are controlled by the lower mantle thermal structure and ought to correspond with a high efficiency dynamo. They also predict that superchrons would be associated with an elevated dipole moment but comparable variability relative to times of high reversal frequency [2]. These predictions can be tested using geomagnetic paleointensity data from the Cretaceous normal polarity superchron (CNS, 120.6 to 83 Ma [4,5]).

Studies of the CNS using both volcanic and sedimentary rocks have lead to strikingly different conclusions regarding the strength and variability of the geomagnetic field (e.g., [6–15]). Some studies suggest rather low average moments (17 Z (10^{21}) Am^2 [6,7]) while others have moments as high as 190 Z Am^2

* Corresponding author.
E-mail address: rgranot@ucsd.edu (R. Granot).

0012-821X/$ - see front matter © 2007 Elsevier B.V. All rights reserved.
doi:10.1016/j.epsl.2006.12.028

[8–10]. This range of dipole moments is similar to that observed during the Cenozoic, a time with high reversal frequency [16]. Moreover, some studies have suggested low variability of the field (10% of the mean, [17]) while others displayed substantially higher variability (55% of the mean, [10]).

The controversy regarding the nature of the geomagnetic field during the CNS could result either from inadequate sampling of the field [13] or from unreliable data, or both. However, there is now a rather large body of published data, much of which conforms to the highest experimental standards. The current debate therefore revolves around selection criteria and the reliability of various recording media [18].

One heretofore unavailable tool to assess the reliability of absolute paleointensity data in the CNS is the degree to which sequential data points display serial correlation. Several sedimentary relative paleointensity records have been produced [14,15], but time-series of absolute paleointensity data from the CNS have not been available and in fact are difficult to obtain. If such a serial correlation could be demonstrated, the geomagnetic origin of the observed variation, as opposed to "noise" would be strongly supported. The magnetization of the oceanic crust as evidenced in magnetic anomaly amplitudes [19–21] may provide a means of obtaining geomagnetic intensity fluctuations but such data are presently insufficient for the CNS. Here we examine paleointensity variations in samples from the oceanic crust exposed in the Troodos ophiolite.

The Troodos ophiolite on the island of Cyprus offers a remarkable exposure of a portion of the oceanic crust dated with uranium–lead as being late Cretaceous in age (92.1 Ma, [22]). Extensive normal faulting and hydrothermal massive sulfide bodies exposed across most of the ophiolite are consistent with crustal formation at a slow to intermediate spreading center (full spreading rate of 20–75 mm/yr) [23–27]. The lower oceanic crust within this kind of spreading environment typically comprises discrete, short-lived, magma bodies (i.e., cooling units) [28].

The Troodos ophiolite comprises a complex tectonic framework with several ancient spreading axes penetrating into previously existing crust [29,30] (Fig. 1). The locations of the fossil spreading axes, representing the youngest rocks, are constrained by several independent structural observations. Blocks of sheeted dikes with opposite tilt and axial extensional faults mark the upper crustal exposure of the spreading axes [29,31]. The location of the spreading axis in the lower crust is more difficult to establish. Granot et al. [32] delineate the axis in the lower crust by using remanence data to identify lower crustal blocks that are decoupled from the upper crust. The chronological relations between the different structural domains are poorly constrained, but within a single domain lower crustal samples can be placed in a relative temporal framework using distance from the inferred spreading center as a proxy for the arrow of time. Moreover, there are several pseudo-stratigraphic sections through

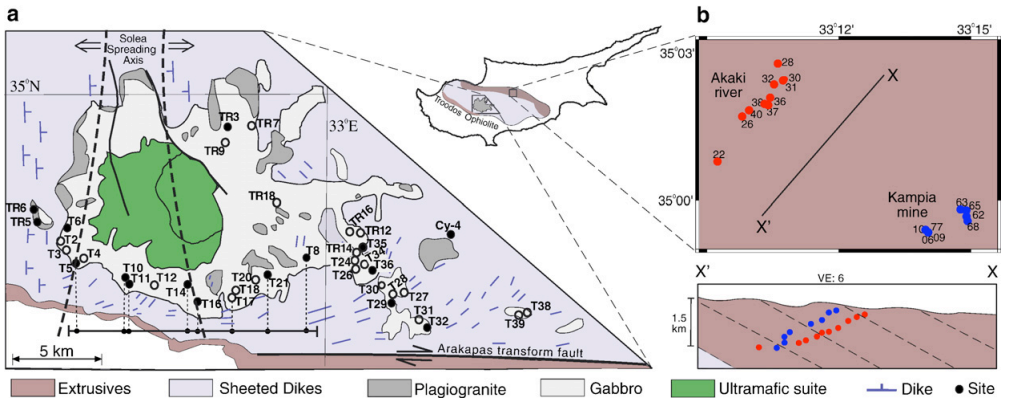

Fig. 1. Sampling sites from the Troodos ophiolite, Cyprus. (a) Gabbro sampling sites within the central intrusive suite. Heavy dashed lines and arrows indicate the location of the paleospreading axis and spreading direction, respectively. The axial location is inferred where minor lower crustal rotations occurred [32]. Solid (open) circles are the successful (unsuccessful) paleointensity sites. The fine dashed lines indicate the projections used to determine the distance of successful paleointensity sites along a flow line (shown in Fig. 3a). Distance along the flow-line is measured from the center of the Solea spreading axis. (b) Glass sampling sites (top) [10], and a schematic cross section through the extrusive sampled section (bottom). Their corresponding paleointensity time-series are shown in Fig. 3a.

the upper crust that also allow temporal ordering of cooling units.

For a time-series through the lower crust, we seek a coherent slice of gabbro in which relative age is well constrained. Deformation of the upper crust sheeted dikes [33,31] and rotations within the lower crust [32] imply that a coherent slice of crust is exposed near the intersection of the Solea spreading center and the Arakapas transform fault (Fig. 1). This slice contains the Solea spreading axis and extends some 6 km to the east (remanence data from lower crustal samples east of this slice (Granot, unpublished data) suggest that these eastern sites formed within a different spreading environment). Exposures of the gabbros parallel to the spreading direction within this coherent slice offer the possibility of constructing a temporal record of the Cretaceous geomagnetic field. Although the spatial variability of magma injection in the accretion zone [28] limits the temporal resolution, the distance of the gabbro sites from the spreading axis should provide an approximate temporal order. Here we consider only intensity variations in these gabbros; variations in remanence directions have been discussed by [32].

A second opportunity for temporal ordering is in the exposures of the upper crust in the Akaki Canyon and the Kampia mine area (Fig. 1). Tauxe and Staudigel [10] presented a large collection of data from these sections which we re-examine in terms of their spatio/temporal relationships.

In this study we present new data from 221 gabbroic samples obtained from 35 sites in the lower Troodos crust (Fig. 1), many of which can be located with respect to the ancient spreading center, and hence form a time-series. The Cyprus drilling project, CY-4, provides 12 additional sampling units of gabbroic material which contribute to the data set as a whole, but which cannot be

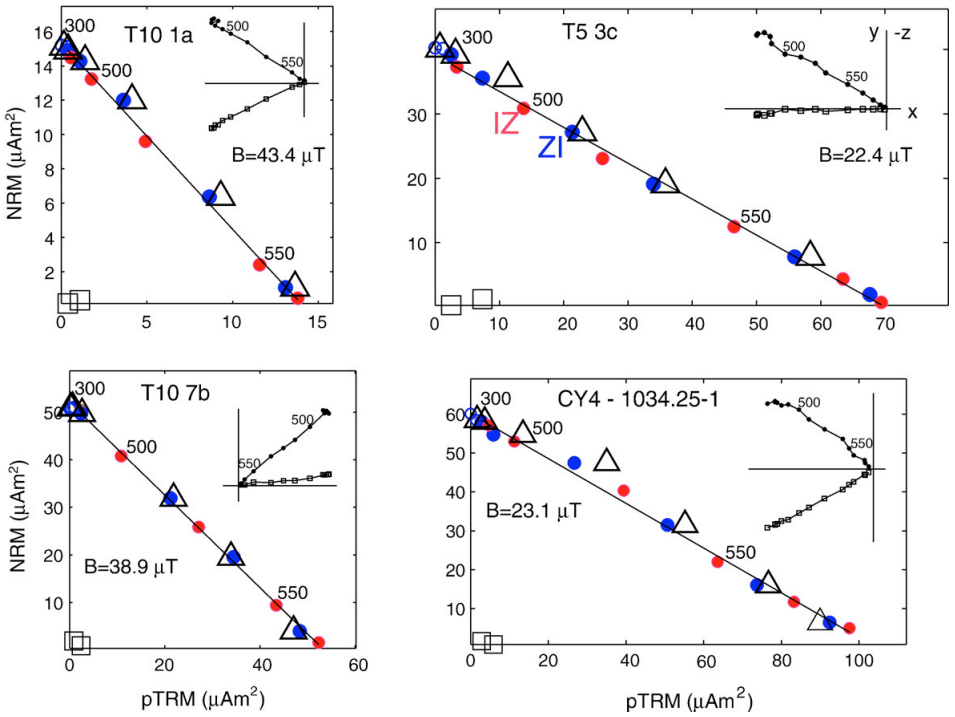

Fig. 2. Plots of representative examples of the modified Thellier–Thellier (IZZI) experiments on the Troodos lower crustal gabbros. Blue (red) symbols are the ZI (IZ) steps. Triangles and squares indicate pTRM checks and pTRM tail checks, respectively. Black line is the "best-fit" line over the temperature range used to estimate the intensity of the geomagnetic field. Insets show the corresponding vector end-point diagrams in specimen coordinates. Open and closed symbols indicate projections on the vertical and horizontal planes, respectively. (For interpretation of the references to colour in this figure legend, the reader is referred to the web version of this article.)

Table 1
Summary of paleointensity results

Specimen	T_1 (°C)	T_2 (°C)	N	$B_{anc.}$ (μT)	MAD	f_{vds} (%)	q	pTRM tail	DRATs	DANG (°)	β	VADM (Z Am^2)	R	VADM$_{AARM}$ (Z Am^2)
T5-3a	400	570	11	20.4	2.6	82	27.0	2.9	12	1.3	0.03	45.3		
T5-3b	300	570	12	19.1	2.9	89	26.3	1.3	12	1.1	0.03	42.4		
T5-3c	300	570	12	22.4	3.6	86	47.4	2.8	16	1.3	0.01	49.7		
T5-4a	400	570	11	17.9	2.7	80	25.6	6.2	18	1.2	0.03	39.7	I	
T5-4b	300	560	10	16.9	4.8	78	13.6	5.5	9	1.0	0.06	37.6		
T5-4cc	400	570	11	21.3	3.6	81	39.5	1.6	16	3.3	0.02	47.4	I	
T5-6b	300	570	12	26.0	2.5	89	35.7	1.8	10	1.6	0.02	57.9	I	
T5-7a	450	570	10	20.0	2.1	76	18.2	1.9	8	3.5	0.04	44.6		
T5-7bc	400	575	12	23.8	2.5	80	30.4	9.1	15	2.2	0.02	53.0	1.008	52.5
T5-7cc	400	570	11	25.4	3.4	83	32.0	1.6	15	2.4	0.02	56.5	I	
T6-11	450	575	11	58.3	2.0	87	36.6	1.3	18	0.5	0.02	130	I	
T6-12	450	575	11	60.6	1.8	86	65.9	0.9	22	0.8	0.01	135	I	
T6-13	450	575	11	56.6	1.1	86	28.8	1.0	15	1.2	0.02	126		
T6-14	450	575	11	61.6	2.0	89	63.5	1.9	10	0.2	0.01	137		
T6-51	520	575	9	43.2	2.8	78	17.6	1.6	22	2.7	0.04	96.2	I	
T6-54	450	575	11	52.7	2.7	83	32.5	4.4	13	0.8	0.02	117		
T8-31	400	555	8	26.3	3.4	75	18.3	6.1	22	3.5	0.03	58.5		
T8-33	500	565	8	27.3	4.1	67	9.25	4.4	21	4.0	0.06	60.7		
T8-34	300	560	10	29.7	3.6	80	16.9	4.7	13	3.7	0.04	66.1	I	
T8-35	450	570	10	19.2	4.9	76	12.9	4.0	16	4.3	0.06	42.6		
T8-51	300	560	10	26.0	3.4	82	15.4	3.3	23	3.2	0.05	57.8		
T10-1a	300	560	10	43.4	2.7	88	39.5	2.0	16	2.2	0.01	96.7	1.156	83.6
T10-2cc	300	555	9	39.0	3.3	86	27.3	5.7	17	3.6	0.02	86.7		
T10-2a	300	565	11	33.3	1.6	93	26.6	2.0	7	1.4	0.02	74.0	0.969	76.3
T10-3c	450	565	9	42.0	1.4	88	17.0	0.8	14	1.4	0.04	93.3		
T10-3dc	300	565	11	36.1	3.2	87	29.0	6.0	17	1.3	0.02	80.3		
T10-5a	300	565	11	41.7	1.6	91	64.1	2.0	10	1.0	0.01	92.8		
T10-5b	300	565	11	43.9	2.0	90	66.9	4.2	11	0.9	0.01	97.7		
T10-5c	300	560	10	45.3	3.2	93	38.6	2.1	6	2.4	0.02	101	1.609	62.7
T10-6b	300	555	9	32.3	3.0	92	46.1	4.0	11	4.6	0.01	71.8	0.778	92.2
T10-6c	300	550	8	59.2	3.3	91	20.3	4.0	18	9.6	0.03	132	1.832	72.0
T10-7a	450	555	7	42.7	1.5	87	18.4	3.4	11	1.7	0.03	95.0		
T10-7b	450	560	8	38.9	2.0	90	49.7	3.6	6	1.2	0.01	86.5		
T10-7c	450	560	8	35.2	2.6	81	16.4	6.8	7	3.4	0.04	78.4		
T11-1a	300	575	13	33.8	3.1	92	40.2	0.7	19	2.0	0.02	75.2		
T11-1b	400	560	9	32.5	3.9	77	21.4	2.5	24	1.5	0.03	72.4	I	
T11-4b	450	570	10	32.8	2.2	84	29.9	2.1	17	2.1	0.02	72.9		
T11-4cc	400	565	10	29.8	2.3	80	26.4	4.8	19	2.6	0.02	66.3	I	
T14-5b1	500	570	9	30.9	1.6	89	22.6	1.4	8	0.6	0.03	68.7		
T14-5b2	450	575	11	32.5	2.0	88	22.8	1.6	12	1.3	0.03	72.4		
T14-5b3	450	570	10	34.7	1.3	88	55.1	3.9	11	0.8	0.01	77.1		
T14-5b4	520	570	8	35.1	1.8	71	12.2	19.5	15	2.2	0.05	78.1		
T16-61	400	570	11	13.3	3.7	72	25.2	4.6	16	4.8	0.02	29.5		
T16-62	400	565	10	12.9	4.1	65	16.7	5.6	18	5.5	0.03	28.7		
T16-65	500	560	7	12.5	4.7	56	8.76	5.9	22	7.9	0.05	27.8		
T17-71	450	570	10	18.4	3.2	91	48.2	1.2	23	4.1	0.01	41.0		
T21-5a	450	565	9	21.8	3.9	76	26.2	4.2	25	4.2	0.03	48.5		
T21-5b	400	570	11	22.9	2.7	81	17.8	2.7	15	5.5	0.05	50.9		
T21-5c	500	570	9	21.0	4.8	58	32.2	6.2	25	5.0	0.01	46.8		
T29-6a	300	575	13	37.4	4.3	88	33.4	2.0	13	1.1	0.02	83.2		
T29-6b	500	575	10	36.6	2.4	50	29.8	4.7	25	1.8	0.01	81.5		
T29-6cc	450	565	9	42.2	2.8	82	36.8	3.8	15	2.2	0.02	93.8	I	
T32-11	500	575	10	22.0	3.5	75	38.0	2.0	10	1.8	0.02	49.0		
T32-12	500	575	10	13.9	3.2	80	31.3	3.3	6	3.4	0.02	31.0		
T32-13	500	575	10	15.8	2.4	80	27.8	2.5	7	2.8	0.02	35.1		
T32-14	530	570	7	23.6	3.1	59	15.2	4.6	11	3.9	0.04	52.5		
T35-11	450	565	9	20.1	3.2	59	18.6	4.4	17	2.1	0.04	44.8	I	

Table 1 (*continued*)

Specimen	T_1 (°C)	T_2 (°C)	N	$B_{anc.}$ (μT)	MAD	f_{vds} (%)	q	pTRM tail	DRATs	DANG (°)	β	VADM (Z Am^2)	R	VADM$_{AARM}$ (Z Am^2)
T35-12	520	570	8	22.6	3.0	51	23.8	3.1	17	2.5	0.02	50.2		
T35-13	500	565	8	23.1	2.4	64	20.8	2.1	20	4.7	0.03	51.4		
T35-14	450	570	10	25.0	3.3	74	13.1	4.3	11	9.2	0.05	55.6	I	
T36-32	520	570	8	21.8	3.4	64	27.7	4.6	25	4.1	0.02	48.4		
T36-33	500	575	10	22.0	1.9	86	26.1	2.6	15	0.4	0.03	49.0		
T36-34	500	575	10	21.4	2.6	83	25.3	5.7	23	1.2	0.03	47.6		
TR3-c1-1	300	565	11	30.1	2.0	97	25.8	0.8	25	3.2	0.03	66.9		
TR3-c1-2	450	560	8	36.8	2.4	80	15.0	3.0	18	1.4	0.04	82.0		
TR3-c1-3	300	550	8	35.2	3.1	78	11.2	3.8	6	3.4	0.05	78.3		
TR5-e1-1	500	570	9	25.0	4.4	78	11.7	1.3	21	2.3	0.07	55.6	I	
TR5-e1-2	500	570	9	23.9	2.9	77	12.4	5.0	15	3.5	0.06	53.2	I	
TR5-e1-4	550	575	6	29.4	2.6	50	9.14	6.7	19	4.6	0.05	65.4	I	
TR6-a2-1	400	555	8	31.1	2.4	77	8.67	4.2	5	4.3	0.07	69.2		
TR6-a2-2	300	560	10	28.6	3.6	79	17.0	2.0	19	4.8	0.04	63.6		
TR6-a2-3	400	550	7	30.3	4.6	63	12.0	5.1	11	8.0	0.04	67.4		
CY-4, 781.5-1	500	570	9	59.2	3.0	70	16.8	3.5	11	2.0	0.04	132		
CY-4, 781.5-2	450	575	11	52.6	2.4	84	25.3	1.4	9	1.9	0.03	117		
CY-4, 781.5-3	500	575	10	50.6	4.0	73	23.3	6.2	15	1.8	0.03	113		
CY-4, 1034.25-1	300	570	12	23.1	3.9	83	32.2	2.5	25	4.5	0.02	51.3		
CY-4, 1034.25-2	300	575	13	24.2	3.1	87	39.5	3.8	20	4.1	0.02	53.9	1.138	47.3
CY-4, 1034.25-3	300	575	13	19.8	3.8	81	22.4	2.2	24	3.5	0.03	44.0	I	
CY-4, 1329.2-1	500	575	9	32.4	2.2	71	14.0	3.1	17	1.0	0.05	72.1		
CY-4, 1329.2-2	300	565	11	39.7	1.7	95	25.9	3.3	13	0.8	0.03	88.3		
CY-4, 1329.2-3	300	565	11	40.2	1.8	93	31.7	1.5	19	2.1	0.02	89.4		

Temperature range used in the best-fit line is between T_1 and T_2. N corresponds to the number of points used in the calculation, and $B_{anc.}$ is the resultant intensity of the field. f_{vds}, q, and β are the fraction of remanent magnetization (based on the vector difference sum), quality factor, and the degree of scattering for the chosen data points. MAD (maximum angular deviation), pTRM checks, DRATs (difference ratio sum), and DANG (deviation angle) are parameters used to assess whether chemical alteration or abnormal magnetic behavior was taking place during the experiments (Appendix A). The degree to which a given specimen was affected by remanence anisotropy is shown by R. We denoted R as I for the isotropic specimens. VADM$_{AARM}$ corresponds to the VADM corrected for anisotropic effect. None of the values are corrected for slow cooling effect. These specimens all passed the zig-zag test. Labels for the specimens from CY-4 drill site correspond to their depth (m). Note: the site labels here differ from those in [32] by the addition of the letter T, added here to distinguish the gabbro sites from the glass sites from [10].

placed in the time-series from outcrop samples. We will first address the suitability of the Troodos gabbros for paleointensity measurements.

Then we will compare the Troodos results with other published paleointensity data from a similar time interval including the results from the upper crust of Tauxe and Staudigel [10]. Finally, we will discuss the implications of the paleointensity data for the results from numerical simulations.

2. Methods

The gabbro samples were sliced into specimens 5 to 10 mm in size. These were fixed into quartz tubes and then measured in the magnetically shielded room at the paleomagnetic laboratory of the Scripps Institution of Oceanography. The Thellier–Thellier method is widely accepted for determining absolute geomagnetic intensity. In this technique, samples are repeatedly heated and cooled in zero field or in a laboratory field at progressively higher temperature steps [34]. Accurate absolute paleointensities require that the blocking and unblocking temperatures be identical (i.e., the reciprocity condition, where the magnetic carriers have single domain like behavior), and no mineralogical alteration takes place while re-heating the samples in the laboratory. To monitor the equivalence of blocking and unblocking temperatures, we performed a modified version of Thellier–Thellier method (the IZZI experiment of [35]; Fig. 2). In this method we successively heat each specimen to a given temperature. Then one of two procedures was followed. In the ZI procedure, the specimen is cooled first in zero field (Z) followed by re-heating and cooling in a 40 μT laboratory field (I). In the other procedure (IZ), the specimen is cooled first in the laboratory field, then re-heated and cooled in zero field. The laboratory field was directed along the specimen's "Z" axis. These IZ and ZI steps are alternated for

subsequent temperature steps. Within a given temperature step we re-heat the specimens to a lower temperature step and cool in the laboratory field to assess the change of their capacity to acquire partial thermal remanent magnetization (a pTRM check). We also performed an additional step in which we re-heated and cooled the specimens in zero field (a pTRM tail check) to assess whether the pTRM acquired at a given temperature is fully removed by cooling in zero field at the same temperature. The existence of so-called high temperature pTRM tails can perhaps better be revealed by the zig-zagging pattern in the IZZI experiment as shown in the natural remanent magnetization (NRM) versus pTRM (Arai plot, please see Appendix A for a thorough description of the analysis procedure), or in the vector end-point diagrams. We performed a total of 12 to 15 temperature steps for a total of up to 45 measurements on each specimen. The results are evaluated according to statistical criteria explained in Appendix A.

3. Results

3.1. Lower crust paleointensity results

The IZZI experiment reveals a characteristic component of magnetization unblocked in the 350–580 °C temperature range and occasionally a minor additional low-temperature (<200–300 °C) overprint magnetization (see insets to Fig. 2). The typical maximum unblocking temperatures are near 580 °C. The magnetic carriers demonstrate a relatively high coercivity spectra (median destructive field of 45 mT) [32]. These characteristics suggest that the magnetic carrier of the Troodos gabbros is an oxyexsolved low-Ti titanomagnetite of single to perhaps small pseudo-single domain grain size.

From the entire specimen collection, ninety one samples passed all criteria (examples are shown in Fig. 2). The results were then averaged by site. Our sampled sites are located hundreds to thousands of meters apart, implying that each site mean is likely to represent a distinct cooling unit.

The sources for paleointensity variations within a given site include alteration, measurement errors, or remanence anisotropy. Both alteration and measurement errors can be detected by the various statistical criteria (Appendix A). The relative orientation of the remanence anisotropy tensor and the direction of the laboratory field controls the way in which the anisotropy effects the resultant paleointensity value (Appendix A, [36]). Our drilled cores and sliced specimens were randomly oriented with respect to one another, which results in a random anisotropic effect. Therefore, sites showing a well grouped paleointensity results (i.e., the results deviate less than 25% or 5 μT from the site mean) are unlikely to be biased by anisotropy. For specimens with a higher degree of variation relative to their site mean, we determined the remanence anisotropy and corrected the paleointensity estimate following [36]. The correlation between the degree of deviation from the site mean and the degree to which a given specimen is effected by anisotropy (R, Table 1) further confirms the assumption that significant remanence anisotropy is manifested by substantial within-site paleofield scatter. Sites with within-site variability greater than 25% or 5 μT even after the remanence anisotropy correction were eliminated from further consideration.

We consider only sites that have at least three specimens. After examination of the consistency of the results within and among specimens from a given site, we are left with 18 high-quality sites, with a total of 80 specimens (Fig. 3, Tables 1 and 2). The average virtual axial dipole moment (VADM), unadjusted for slow cooling, for the gabbros is 67 ± 24 Z Am^2 (paleolatitude of 20° [37]). The variations in the dipole moments are up to 35% of the mean and are similar to the Cenozoic magnetic field variations [16].

Within our acceptable data set, eight gabbroic sites are located within a single tectonically undisrupted domain (Fig. 1) and can be used to examine temporal variations of the geomagnetic field (Fig. 3a). The paleointensity data from these sites exhibit considerable serial correlation and appear to define a quasi-cyclic geomagnetic field variation along the 11 km of the lower oceanic crust. Assuming a full spreading rate of 20 to 75 mm/yr [23–27], this corresponds to 0.3 to 1.1 Ma of accretion.

3.2. Upper crust paleointensity analysis

In addition to the time-series from the gabbro samples presented in the foregoing, Tauxe and Staudigel [10] presented data from submarine basaltic glasses (SBG) obtained from two transects through the Troodos extrusive section providing two independent temporal views of the CNS magnetic field (Fig. 1). These transects are located east of our gabbro sequence and consequently record different, most likely earlier times of the CNS field. The two transects are 10 km apart along the spreading direction, implying an age difference of some 0.2 to 1 Ma (Fig. 1). Each transect contains up to ten geochemically distinctive units [38] creating a time-series that might span as much as 10^5 yrs [39]. The actual time interval between the various pillow lava flows is

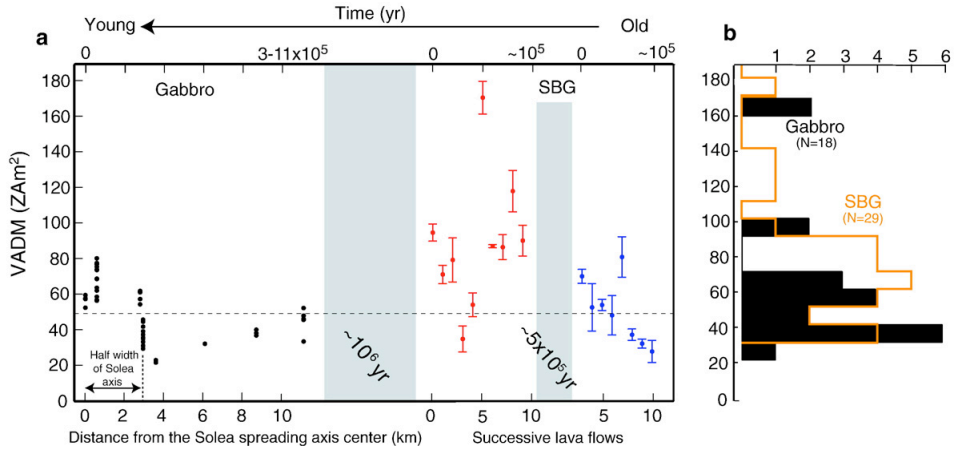

Fig. 3. Summary of paleointensity data from the Troodos ophiolite. All results were converted to VADM (assuming a paleolatitude of 20° [37]). (a) Three time-series of the magnetic dipole moments during the late CNS from the gabbros and glasses [10]. Gray areas represent gaps in time estimated from moderate spreading rate (full spreading rate of 20 to 75 mm/yr). Results for the gabbro specimens are shown as individual points and are corrected for cooling rate and anisotropy (see text for details). Results for the SBG sites correspond to the average results from successive cooling units (color scheme same as in Fig. 1b). Dashed line represents the average field of the Cenozoic [16]. (b) Histograms of all paleointensity data available from the upper [10] and lower Troodos crust. Data counts are from individual sites. Results for the gabbros are corrected for cooling rate.

unknown. From the original work of [10], we have used only those data points whose age relations were known from stratigraphic order and conformed to our selection criteria (Fig. 3a). Glasses from dikes have been excluded from consideration. These two time-series, although more scattered than the gabbroic series, also appear to exhibit serial correlation. Their grand mean averaged VADM was reported as 75± 41 Z Am^2 whereas the mean VADM of the data subset used here is 77±36 Z Am^2.

Table 2
Summary of site statistics based on the results shown in Table 1

Site	Lat. (°N)	Long. (°E)	N	$\overline{B}$ (μT)	σ_B	$100(\sigma/\overline{B})$	VADM (Z Am^2)	σ_{VADM}
T5	34.5376	32.5023	10	21.3	3.0	7.8	37.8	5.4
T6	34.5545	32.4905	6	55.5	6.8	12.2	98.8	12.1
T8	34.5416	32.5916	5	26.9	5.2	19.5	47.8	9.3
T10	34.5307	32.5247	13	38.0	4.6	12.1	65.7	10.3
T11	34.5342	32.5210	4	32.2	1.7	5.3	57.3	3.0
T14	34.5359	32.5395	4	33.3	2.0	5.9	59.2	3.4
T16	34.5279	32.5438	3	12.9	0.4	3.1	22.9	0.7
T21	34.5362	32.5763	3	21.9	1.0	4.3	38.9	1.6
T29	34.5249	33.0302	3	38.7	3.0	7.8	68.9	5.3
T32	34.5222	33.0479	4	18.8	4.7	24.9	33.5	8.3
T35	34.5423	33.0104	4	22.7	2.0	8.8	40.4	3.5
T36	34.5361	33.0168	3	21.7	0.3	1.4	38.6	0.5
TR3	34.5826	32.5576	3	34.0	3.5	10.2	60.6	6.2
TR5	34.5547	32.4741	3	26.1	2.9	11.1	46.4	5.1
TR6	34.5612	32.4726	3	30.0	1.3	4.2	53.3	2.2
CY-4, 781.5	33.0538	34.5406	3	54.1	4.5	8.3	96.5	8.0
CY-4, 1034.25	33.0538	34.5406	3	21.4	1.7	7.7	39.7	4.1
CY-4, 1329.2	33.0538	34.5406	3	37.4	4.4	11.6	66.6	7.7

N are the number of specimens used in the calculation. The averaged field values ($\overline{B}$, σ_B) are not corrected for cooling rate, whereas the virtual axial dipole moment (VADM, λ=20°) are corrected for cooling rate ($VADM_{corrected}$=0.8 VADM).

4. Discussion

Rapidly cooled igneous rocks (e.g., SBG) record the variability of the geomagnetic field with virtually no averaging involved, whereas slowly cooled rocks (e.g., gabbros) should filter out the short wavelength changes of the field. Furthermore, the ratio between the cooling rates of plutonic rocks during formation and in the laboratory results in an overestimation of the ancient geomagnetic field [40]. SBG cools in nature at a similar cooling rate as in the laboratory [41], and consequently require no significant cooling rate correction. Direct measurements from the lower crust at the Mid-Atlantic Ridge [42] and thermal modeling [43] suggest that lower oceanic crustal cooling (over the 600 to 300 °C temperature range relevant for our paleointensity estimates) may require up to 10^5 yrs. These cooling rates are significantly slower than in the laboratory and would equate to overestimates of the ancient field by 40% [44,36]. Actual cooling rates for the Troodos gabbros are poorly constrained but might be significantly faster, for example due to hydrothermal circulation. We have arbitrarily corrected the gabbro paleointensity estimates by a factor of 0.8, corresponding to a 20% overestimate of the ancient field. Since we are primarily concerned with paleointensity variations, the precise cooling rate correction is not critical although cooling rate variations might account for up to 10% of the between-site paleointensity variations. Since the cores within each sites are located a few meters apart, and there were no petrographic (i.e., grain size) or any field indications for a thermal boundary, we conclude that cooling rate variations within a single site are unlikely and therefore cannot explain within-site paleointensity variations.

The cooling rate corrected gabbro results range from 23 to 96 Z Am^2 (Fig. 4 and Table 2), and the corrected average VADM of the gabbros is 54±20 Z Am^2. This value, although statistically indistinguishable, is lower than the extrusive averaged dipole moment. We speculate that the reason for the difference is that the portions of the crust discussed here sample different time intervals, and therefore record different time-series of the geomagnetic field.

By considering all three time-series, it is possible to place constraints on the variability of the geomagnetic field during the CNS in a more definitive manner than heretofore possible. Discrepancies noted in the published data, especially in those studies that had few data points, are plausibly attributed to under-sampling of the true geomagnetic field variability, with some studies sampling peaks of the geomagnetic field [e.g., [9]] and others sampling low points [e.g., [7]].

The observed trend in the gabbros is also interesting when taking into account the slow to intermediate spreading environment in which the Troodos crust formed. The quasi-continuous VADM trend is suggestive of a relatively continuous lower crust formation with negligible re-heating events, if any, after the initial cooling within the accretion zone.

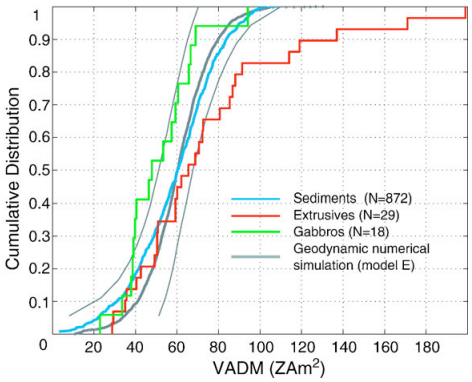

Fig. 4. Distributions of dipole moments from the late CNS. Heavy gray line corresponds to the geodynamo numerical simulation results [model E [2]]. The 95% confidence bounds (fine gray lines) for the numerical simulation were determined from CDFs for a large number of pseudo-samples (each with 18 samples as for the Troodos gabbros data) drawn from the simulation. Gabbros (corrected for cooling rate) and glasses [10] results are shown in green and red, respectively. The median of the sediment record (blue, [15]) is adjusted to the median of the numerical simulation data. In brackets are the number of cooling units that are used in the calculation. (For interpretation of the references to colour in this figure legend, the reader is referred to the web version of this article.)

4.1. Comparison with other data sets and geodynamo numerical simulations

Cumulative distributions of VADM data allow us to compare the Troodos data sets and the geodynamo model predictions (Fig. 4). We use for comparison Model E of Glatzmair et al. [2] as it is the only model which shows no reversals throughout the 300 kyr simulation and best represents the CNS. The mean values for extrusives (75 Z Am^2), intrusives (54 Z Am^2), and the geodynamo numerical simulations (60 Z Am^2) are quite similar, and are comparable to the post-CNS average intensity field [16,13]. The apparent concordance of our results with the model is artificial, however, because Glatzmaier et al. [2] argue that the true average of their numerical simulations must be higher owing the computational necessity of using unrealistically high outer core viscosities. The paleointensity data from Troodos include a substantial number of sites, both from extrusive and intrusive rocks. The spatial distribution of these sites, together with the time averaging inherent in

slowly cooled gabbros, should provide a robust estimate of the geomagnetic field in the latter part of the CNS. To the extent that these data are representative, we conclude that an average value for the late CNS dipole moment much higher than ~60–70 Z Am^2 is unlikely.

The comparison between the data sets also allows us to consider the variability of intensity values in the late CNS. For this purpose, we plot the sedimentary relative paleointensity data of Cronin et al. [15], adjusted to a common median value with the numerical simulation data. The sedimentary and intrusive data sets have remarkably similar distributions, and display much less variability than the extrusives. We attribute this to the fact that both intrusive and sedimentary samples average the geomagnetic field over some period of time while extrusives are more likely to represent "snap shots" of field intensities. Also, specimens of SBG are weakly magnetized and instrumental noise means that the weakest specimens are never measured, resulting in a possible bias in SBG data toward higher field values. Therefore, the variability of the geomagnetic field during the late CNS was significantly higher than that predicted by the numerical simulations.

5. Conclusions

The paleointensity results from 18 sites in the lower Troodos crust shown here, together with previously published results from the upper Troodos crust provide three independent time-series of absolute paleointensities from the CNS. The serial correlation of the data provides an independent confirmation of the quality of our results and agrees with the available sediment and extrusive records. The observed quasi-continuous paleointensity trend in the lower Troodos crust also suggests relatively continuous cooling of the lower crust.

The high variability of the paleointensity data from the Troodos ophiolite may offer an explanation for the wide range of paleofield estimates previously reported from the CNS. Based on the mean value of 54± 20 Z Am^2 we suggest that the geomagnetic field was weaker and more variable than the predictions made by the geodynamo numerical simulations. This result can be used to refine the geodynamo numerical simulations.

Acknowledgments

We thank G. Glatzmair for providing the geodynamic numerical modeling results for comparison with our data. We also thank A. Agnon, M. Abelson, and R. J. Varga for kindly allowing us to use their specimens. The manuscript was greatly improved by the constructive comments of the editor M.L. Delaney and by the comments of two anonymous reviewers. This work was partially supported by the National Science Foundation grant OPP-0229403.

Appendix A. Analysis of IZZI results

The results from the IZZI experiment are assessed according to the following reliability criteria (see Lecture 10 of http://earthref.org/MAGIC/books/Tauxe/2005/ for more details). At least five data points are needed in the calculation. The best-fit lines to the progressive thermal demagnetization vectors are calculated using principal component analysis [45]. The maximum angular deviation (MAD) about the characteristic magnetization vector (ChRM) of the chosen points has to be less than 15°. The

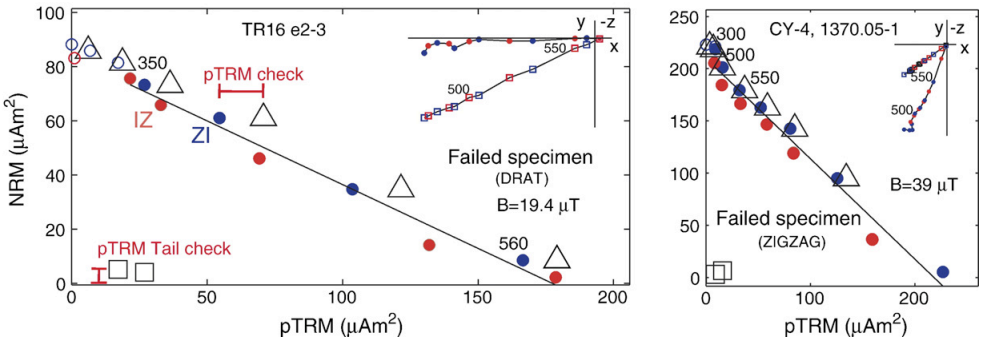

Fig. 5. Representative illustrations of the selection criteria that were used to evaluate the quality of the measurements. Blue (red) symbols represent the ZI (IZ) steps. The slopes and the vectorial directions of both ZI and IZ populations are compared to assess whether the specimens are uniformly magnetized. Open triangles and squares indicate the pTRM checks and pTRM-tail checks, respectively. Both specimens demonstrate unacceptable results due to high DRAT (left) and failure of the zig-zag test (right). (For interpretation of the references to colour in this figure legend, the reader is referred to the web version of this article.)

ChRM has to point toward the origin with a deviation angle (DANG) of less than 10°. In the NRM–pTRM plots (i.e., Arai plots), the best-fit line through the chosen data points must have low scatter around the mean [46], ($\beta=\sigma/|b|<0.1$). We sum all the differences between the pTRM checks and the corresponding original pTRM and normalized it by the pTRM gained in the temperature range used for the paleofield determination. This difference ratio sum (DRATs) must be less than or equal to 25% in order to avoid the use of specimens that developed chemical alteration during the experiment. The fraction of remanent magnetization (f_{vds}, vector difference sum) was always greater than 50%.

We use a new parameter to quantify the degree of "zig-zagging" observed in the IZZI experiment. Here we assess the zig-zagging nature of the specimens by evaluating the slopes of the ZI and IZ data points separately. The results of a given specimen are thought to be of a good quality if these slopes are statistically distinct at the 95% confidence level (using the test for common mean of [47]) (Fig. 5). This evaluation of the zig-zagging nature does not require a threshold limit, but produces an independent fail/pass criteria.

We have used pTRM tail checks [48] in the lower temperature range (<300 °C) where it had to be less than 5% and the zig-zagging parameter above this temperature range. In cases where it was needed, the paleointensities were corrected for the anisotropy of remanence as follows [36]:

$$B_{\mathrm{corrected}} = R/B_{\mathrm{anc}} \tag{1}$$

where R is:

$$R = \frac{|\chi\cdot\hat{H}_{\mathrm{anc}}|}{|\chi\cdot\hat{H}_{\mathrm{lab}}|} \tag{2}$$

and χ is the remanence anisotropy tensor, $\hat{H}_{\mathrm{anc}}$ is the ancient field direction determined from the ChRM direction and the anisotropy tensor, and $\hat{H}_{\mathrm{lab}}$ is the lab field direction applied along the sample Z coordinate axis.

References

[1] R.T. Merrill, M.W. McElhinny, P.L. McFadden, The Magnetic Field of the Earth: Paleomagnetism, the Core, and the Deep Mantle, Int. Geophys. Ser., Academic, San Diego, Calif., 1996.

[2] G.A. Glatzmaier, R.S. Coe, L. Hongre, P.H. Roberts, The role of the Earth's mantle in controlling the frequency of geomagnetic reversals, Nature 401 (1999) 885–890.

[3] J. Bloxham, Sensitivity of the geomagnetic axial dipole to thermal core–mantle interactions, Nature 405 (2000) 63–65.

[4] J.E.T. Channell, M. Erba, E. Nakanashi, K. Tamaki, Late Jurassic–early Cretaceous time scales and oceanic magnetic anomaly block models, in: W. Berggren, D.V. Kent, M. Aubry, J. Hardenbol (Eds.), Geochronology, Time Scales and Global Stratigraphic Correlation, Soc. Sed. Geol., vol. 54, 1995, pp. 51–63.

[5] S.C. Cande, D.V. Kent, Revised calibration of the geomagnetic polarity timescale for the late Cretaceous and Cenozoic, J. Geophys. Res. 100 (1995) 6093–6095.

[6] P. Riisager, J. Riisager, X.X. Zhao, R.S. Coe, Cretaceous geomagnetic paleointensities: Thellier experiments on pillow lavas and submarine basaltic glass from the Ontong Java Plateau, Geochem. Geophys. Geosyst. 4 (12) (2003), doi:10.1029/2003GC000611.

[7] H.F. Tanaka, M. Kono, Paleointensities from a Cretaceous basalt platform in inner Mongolia, northeastern China, Phys. Earth Planet. Inter. 133 (2002) 147–157.

[8] J.A. Tarduno, R.D. Cottrell, A.V. Smirnov, The Cretaceous superchron geodynamo: observations near the tangent cylinder, Proc. Natl. Acad. Sci. U. S. A. 99 (2002) 14020–14025.

[9] J.A. Tarduno, R.D. Cottrell, A.V. Smirnov, High geomagnetic intensity during the mid-Cretaceous from Thellier analyses of single plagioclase crystals, Science 291 (2001) 1779–1783.

[10] L. Tauxe, H. Staudigel, Strength of the geomagnetic field in the Cretaceous normal superchron: new data from submarine basaltic glass of the Troodos ophiolite, Geochem. Geophys. Geosyst. 5 (2) (2004), doi:10.1029/2003GC000635.

[11] X.X. Zhao, P. Riisager, J. Riisager, U. Draeger, R.S. Coe, Z. Zheng, New palaeointensity results from Cretaceous basalt of inner Mongolia, China, Phys. Earth Planet. Inter. 141 (2004) 131–140.

[12] T. Pick, L. Tauxe, Geomagnetic palaeointensities during the Cretaceous normal superchron measured using submarine basaltic glass, Nature 366 (1993) 238–242.

[13] L. Tauxe, Long-term trends in paleointensity: the contribution of DSDP/ODP submarine basaltic glass collections, Phys. Earth Planet. Inter. 156 (2006) 223–241.

[14] A. Kurazhkovskii, N. Kurazhkovskaya, B. Klain, A. Guzhikov, Paleointensity behavior in Barremian–Cenomanian (Cretaceous), Int. J. Geomagn. Aeron. 5 (2004), doi:10.1029/2003GI000043.

[15] M. Cronin, L. Tauxe, C. Constable, P.A. Selkin, T. Pick, Noise in the quiet zone, Earth Planet. Sci. Lett. 190 (2001) 13–30.

[16] P.A. Selkin, L. Tauxe, Long-term variations in paleointensity, Philos. Trans. R. Soc. Lond., A 358 (2000) 1065–1088.

[17] J.A. Tarduno, R.D. Cottrell, Dipole strength and variation of the time-averaged reversing and nonreversing geodynamo based on Thellier analyses of single plagioclase crystals, J. Geophys. Res. 110 (2005), doi:10.1029/2005JB003970.

[18] J.P. Valet, Time variations in geomagnetic intensity, Rev. Geophys. 41 (1) (2003), doi:10.1029/2001RG000104.

[19] S.C. Cande, D.V. Kent, Ultrahigh resolution marine magnetic anomaly profiles: a record of continuous paleointensity variations? J. Geophys. Res. 97 (1992) 15075–15083.

[20] J.S. Gee, S.C. Cande, J.A. Hildebrand, K. Donnelly, R.L. Parker, Geomagnetic intensity variations over the past 780 kyr obtained from near-seafloor magnetic anomalies, Nature 408 (2000) 827–832.

[21] J. Bowles, L. Tauxe, J. Gee, D. McMillan, S.C. Cande, Source of tiny wiggles in chron C5: a comparison of sedimentary relative intensity and marine magnetic anomalies, Geochem. Geophys. Geosyst. 4 (6) (2003), doi:10.1029/2002GC000489.

[22] S.B. Mukasa, J.N. Ludden, Uranium–lead isotopic ages of plagiogranites from the Troodos ophiolite, Cyprus, and their tectonic significance, Geology 15 (1987) 825–828.

[23] E.M. Moores, F.J. Vine, Troodos massif, Cyprus and other ophiolites as oceanic crust — evaluation and implications, Philos. Trans. R. Soc. Lond. Ser. 268A (1971) 443–466.

[24] S.D. Hurst, E.M. Moores, R.J. Varga, Structural and geophysical expression of the Solea graben, Troodos ophiolite, Cyprus, Tectonics 13 (1) (1994) 139–156.
[25] C. Small, Global systematics of mid-ocean ridge morphology, in: R. Buck, P. Delaney, J.A. Karson, Y. Lagabrielle (Eds.), Faulting and Magmatism at Mid-Ocean Ridges, Geophys. Mon. Ser., vol. 106, Am. Geophys. Union, Washington, D.C., 1998, pp. 1–26.
[26] R.J. Varga, J.S. Gee, L. Bettison-Varga, R.S. Anderson, C.L. Johnson, Early establishment of seafloor hydrothermal systems during structural extension: paleomagnetic evidence from the Troodos ophiolite, Cyprus, Earth Planet. Sci. Lett. 171 (2) (1999) 221–235.
[27] P.A. Rona, Hydrothermal mineralization at seafloor spreading centers, Earth-Sci. Rev. 20 (1984) 1–104.
[28] J.M. Sinton, R.S. Detrick, Mid-ocean ridge magma chambers, J. Geophys. 97 (B1) (1992) 197–216.
[29] R.J. Varga, E.M. Moores, Spreading structure of the Troodos ophiolite, Cyprus, Geology 13 (1985) 846–850.
[30] C.J. Macleod, A.H.F. Robertson, S. Allerton, P. Browning, I.G. Gass, R.N. Taylor, F.J. Vine, C. Xenophontos, Tectonic evolution of the Troodos ophiolite within the Tethyan framework — comment, Tectonics 11 (1992) 910–915.
[31] C.J. Macleod, S. Allerton, I.G. Gass, C. Xenophontos, Structure of a fossil ridge-transform intersection in the Troodos ophiolite, Nature 348 (1990) 717–720.
[32] R. Granot, M. Abelson, H. Ron, A. Agnon, The oceanic crust in 3D: paleomagnetic reconstruction in the Troodos ophiolite gabbro, Earth Planet. Sci. Lett. 251 (2006) 280–292.
[33] N. Bonhommet, P. Roperch, F. Calza, Paleomagnetic arguments for block rotations along the Arakapas fault (Cyprus), Geology 16 (1988) 422–425.
[34] R.S. Coe, Paleointensities of earths magnetic field determined from Tertiary and Quaternary rocks, J. Geophys. Res. 72 (1967) 3247–3262.
[35] Y.J. Yu, L. Tauxe, A. Genevey, Toward an optimal geomagnetic field intensity determination technique, Geochem. Geophys. Geosyst. 5 (2) (2004), doi:10.1029/2003GC000630.
[36] P.A. Selkin, J.S. Gee, L. Tauxe, W.P. Meurer, A.J. Newell, The effect of remanence anisotropy on paleointensity estimates: a case study from the Archean Stillwater complex, Earth Planet. Sci. Lett. 183 (2000) 403–416.
[37] T.M.M. Clube, K.M. Creer, A.H.F. Robertson, Paleorotation of the Troodos microplate, Cyprus, Nature 317 (1985) 522–525.
[38] M. Rautenschlein, G.A. Jenner, J. Hertogen, A.W. Hofmann, R. Kerrich, H.U. Schmincke, W.M. White, Isotopic and trace element composition of volcanic glasses from the Akaki canyon, Cyprus: implications for the origin of the Troodos ophiolite, Earth Planet. Sci. Lett. 75 (1985) 369–383.
[39] H.U. Schmincke, M. Rautenschlein, P.T. Robinson, J.M. Mehegan, Troodos extrusive series of Cyprus: a comparison with oceanic crust, Geology 11 (1983) 405–409.
[40] S.L. Halgedahl, R. Day, M. Fuller, The effect of cooling rate on the intensity of weak-field TRM in single-domain magnetite, J. Geophys. Res. 85 (7) (1980) 3690–3698.
[41] J. Bowles, J.S. Gee, D.V. Kent, E. Bergmanis, J. Sinton, Cooling rate effects on paleointensity estimates in submarine basaltic glass and implications for dating young flows, Geochem. Geophys. Geosyst. 6 (7) (2005), doi:10.1029/2004GC000900.
[42] J. Gee, W.P. Meurer, Slow cooling of middle and lower oceanic crust inferred from multicomponent magnetizations of gabbroic rocks from the Mid-Atlantic ridge south of the Kane fracture zone (MARK) area, J. Geophys. Res. 107 (7) (2002), doi:10.1029/2000JB000062.
[43] W.J. Shaw, J. Lin, Models of ocean ridge lithospheric deformation: dependence on crustal thickness, spreading rate, and segmentation, J. Geophys. Res. 101 (B8) (1996) 17977–17993.
[44] G. Pullaiah, E. Irving, K.L. Buchan, D.J. Dunlop, Magnetization changes caused by burial and uplift, Earth Planet. Sci. Lett. 28 (1975) 133–143.
[45] J.L. Kirschvink, The least-squares line and plane and the analysis of paleomagnetic data, Geophys. J. R. Astron. Soc. 62 (1980) 699–718.
[46] R.S. Coe, S. Gromme, E.A. Mankinen, Geomagnetic paleointensities from radiocarbon-dated lava flows on Hawaii and question of Pacific nondipole low, J. Geophys. Res. 83 (1978) 1740–1756.
[47] G.S. Watson, Large sample theory of the Langevin distributions, J. Stat. Plan. Inference 8 (1983) 245–256.
[48] P. Riisager, J. Riisager, Detecting multidomain magnetic grains in Thellier palaeointensity experiments, Phys. Earth Planet. Inter. 125 (2001) 111–117.

This chapter, in full, is a reprint of the material as it appears in *Earth and Planetary Science Letters*, R. Granot, L. Tauxe, J. S. Gee, and H. Ron, A view into the Cretaceous geomagnetic field from analysis of gabbros and submarine glasses, 256, 1-11, 2007.

I collected, processed, and interpreted all of the data in this chapter. Lisa Tauxe provided significant advice on laboratory methods, data interpretation, and analysis. Jeff Gee provided continuous advice. Sampling in the field was carried out by myself and Hagai Ron.

Chapter 2

The implications of long-lived asymmetry of remanent magnetization across the North Pacific fracture zones

Abstract. Large marine magnetic anomalies accompany the Pacific fracture zones (FZs) for thousands of kilometers. Although the origin of these anomalies is poorly understood, their underlying magnetization contrasts should reflect the temporal record of crustal accretion as well as geomagnetic field variations. Here we present an analysis of archival and newly collected magnetic anomaly profiles measured across three FZs from the North Pacific Cretaceous Quiet Zone (120.6 to 83 Ma) that are characterized by a remarkably uniform shape. Forward and inverse modeling indicates that these anomalies arise from remanent magnetization, with enhanced remanence located on one side of each FZ along the entire studied area. A comparison between geochemical and magnetic data from active ridge discontinuities and transform faults suggests that elevated iron content near segment ends is likely responsible for the observed anomalies in the Cretaceous Quiet Zone as well. A more complex magnetization setting is observed where the FZs contain multiple faults. There, the simple model of one-sided enhancements

is only partly valid. Comparison between 3D forward modeling of the Quiet Zone magnetization and the calculated magnetization contrasts found across the Pioneer and Pau FZs suggests that the intensity of the geomagnetic field during the Cretaceous superchron had less than 50 percent variability about its average value. No major trends in the strength of the geomagnetic field during the superchron are observed. The presence of long-duration (> 30 m.y.) zones of enhanced magnetization along the young/old sides of the Pioneer/Pau FZs (both left-stepping) requires some long-lived asymmetry in crustal construction processes near ridge-transform intersections. Although the underlying mechanism that controls this long-lived asymmetry remains unclear, absolute plate motions might explain this asymmetry. Shorter period (few m.y.) variations in the amplitudes of the enhancements probably result from oscillations in crustal construction.

2.1 Introduction

Marine magnetic anomalies, typically measured along the direction of seafloor spreading, are used to study the geomagnetic reversal sequence as well as the kinematics of lithospheric plates (using polarity and skewness). The integrated magnetization of the oceanic crust also reflects its tectono-magmatic evolution (i.e., geochemistry and magnetic source layer geometry) and fluctuations in geomagnetic field behavior (Gee and Kent, 2007). For example, higher amplitude magnetic anomalies are associated with iron-rich lavas, particularly near ridge crest discontinuities (Sempere, 1991; Carbotte and Macdonald, 1992), and variations in the source layer thickness also appear correlated with anomaly amplitude (e.g., Bazin et al., 2001). Coherence between multiple profiles and similarity globally (e.g., Cande and Kent, 1992; Bowers et al., 2001) suggest that many short wavelength magnetic anomalies ("tiny wiggles" within constant polarity intervals) are related to variations in geomagnetic field intensity.

Magnetic anomalies observed across fracture zones (FZs), where crust of different age that formed at two adjoining spreading segments is juxtaposed, can provide insights into aspects of crustal construction and, potentially, geomagnetic

field behavior. Indeed, studies from the fast spreading East Pacific Rise (Carbotte and Macdonald, 1992) and from the intermediate spreading Juan de Fuca-Gorda ridge area (Detrick and Lynn, 1975; Vogt and Byerly, 1976) revealed high-amplitude magnetic anomalies that parallel the transform faults and FZs. These higher amplitude anomalies have been attributed to enhanced low-pressure fractionation leading to iron enrichment at colder segment ends. Transform faults may also be characterized by variations in crustal thickness (Barth, 1994; Gregg et al., 2007) and secondary volcanism (Menard and Atwater, 1969) or alteration (Hosford et al., 2003) that may modulate magnetic anomaly amplitudes. For example, a pattern of more positive magnetization at the ends of slow-spreading segments, regardless of the polarity, has been interpreted as reflecting a significant contribution from induced magnetization, presumably as a result of serpentinization of mantle peridotite (Twigt et al., 1983; Collete et al., 1984; Tivey and Tucholke, 1998; Hosford et al., 2003).

In this paper, we focus on anomalies over FZs in the North Pacific that separate fast to intermediate-spread crust located in the Cretaceous Quiet Zone (the term Quiet Zone will be used here when discussing oceanic crust formed in the period between chrons M0 and C34, 120.6 to 83 million years ago, respectively; Cande and Kent (1995); He et al. (2008)). The North Pacific provides an ideal location to study the origin of FZ anomalies owing to the simple polarity setting, reducing the number of edge-effects, and the good magnetic coverage available. In addition, time-dependent magnetization changes that might affect young crust near active transforms (e.g., from ongoing alteration) should be minimal in Cretaceous crust.

Archival and newly collected magnetic and bathymetry data from the Pau, Pioneer and Murray FZs (Figure 2.1), show a remarkably uniform magnetic signature for nearly 2,000 km (Figure 2.2). We examine the origin of magnetization along the FZs using forward and inverse models and show that the magnetic contrast typically originates from a one-sided enhancement of remanent magnetization. We suggest that this remanent enhancement is likely controlled by the degree of fractionation and iron content in the crust. We next show the limitations of our

model in regions where complex crustal accretion processes took place. The Pau and Pioneer FZs provide two very long records of magnetization contrasts. These magnetization variations could also preserve information about the geomagnetic field (e.g., the degree of field variability, long-term trends in the strength of the dipole) during the unique 37 m.y. Cretaceous normal superchron (CNS, the time-equivalent of the Quiet Zone). We discuss possible scenarios and inferences on the long-term geomagnetic field behavior using a set of 3D forward models. Finally, we conclude with new insights and future approaches in the study of crustal accretion near ridge-transform intersections (RTIs).

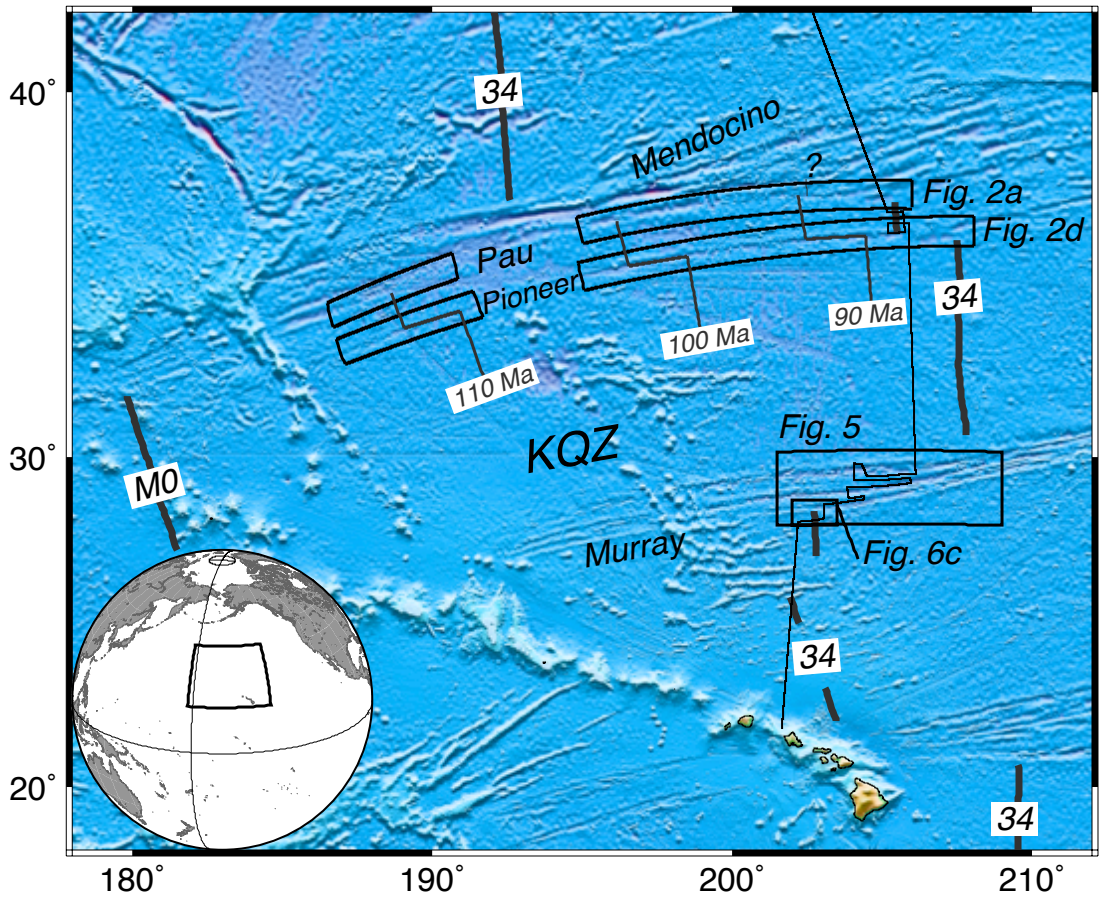

Figure 2.1: North Pacific tectonic map. Thick gray lines delineate anomalies M0 and 34 that mark the old and young edges of the Cretaceous Quiet Zone, respectively. The studied FZs are highlighted with black boxes. Thin black line outlines cruise track MGLN44MV. Thin gray lines define the interpolated ages as described in the text.

2.2 Tectonic setting

We compiled topographic and sea-surface total-field magnetic profiles collected within the Quiet Zone crust in the North Pacific, a region formed by relatively smooth spreading along the Pacific-Farallon spreading system (Atwater et al., 1993). At the end of the Cretaceous Superchron the Pacific-Farallon Ridge in this region was dominated by the right-stepping Murray FZ which offset the ridge axis about 400 km, and the left-stepping Pioneer, Pau and Mendocino FZs which collectively offset the ridge axis roughly 1000 km (Figure 2.1). The Murray FZ is topographically complex and is composed of many small-offset strands that vary in width over short distances. The Mendocino FZ in this region is also very complex, having an enormous left-stepping offset which responded to the major counter-clockwise change in plate motion around chron C33R by developing numerous high relief, short-offset ridge segments between 195°E and 210°E (Atwater et al., 1993). The Pioneer FZ has the most straightforward topographic signature; the fracture zone is generally characterized by a simple topographic step up from the older, southern side to the younger, northern side. This step is largest, roughly 500 to 700 m, in the eastern, younger end of the Quiet Zone and gradually diminishes to about 300 to 500 m, towards the western (older) end of the Quiet Zone (see Figures. 2.2e and 2.3b). Although in places the topography of the Pau FZ is characterized by a small escarpment separating the older southern side from the younger northern side, as along most of the Pioneer FZ, in the section south of the region where the Mendocino FZ developed multiple splays at chron C33R, the Pau is often characterized by a narrow ridge that can probably be attributed to extensional stresses during the ridge re-orientation (Hall and Gurnis, 2005). Cooling and subsequent subsidence of the Pacific crust has created a long wavelength (~40 km) flexural bending that overprints the initial topography of the fracture zones (Sandwell, 1984). Overall, the topography and gravity signatures of the studied FZs reflect the cumulative effects of both the spreading-related processes (e.g., by modulating the thickness of the crust) and post-spreading lithospheric processes (e.g., changes in topography related to the changes in plate motion and local mantle convections, Hall and Gurnis (2005)).

Because of the sparsity of east-west oriented magnetic lines north of the Pau FZ, the exact location of anomalies 34 and 33o between the Pau and Mendocino FZs is unknown. However, the swathmap bathymetry at 205°E shows that the orientation of abyssal hills north of the Pau FZ (Figure 2.4c) have the post C33R azimuth which constrains C33R crust to lie to the west. In addition, the large amplitude of the magnetic anomaly over the Pau FZ between 202°E and 204°E suggests that anomaly 34 is located near 202°E as we will discuss later in the text.

Spreading rates and ridge geometry are only constrained outside of the Quiet Zone edges (Figure 2.1). In the studied area, half spreading rates just prior to and just after the Quiet Zone were 50 mm/yr and 33 mm/yr, respectively. The anomaly pattern requires a ridge jump that may have taken place early in the superchron (Rea and Dixon, 1983; Atwater et al., 1993), in crust older than the crust studied here (Figure 2.1). To estimate seafloor ages within the Quiet Zone we use the half spreading rate between anomalies 34 and 33o (33 mm/yr), the width of Quiet Zone crust as measured along the Pioneer FZ (2420 km), a ridge jump (700 km) assumed to have occurred older than the oldest profile data considered here, and assume a constant deceleration to interpolate spreading rates. These assumptions result in a fast (85 mm/yr) half spreading rate for the old-end of the Quiet Zone which is 35 mm/yr faster than the rate observed for M0 to M4. Using these interpolated velocities we predicted the ages within the Quiet Zone (Figure 2.1). Shallow remanence directions and nearly east-west orientation of the FZs result in calculated magnetizations that are only slightly susceptible to the pole uncertainties. In fact, even a conservative 20° misfit in the resultant skewness angle (reflecting uncertainties in the orientation and position of the studied blocks, uncertainties in the position of the paleomagnetic poles, and uncertainties in the age of the crust) would have only a minor effect on the magnetization (see below and Figures. 2.7a and b). Therefore, although the calculated spreading rates may be an overestimate of the true rates (e.g., Heller et al., 1996) they do not affect the results of this study.

2.3 Data and methods

The magnetic anomaly data used here were gathered from the U.S. National Geophysical Data Center (NGDC) and augmented by recent magnetic, swath bathymetry, and 3.5 kHz seismic profiler data collected aboard the R/V Melville (cruise MGLN44MV). Overall, we use 180 profiles that cross the FZs at an angle larger than 45°, and extend for at least 40 km on each side of the FZ. The average sampling distance between successive magnetic measurements, which were primarily collected in the 1960s, is 1.7 km (σ = 1.5 km). The geomagnetic field at the time of acquisition of the observed magnetic profiles was subtracted using the appropriate coefficients from the International Geomagnetic Reference Field (IGRF 10; Macmillan and Maus (2005)). We used the well-navigated swath bathymetry data to constrain a best-fit line for each FZ (pseudo synthetic flow-line). These synthetic flow-lines were used as the reference for a latitudinal re-positioning of the poorly navigated profiles. The correction was based on the along-track single-beam bathymetry soundings. The average latitudinal correction was 3 km.

The magnetic data were measured above an uneven seafloor and due to the absolute northward motion of the Pacific Plate and the curvature of the studied FZs, the magnetic anomalies are increasingly skewed in the old parts of the Quiet Zone. To account for these effects we calculated equivalent magnetizations using the Fourier method of Parker and Huestis (1974). The resulting inversion solutions offer estimates of the magnetization across FZs for a uniform 1 km thick magnetic source layer. The thickness of the imaged sedimentary sequence was minimal throughout the studied area (< 50 m), allowing us to use seafloor depth as the top of the magnetic source layer. We have estimated remanence directions using the interpolated locations of chrons M0 and C34 paleomagnetic poles of Wessel and Kroenke (2008) (58°N, 350°E and 51°N, 335°E, respectively), using the estimated crustal ages as described above.

Because the results from the two-dimensional (2D) inversions are poorly constrained at long and short wavelengths, we applied band-pass filtering allowing wavelengths between 10 and 200 km to pass unattenuated. In the case of seafloor spreading anomalies the magnetization solution is often adjusted by addition of an

annihilator, a magnetization distribution for a given topography and thickness of source layer that produces no external magnetic field (Parker and Huestis, 1974), in order to balance the positive and negative sources that are assumed to be of equal magnetization. Since no such constraint is available for the FZs anomalies, we do not apply the annihilator and rather view the results as an estimate for the relative magnetization contrasts.

2.4 Magnetic observations and their inversion solutions

The magnetic anomaly profiles are remarkably uniform across the Pioneer and Pau FZs for nearly 2,000 km (Figures. 2.2a and d), with a mean peak-to-trough amplitude of 340 nT (σ = 110 nT). The 2D inversion solutions of these profiles show that an enhanced magnetization zone is located, for most of the studied area, on one side of the FZs (Figures. 2.2c and f). This zone is located on the younger, northern side of the Pioneer FZ whereas it is located on the older, southern side of the Pau FZ. These enhanced magnetization zones begin on, or very close to, the morphological slope that marks the fault-line and gradually diminish over a distance of 15 to 40 km (Figure 2.2). The absolute values of crustal magnetizations are unknown, yet the anomalies require a typical contrast in magnetization of 5 to 16 A/m (Figure 2.3) for a 1 km thick source layer. If there are no spreading discontinuities between the Pioneer and Pau FZs, as appears to be the case, one of the more intriguing observations in this study is that the enhanced magnetization zones north of the Pioneer and south of the Pau are at opposite ends of the same ridge segment.

The peak-to-trough amplitude of the 2D inversion solutions across the Pau and Pioneer FZs, when viewed with respect to their flow-line locations, provides a temporal view of the evolution of magnetization contrast during the Quiet Zone (Figure 2.3). Quantifying these temporal changes is somewhat subjective, since the amplitude of the magnetization contrast depends on the location where one picks the maximum and minimum magnetization values. Because the inversion process

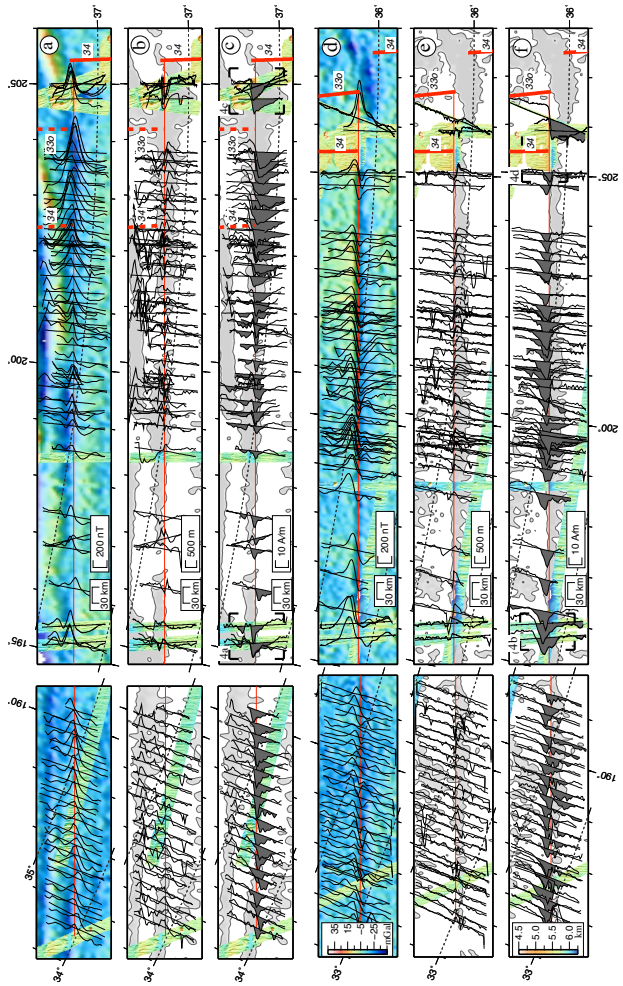

Figure 2.2: Oblique projections of Pau (a-c) and Pioneer (d-f) FZs. The observed magnetic anomalies (a,d, projected over the free-air gravity map of Sandwell and Smith (1997)), bathymetry (b,e) and 2D inversion solutions (c,f, positive shaded) are plotted with positive values projected westward, as for all the figures in this study. Locations of archival data were corrected to match the synthetic trace (thin red lines) of the FZs. Light gray shaded areas are the 15 and 25 mGal free-air gravity contours for the eastern and western plots, respectively. The corners of the black squares shown in panels c and f delineate the locations of the enlarged maps shown in Figure 2.4. All inversion models in this study assume a kilometer thick magnetic source layer starting at the seafloor depth. Other parameters: present inclination and declination was determined for every profile, remanence directions were calculated using the interpolated paleopoles of Wessel and Kroenke (2008) based on the interpolated ages shown in Figure 2.1. The track lines correspond with zero value for the anomalies and inversions panels, and with the average depth for the bathymetric panels.

applies a bandpass filter to the magnetic data, variations in the peak-to-trough amplitude of the inversion solutions may be influenced by the parameters of the bandpass filter. We measured the peak-to-trough amplitude of both the deskewed anomalies and the inversions on the side of the anomaly facing the fracture zone as a measure of the magnetization contrasts. Both of these values reveal similar patterns (Figure 2.3), confirming the minimal effect of bandpass filtering.

In general, the magnetization contrasts along the Pioneer FZ display values averaging around 8 A/m (Figure 2.3). Two episodes of higher values, averaging about 15 A/m, occur at 101 and 93-91 Ma. A zone of higher magnetization contrasts at the Pau FZ between 90 and 85 Ma is probably the result of the presence of reversed polarity crust, associated with chron C33R, located on the north side of the FZ. On crust older than 90 Ma, the average magnetization contrast across the Pau is similar to the Pioneer (about 8 A/m). Higher scatter at the Pau FZ is apparent in the western region, between 108 and 114 Ma.

Although a one-sided magnetization enhancement accounts for observations along FZs characterized by a single fault strand (e.g., Figures. 2.4c and d), the calculated magnetization deviates from the simple one-sided enhancement model in more structurally complex areas. Multiple enhancement zones appear to be present in places where the FZs are composed of multiple sub-parallel faults. Here each fault is usually associated with a single, distinctly separated enhancement zone (e.g., Figure 2.4a), but may in places also be associated with an unusually low magnetization (Figure 2.5, northern strand). A prime example of the multiple and complex magnetization setting is found near the Murray FZ, where three strands of faults are found in the Quiet Zone (Figure 2.5). These faults merge into a single fault system during the major change in plate motion that took place in chron C33R. Each strand is composed of several sub-parallel faults, which together have accommodated the lateral offset. The enhanced magnetization zone is located south of the southernmost strand (see also Figures. 2.6c and d) but is found on the north side of the two other strands. Later in the text we will further discuss the possible mechanisms that created these magnetization contrasts. For the purpose of this paper, when investigating the evolution of the magnetization contrasts,

we will focus on the Pau and Pioneer FZs as their structural and magnetization settings display a relatively simple pattern.

2.5 Discussion

2.5.1 Nature of magnetization

The magnetization contrast that generates FZ anomalies may be either remanent or induced and may vary at different spreading rates and tectonic settings. For example, the enhanced magnetization at slow-spreading segment ends may reflect a significant induced magnetization contribution (Pockalny et al., 1995; Tivey and Tucholke, 1998; Hosford et al., 2003) from serpentinized peridotites. In contrast, the thermal structure at fast-spreading transforms suggests that little serpentinization may occur (e.g., Gregg et al., 2007) since the mantle will likely be at temperatures above the stability field for serpentine (<500°C; Chen (1988); Ulmer and Trommsdorff (1995)).

Several lines of evidence suggest that FZ magnetic anomalies at fast-spreading ridges are dominantly remanent in origin. The most compelling evidence comes from the shape of the FZ anomalies, which change abruptly across isochrons (Figures. 2.2d and 2.5) implying that their magnetization is dominated by thermoremanent magnetization. If induced magnetization were dominant then the anomalies should show a pattern of positive anomalies to the south and negative anomalies to the north of the fracture zone, regardless of the polarity of magnetization of the confining crust. This predicted anomaly pattern is not observed (Figures. 2.6c and 2.7d).

To quantify the contribution of induced magnetization we make use of a modified version of the method first introduced by Tivey and Tucholke (1998). The premise that underlies this method is that magnetic blocks (single spreading segments in Tivey and Tucholke (1998); here, the confining crust of the studied FZs, Figure 2.6a) have similar magnitude of magnetizations on opposite sides of a polarity reversal (far from the boundary itself), when remanence dominates the magnetization. Therefore, adding and dividing by two the results from the inver-

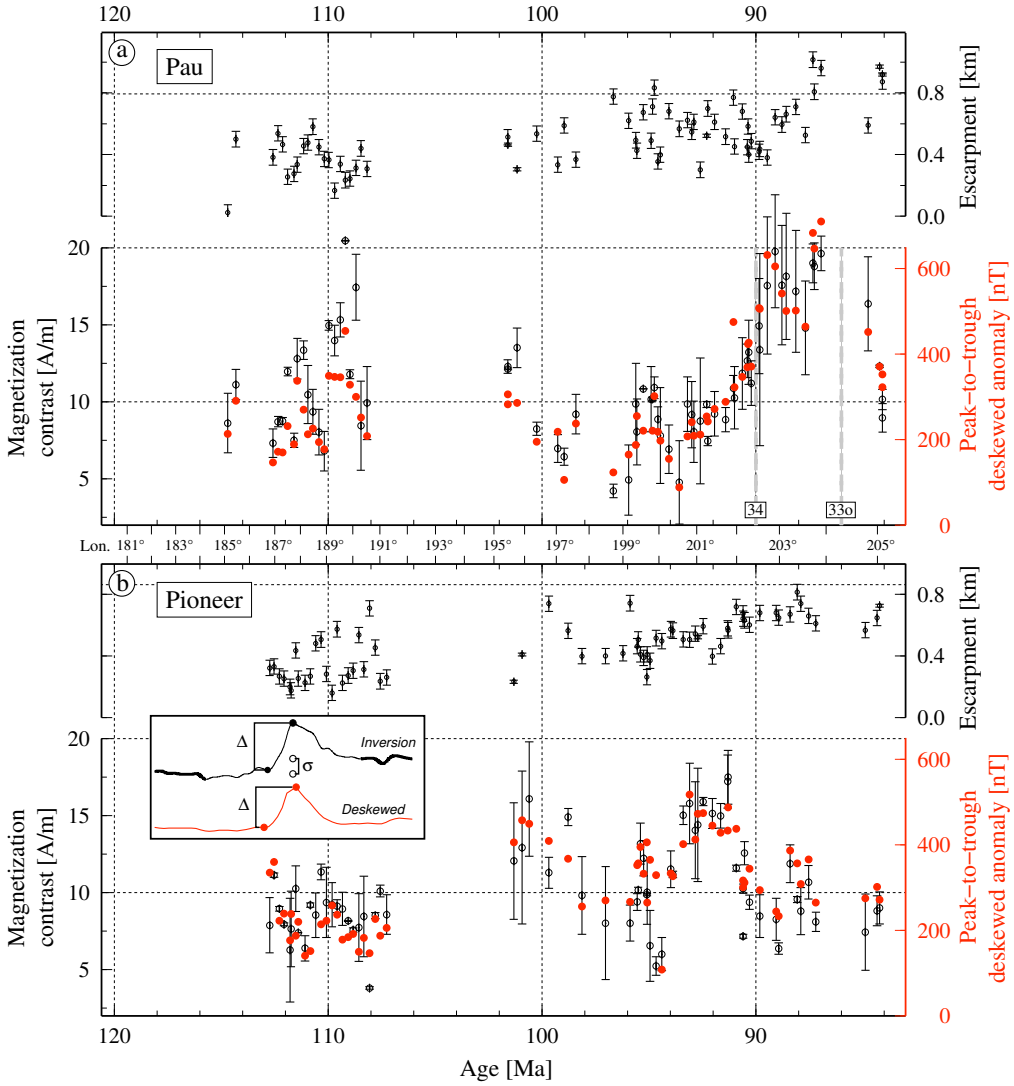

Figure 2.3: Magnetization contrasts from the Pau (a) and Pioneer (b) FZs. The upper diagrams show the topographic escarpments of the FZs as calculated from the single beam data shown in Figures. 2.2b and e. Estimates of magnetization contrasts (lower panels) were obtained using both the peak-to-trough amplitudes of the deskewed anomalies (red circles) and the hand-picked magnetization contrasts measured from the inversion solutions shown in Figures. 2.2c and f. The error bar for the magnetization contrasts is calculated by taking the difference between the average value of the first and last quintile of the profile (darker portion of the representative profile). This error estimate mimics the uncertainty of the longer wavelength signal (i.e., uncertainty in the location of the baseline), located outside the influence of the FZ magnetization. A representative profile and the corresponding estimated contrasts and error are shown in the inset. Temporal uncertainties increase from near zero in the end of the Quiet Zone to a few million years near the 110 Ma crust.

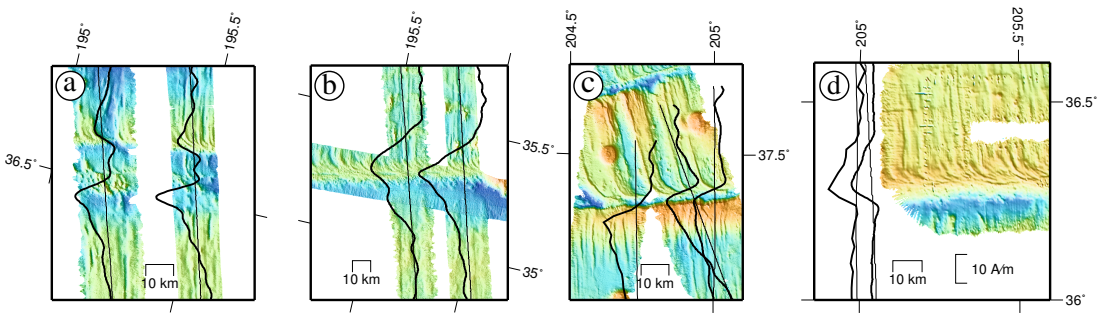

Figure 2.4: Inversion solutions from the Pau (a,c) and Pioneer (b,d) FZs illustrating how magnetization is distributed in different FZ settings. All inversion parameters are similar to the ones used in Figure 2.2. Note the difference in orientation of the abyssal hills north of the Pau (c, north-north-west to south-south-east) versus the orientation north of the Pioneer (d, north to south) that indicates that the crust north of the Pau is younger than chron C33R (i.e., formed after the major change in plate motion).

sion solutions collected across FZs and from opposing sides of a polarity reversal (i.e., isochron) provides an estimation of the amount of induced magnetization (Figure 2.6b). Similarly, the subtraction of the magnetizations from opposing sides of a polarity reversal (and dividing by two) yields the average remanent magnetization in the crust (Figure 2.6b). We carried out this approach in the southern strand of the Murray FZ, from both sides of anomaly 34, where sufficient data exist to stack multiple profiles. Presumably, local variations in the magnetic signal are averaged out by the stacked profiles (Figure 2.6d). The results from this exercise confirm that more than 90 percent of the magnetic signal originates from remanent magnetization (Figure 2.6d), with induced magnetization apparently contributing less than ~2 A/m of the magnetization contrast.

Comparison of the observed anomaly data with two- and three-dimensional forward models, near the Pioneer FZ where the location of polarity reversals is well defined, further supports a remanent magnetization as the source of the anomalies (Figure 2.7). The observed anomalies require a distinct asymmetry in the magnetization, with an elevated magnetization located north of the FZ, regardless of the polarities of the confining crust (i.e., more positive magnetization within the Quiet Zone crust and more negative magnetization within the C33R crust). Particularly the anomalies within the Quiet Zone crust, where both side of the FZs

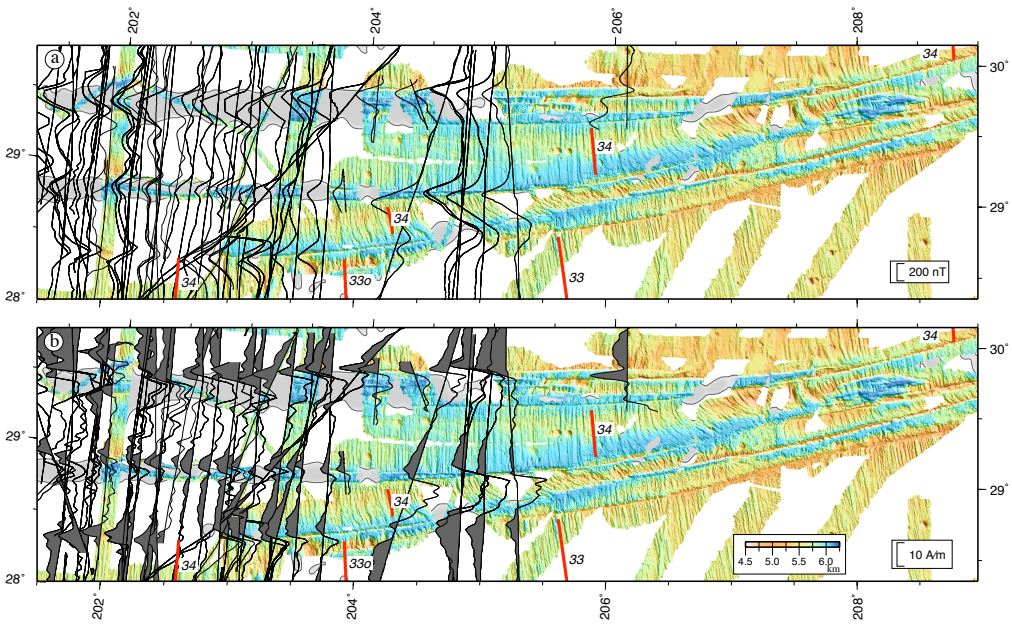

Figure 2.5: Oblique projections of the Murray FZ plotted with (a) the observed magnetic anomalies and (b) their 2D inversion solutions (positive shaded). Parameters used in the inversions and figure details are similar to the ones used in Figure 2.2.

are normally magnetized, require an enhanced magnetization zone (for example see west region of Figure 2.7d). The typical depth of 5.6 km (Figures. 2.2 and 2.5) effectively precludes the topographic step that is associated with the FZs (~500 m) as the source of the observed anomalies. For a uniform magnetization of 6 A/m and a 1 km thick source layer this topographic step generates only an anomaly of 14 nT, far smaller than the observed anomalies.

Although the observations above strongly suggest that the observed FZ magnetic anomalies are remanent in origin, it is conceivable that the remanence along the FZ might be acquired later than for crust far from the transform. Such secondary magnetization could result from chemical acquisition (e.g., alteration, hydrothermal activity) or from post-accretion volcanic activity (e.g., the leaky transforms of Menard and Atwater (1969)) that may overprint the original remanent magnetization. For example, a leaky transform near the end of the Quiet Zone might result in magnetizations with mixed polarities that would not be expected to coincide with the isochron and would probably not generate a uniform

signature over many million of years. Moreover, secondary volcanism is likely to fill the fractured area and create a magnetic signature that is centered along the FZs (e.g., Gregg et al., 2007) instead of being offset to one side. Acquisition of chemical magnetization should also have significant variability both spatially and temporally, and should result in spatial disassociation between the magnetization of FZs and isochrons. Therefore, we argue that secondary magnetization may only have a negligible contribution to the magnetization of the studied FZs.

Curved abyssal hills approach the FZs in several localities and are located on the younger side of the Pau and Pioneer FZs implying that they were accreted in the outside corner of the RTIs (e.g., see Figure 2.4). This observation suggests that curvature is not related to post-spreading shearing (transform fault-related) but rather reflects the original curved orientation of the abyssal hills (J ridges, presumably formed as a result of the change in the stress field near RTI (Morgan and Parmentier, 1984)). There is potentially a link between J ridges and geochemistry if these are formed as propagating cracks, where one might expect more fractionation (Sinton et al., 1983). The magnetization enhancement near the Pau and Pioneer FZs, located in their old and young sides, respectively (Figure 2.2), shows no spatial correlation to the curved abyssal hills (Figure 2.4). We conclude therefore that the enhancement of magnetization near the studied FZs is not dominated by vertical axis rotations (no bathymetric evidence is found for rotations) or by the propagation of ridges toward the transform faults.

2.5.2 Source of magnetic enhancement

The one-sided enhancement may result from an asymmetric thickness of magnetic source layer (e.g., ponding of extrusives at segment ends) or from a zone of iron enrichment located at segment ends. Currently, neither seismic nor geochemical data are available to distinguish these two different mechanisms in the studied area. Nonetheless, based on the characteristics of the magnetic contrasts, and on data gathered from dense surveys at the Clipperton Transform, a few initial suggestions can be made.

We can estimate the amount of source layer thickening required to account

for the observed enhanced magnetization zone in the following manner. We use two flow-line parallel magnetic anomaly profiles across anomaly 34 away from the Pioneer FZ (Figure 2.7d) to provide an estimate of the source layer magnetization. A 2D inversion of these data, assuming a source layer thickness of 1 km, yields magnetization values of 6 A/m. For anomaly profiles crossing the FZ entirely within the Quiet Zone, a uniformly magnetized layer (+6 A/m) would require an increase in source layer thickness from 1 km to 2.5 km to match the observed ~450 nT anomaly. The increase in thickness would be correspondingly less if the magnetization of the source layer were higher (corresponding to a thinner magnetic source). Since some contribution from deeper layers is likely (e.g., Dyment et al., 1997; Gee and Kent, 2007), we suggest 1 km as a plausible lower bound for the thickness of the extrusives and the portion of the sheeted dike layer that together constitute the dominant magnetic source. Although we cannot exclude the possibility that thickening of source layer could account for the enhanced magnetization, a long-lasting prominent (>1 km) contrast in the thickness of source layer, between two adjoining ridge segments seems unlikely, and has never been documented. The asymmetric high magnetization at the FZ is more likely related to geochemical variations.

Shallow (low pressure) fractionation of basaltic melt increases iron content (FeO*, total iron as FeO) (Rubin and Sinton, 2007), leading to the enrichment of titanomagnetite concentration and thus to higher rock magnetization (natural remanent magnetization, NRM) and ultimately to stronger magnetic anomalies (Vogt and Johnson, 1973; Gee and Kent, 1997). An increase of 1 percent FeO* in the basalts, formed under the present day geomagnetic field strength, leads to an increase of 6.6 A/m in NRM (Gee and Kent, 1997). This relationship, together with a 1 to 6 percent enhancement of FeO* observed near several active discontinuities and transform faults (Figure 2.8) (Sempere, 1991; Sinton et al., 1991) suggests that the 6 to 15 A/m magnetization contrasts in the Pau and Pioneer FZs can be explained by geochemical variations. An implicit assumption in this conclusion is that the geochemistry of surface lavas is broadly representative of the bulk composition of the extrusives and dikes, as suggested by limited deep drillcore

sampling (Emmermann, 1985; Teagle et al., 2006), that together may constitute the principal magnetic source.

Comparison between crustal magnetization, as calculated from sea surface anomalies (Carbotte and Macdonald, 1992), and a compiled dataset of FeO* concentrations in dredged basalts located along the ridge axis near the Clipperton Transform, East Pacific Rise (Figure 2.8), shows a fairly good correlation (Figures. 2.8b and c). Unfortunately, no detailed layer 2A thickness is available across the Clipperton Transform. Nonetheless, the correlation between the geochemical and magnetic data further support the degree of low pressure fractionation as the dominant cause of Pacific FZs anomalies, as has been argued before by investigations of fast spreading discontinuities and transform faults (e.g., Sempere, 1991; Carbotte and Macdonald, 1992; Bazin et al., 2001) and Oligocene Pacific FZs (Vogt and Byerly, 1976). Still, the underlying mechanism that generates this asymmetric iron signature at RTIs is not clear. Possible hypotheses will be discussed later in the text.

2.5.3 Complex magnetization pattern near multiple-stranded faults

Our simple model of one-sided enhancement of magnetization does not satisfactorily explain the observed signal where the FZs are made from several closely-spaced faults (Figures. 2.4a and 2.5). In these cases, each fault seems to serve as a magnetization discontinuity that is accompanied by either an increase or decrease, or both, in magnetization. The shape of anomalies located near the middle strand of the Murray FZ is consistent with the location of the area of reverse magnetization between anomalies 34 and 33o (Figure 2.5) suggesting that their magnetization results, predominantly, from remanent magnetization. A pronounced reduction in magnetization is also observed in places (for example, see northernmost strand of the Murray FZ between 202°E and 205°E, Figure 2.5). This pattern of magnetization may result from several processes. Abnormally highly fractured crust, located within these particularly faulted areas, may be associated with enhanced alteration or physical disruption that reduces the remanent magnetization. Alter-

natively, the close association between magnetization pattern and faulting (e.g., Figures. 2.4 and 2.5) may also be related to our simple model where, presumably, end-of-segment-enrichment in iron increases magnetization, even in these fine scale segments. The available data are not sufficient to produce a detailed and well-constrained magnetic model for these structurally complicated regions. Further evaluation of the magnetization, crustal and mantle structure, and geochemistry of these complex zones will require detailed and focused investigations.

2.5.4 Long-term behavior of the CNS geomagnetic field

The observed anomalies, as discussed earlier in the text, reflect the original crustal accretion processes that took place near the RTIs. Although variability in these processes undoubtedly contribute to fluctuations in anomaly amplitudes across the FZs, the magnetization contrasts should also reflect variations in geomagnetic intensity when the source rocks were magnetized. The FZ magnetic anomalies from the North Pacific therefore may provide information about the geomagnetic field during the CNS, a particularly interesting interval, as it constitutes one extreme end member of geomagnetic field behavior, when a stable normal polarity state prevailed for 37 million years.

The strength and variability of the CNS field have been the focus of numerous studies using both absolute and relative paleointensity methods (e.g., Pick and Tauxe, 1993; Cronin et al., 2001; Tarduno et al., 2001; Tarduno and Cottrell, 2005; Granot et al., 2007). These studies have yielded contradictory views of the geomagnetic field. Some studies have suggested very high dipole moments accompanied by low (<10 percent) variability about the average field (Tarduno et al., 2001, 2006), consistent with the prediction made by numerical geodynamo simulations (e.g., Glatzmaier et al., 1999). Other studies have suggested lower dipole moments and higher (>40 percent) field variability (Riisager et al., 2003; Zhao et al., 2004; Tauxe, 2006; Granot et al., 2007; Zhu et al., 2008), implying that the behavior of the superchron field is comparable to the observed Cenozoic geomagnetic field, a time of frequent reversals (Selkin and Tauxe, 2000). Part of the controversy is linked to the reliability of the magnetic recording media but

partly it is linked with sparse temporal sampling.

Marine magnetic anomalies provide an alternative means to investigate geomagnetic intensity fluctuations since they can provide nearly continuous and spatially/temporally averaged estimates of the geomagnetic field (Gee and Kent, 2007). Despite uncertainty in crustal accretionary processes that affect the magnetic anomalies over FZs, some aspects of geomagnetic field behavior may still be discernable.

To illustrate the types of geomagnetic behavior that might be recovered, we generated 3D forward models for various crustal magnetization patterns (Figure 2.9), where the crustal magnetization is proportional to the geomagnetic intensity (with Gaussian noise). We used an average crustal magnetization of 6 A/m (based on the magnetization contrast at anomaly 34), with the exception of the model shown in Figure 2.9b where the average strength was set to be highest (12 A/m) in the center of the Quiet Zone. The magnetic source geometry simulates the setting of the Pau and Pioneer FZs, where one side of the FZ has enhanced magnetization of up to 70 percent relative to the background magnetization.

Results of the first forward model (Figure 2.9a) illustrate that large amplitude, long period geomagnetic intensity fluctuations appear to be incompatible with the pattern of FZ anomalies in the Quiet Zone. The geomagnetic field for this model has large (50% of mean) 5 m.y. sinusoidal variations and small (10% of mean) Gaussian noise on shorter time scales. Such a field model produces magnetization contrasts where the side of higher magnetization changes frequently (from north to south and vice versa). This magnetization setting may yield both positive and negative magnetic anomalies (Figure 2.9a, right), in conflict with the observed uniform polarity of anomalies across the Pau and Pioneer FZs. Although low Gaussian noise was chosen to highlight this effect, the same pattern of mixed positive and negative anomalies would also be present for any field variation models that result in the lower (but still positive) magnetization crust occurring on alternate sides of the FZ. These results suggest that the long wavelength magnetization contrasts along the Pau and Pioneer FZs (Figure 2.3) are unlikely to be the result of long period geomagnetic intensity fluctuations.

Magnetic anomaly variations along FZs might also allow some proposed correlations between geomagnetic intensity, variability and reversal frequency to be addressed. Some geodynamo numerical models predict that the geomagnetic field during superchrons is both stronger and less variable than the field in times with frequent reversals (e.g., Glatzmaier et al., 1999). Alternatively, other studies of the geomagnetic field argue that the characteristics of the field during superchrons are fundamentally similar to the field at times of frequent reversals (e.g., Ryan and Sarson, 2007). Although neither the numerical models nor paleointensity data from rock samples provide any specific predictions of long-term variations within the Quiet Zone, Figure 2.9b illustrates how FZ anomalies might show whether a slow (long wavelength) increase or decrease in geomagnetic intensity took place within the superchron. The geomagnetic field for this model has lower intensity and higher variability (60% of mean) at the ends of the superchron and significantly higher intensity and lower variability (10% of mean, as suggested by some absolute intensity estimates; e.g., Tarduno et al. (2001, 2006)) in the middle of the superchron. The predicted evolution of magnetic contrasts (Figure 2.9b, right) does not bear a resemblance to the observations (Figure 2.3), illustrating how such long-term variations might be tested with FZ anomalies. Since no mutual long wavelength ($>$ 10 m.y.) trends are observed in the Pau and Pioneer FZs (Figure 2.3), we conclude that overall, the strength of the geomagnetic field in the CNS was relatively steady, at least for the period younger than 114 Ma.

Finally, the variability of geomagnetic intensity should also be reflected in the variability of magnetization contrasts across FZs (Figure 2.9c). Variability of 80% in the geomagnetic field about its average overestimates the observed scatter in the FZ magnetic anomalies. Fifty to twenty percent variability predicts a typical 5 to 3 A/m scatter, respectively, similar to the typical spread of our calculated contrasts (Figure 2.3). We therefore deduce that the long-term variability of the geomagnetic field during the Cretaceous superchron likely was not larger than ~50%. Variability smaller than 20% cannot be implicitly excluded as some of the observed scatter may result from crustal accretion variability. CNS paleointensities from sediments (Cronin et al., 2001) and igneous rocks (e.g., Granot et al., 2007;

Zhu et al., 2008) have shown similar range of variability (40-60% of mean). Our observations, however, suggest that this variability lasted for 30 million years and further support the notion that the variability of the geomagnetic field in the Cretaceous superchron was probably similar to the variability at times with frequent reversals.

2.5.5 Tectonic implications

Our observations indicate that the Pacific FZs are characterized by enhanced remanent magnetization zones located on one side of each of the FZs, for thousands of kilometers (Figure 2.2). The enhancement in magnetization may be explained by an increase in the degree of fractionation at segment ends, leading to iron-rich melts (our preferred model), or alternatively, by thickening of the magnetic source layer. The resultant magnetic anomalies therefore provide a very valuable insight into the long-term crustal construction (e.g., melt delivery). The consistency of magnetic anomalies across the Pioneer and Pau FZs suggests that spatially stable asymmetry in crustal construction across transform faults prevailed for more than 30 million years. Although not fully understood, these inferences require some fundamental crustal accretion processes to take place near the RTIs. A persistent increase in fractionation toward the end of segments may indicate that delivery of magma along-axis is an important mechanism at fast spreading ridges (i.e., three-dimensional magma accretion along ridge segments).

Why is there a persistent asymmetry in crustal construction across transform faults? Our results from the left-stepping Pau and Pioneer FZs illustrate that the enhancement in fractionation can be located either on the old or young side of the FZs, respectively (Figure 2.10). In fact, these two FZs confine a single spreading segment where a long-lasting enhancement prevailed at both ends of the segment. Transform fault effect (i.e., cold edge effect) should result in symmetric accretion patterns across discontinuities and consequently cannot explain the observed magnetic signature. Asymmetric morphology, geochemistry and crustal structure properties across active ridge discontinuities (e.g., Langmuir and Bender, 1984; Langmuir et al., 1986; Macdonald et al., 1988) have recently been attributed

to the migration of spreading centers over the mantle (Carbotte et al., 2004) where the leading segment preferentially entrains melt while the trailing side (i.e., end of the other adjoining segment) suffers from a relative reduced melt supply. Alternatively, Toomey et al. (2007) have suggested that differences between the axes of mantle upwelling and spreading direction modulate the magmatic construction at spreading segments. The link, if any, between absolute plate motion and crustal accretion over long periods of time is still unclear. Since both the Pioneer and Pau are left-stepping transforms, there is no obvious correlation between crustal magnetization and ridge geometry, although rigorous analysis of magnetic anomalies across the Pacific FZs within and outside the Quiet Zone should provide new insights into this enigma.

The observed magnetization contrasts along the Pau and Pioneer FZs reveal oscillations over time scales of some 2 to 5 m.y. (Figure 2.3). The crust juxtaposed across these FZs (i.e., formed at the adjoining segments, north and south of the Pau and Pioneer FZs, respectively) differs in age by some ~10 million of years. Long period (longer than few hundred thousands of years) variations in geomagnetic field intensity are an unlikely source for these fluctuations as they will likely result in anomalies alternating on the north or south sides of the FZ (Figure 2.9a). On the other hand, variations in the degree of shallow fractionation could theoretically produce variations in the observed magnetic contrasts but still maintain a uniform shape of anomalies. Therefore, the long period magnetic records shown here may document variations in the degree of fractionation (or possibly melting) and crustal accretion. The longest geochemical records from fast-spreading crust covers ~800 ka (Batiza et al., 1996) and indicate that temporal variability in fractionation (~2% MgO) can be of the appropriate order to explain our observed oscillations. Geophysical as well as geochemical observations from the Vema Transform fault (Bonatti et al., 2003) suggest that dynamic pulses of mantle upwelling and melting lead to variable crustal properties on a scale of millions of years. A similar mechanism may control the observed magnetic record along the studied fast spreading FZs.

The magnetization contrast across FZs can also be used to better locate the

plate boundary, as opposed to the longer wavelength, topographically controlled and overprinted gravity signal. For instance, profile y-y (Figures. 2.7b and d) crosses the Pioneer FZ where no obvious topographic (measured with multi- and single beam) or gravity signature can be used to locate the fault. Yet, the narrow magnetic contrast calculated along the profile constrains the location of the fault at this particular place (Figure 2.7d, the steepest gradient is indicated with star). Indeed, the predicted location aligns well with the observed trace of the FZ found to the west of the profile.

2.6 Conclusions

Systematic analysis of magnetic anomalies observed across the North Pacific FZs, within the Quiet Zone crust, reveals a remarkably uniform shape over 30 million years. These anomalies can be modeled with an enhanced remanent magnetization zone located mostly on one side of the FZs. The most likely cause of this zone is an increase in the degree of fractionation at one of the confining segment ends, which, in turn, implies long-lived asymmetric crustal construction. 3D magnetic forward modeling suggests that geomagnetic field intensity in the Cretaceous superchron had a typical variability of 50 percent or less about its average. The observed magnetization contrasts are on the order of 8 A/m for most of the Cretaceous superchron suggesting that the dipole strength remained, overall, near constant. Therefore, if the CNS field was associated with higher dipole moments, then the decrease to Cenozoic magnitudes might be discernable with additional FZ magnetic profiles near the end of the CNS and over younger crust.

The presence of long-lasting enhanced zones of remanent magnetization confined to one side of a fracture zone may provide constraints in models of melting accretion near RTIs. Oscillations of 2 to 5 m.y. in the observed magnetizations at the Pau and Pioneer FZs most likely reflect crustal accretion dynamics. The magnetic signature of FZs formed along intermediate to fast spreading axes can potentially be used to study the long-term effect of absolute plate motion on crustal construction at RTIs.

2.7 Acknowledgments

We thank Captain C. Curl, the crew, and the science party for their great support during cruise MGLN44MV on board R/V Melville. The cruise was supported by the University of California Ship Funds program (awarded to R. G.). Additional support was provided by NSF OCE0452610. Most figures and many of the calculations were made using GMT software (Wessel and Smith, 1998). We thank J. Dyment for his comments and two anonymous reviewers for their constructive reviews.

The text of this chapter, in full, is a reformatted version of the mate- rial as it appears in *Earth and Planetary Science Letters*, R. Granot, S. C. Cande, and J. S. Gee, The implications of long-lived asymmetry of remanent magnetization across the North Pacific fracture zones, In-press.

I have led the collection of the new and archival data. I also calculated all forward and inverse modeling, and interpreted the results. Steve Cande and Jeff Gee provided codes for the two- and three-dimensional forward and inverse modeling and gave continuous advise.

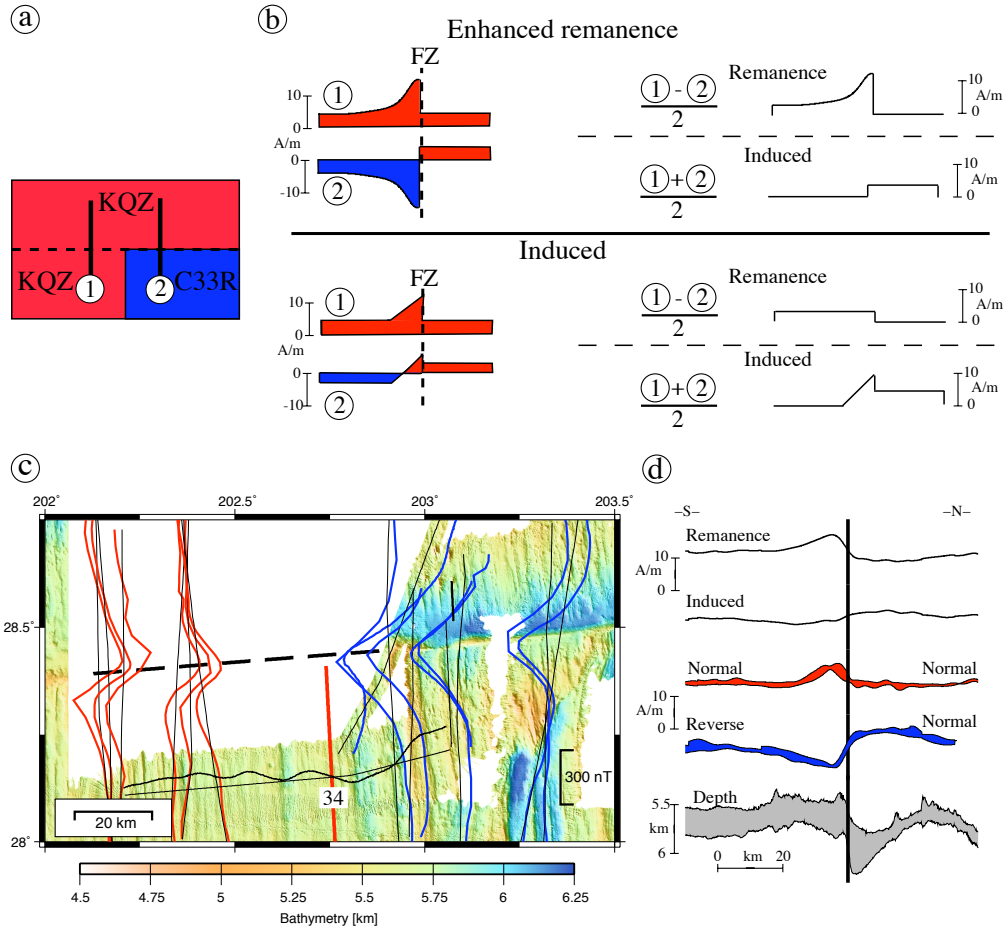

Figure 2.6: Data from the southern strand of the Murray FZ illustrating how induced and remanent magnetization contributions may be estimated. a) Schematic magnetization pattern near the southern strand of the Murray FZs and the location of two representative profiles shown in panel b. b) Two conceptual end-member models of magnetization setting (left) with their predicted results shown on the right. The upper model assumes only enhanced remanence as the source of the anomalies whereas the lower model assumes that the anomalies result from induced magnetization near the FZ. c) Observed magnetic anomalies, positive values are projected westward, color coded with respect to the two stacks. d) Stacks of the bathymetry and 2D inversion solutions shown in panel c. Stacks of the solutions west (red, 6 profiles) and east (blue, 7 profiles) of chron C34 are shown with standard errors. The resultant calculated remanence contribution is shown in the top most plot. Contribution from induced magnetization is shown below. Tie point used in the stacking procedure was the steepest gradient of bathymetry.

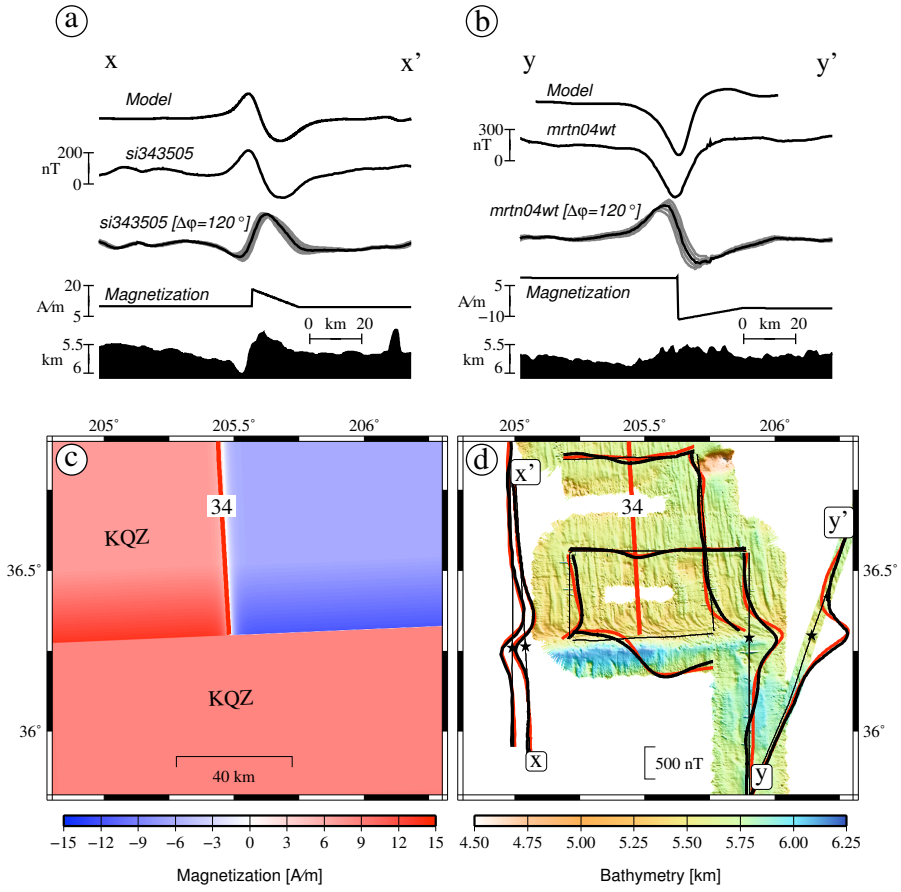

Figure 2.7: The enhancement in remanent magnetization north of the Pioneer FZ (straddling the end of the Quiet Zone), as been calculated using 2D and 3D forward modeling. a,b) Projected bathymetric (shaded) and magnetic profiles compared to magnetic 2D forward models. The four profiles are from bottom to top: magnetization setting used in the forward models, deskewed anomalies, observed anomaly, and result from the forward 2D modeling. Gray lines in the pole-reduced profile illustrate the effect of 20° uncertainties in theta that result from uncertainties in the paleomagnetic pole position and location of the ridge axis at the time of accretion. Locations of these profiles are shown in panel d. The bathymetric profiles were used as the top of a kilometer thick magnetic source layer. c) Magnetization setting for the 3D forward modeling shown in panel d. d) Predicted anomalies (red) as calculated by 3D forward modeling and compared with the observed anomalies (black) projected over the bathymetry that was used in this model (1 km source layer). The anomalies are plotted with positive values projected westward. Black stars delineate the location where the gradient of magnetization is steepest as calculated from the 2D inversion solutions. Gaussian smoothing across the reversal boundary is 2 km. The northern two flow-line profiles were used to calculate magnetization of 6 A/m at the crust located far from the fracture zone.

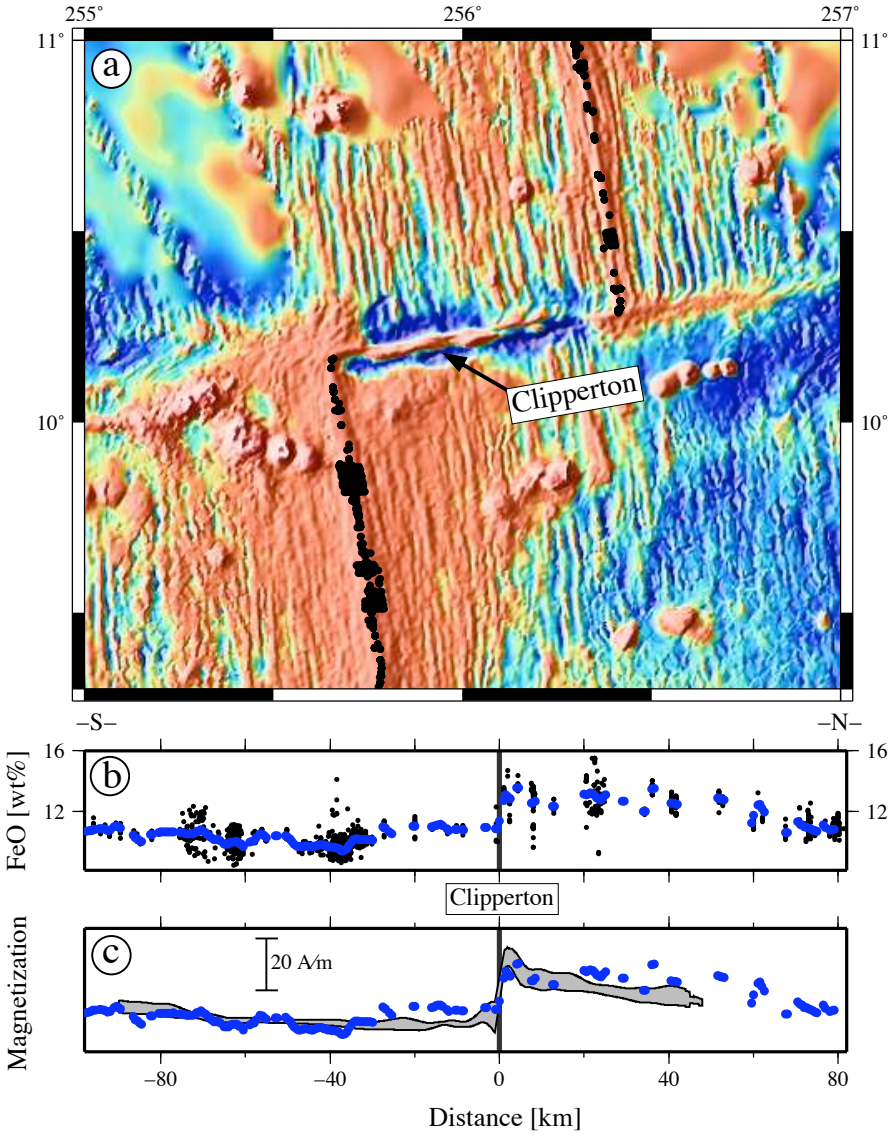

Figure 2.8: Comparison between FeO* content in dredged basalts and results from magnetic inversions near the Clipperton Transform fault. a) Bathymetric map with dredge locations (black dots). All dredges are located within 3 km from the ridge axis. Data from PetDB, www.petdb.org. b) Iron (FeO*) content of the dredged rocks shown in panel a are indicated by the black dots. Running average is determined every 1 km, filtered with a cosine arch width of 4 km (blue dots). c) Comparison between crustal magnetizations (gray shaded area) and the predicted magnetization (blue dots). Crustal magnetizations are based on the 3D inversion from Carbotte and Macdonald (1992). We calculated ridge parallel profiles every 10 km within the Brunhes and stacked them to get the average magnetization of the crust (gray shaded area delineates the standard error). The predicted magnetization is based on the running mean FeO* content of the dredge samples shown in panel b and the relationship of Gee and Kent (1997).

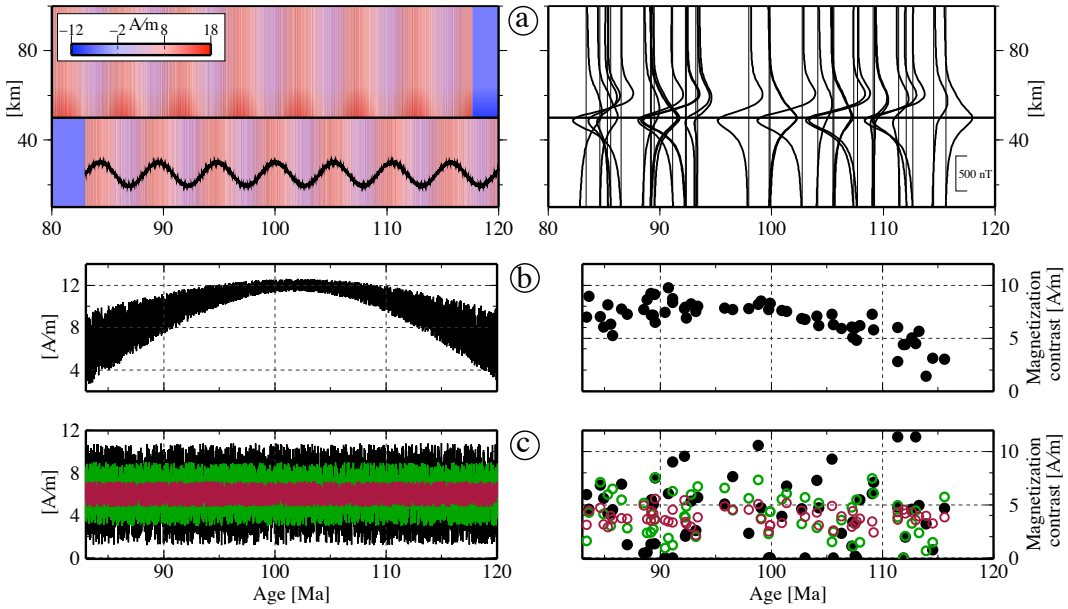

Figure 2.9: Three-dimensional forward models illustrating different Quiet Zone geomagnetic field behavior scenarios and their resultant magnetic anomalies across FZs. a) Magnetization model (left, map view) for periodic variation in geomagnetic strength coupled with enhanced magnetization (70% higher north of FZ, black line). Average strength of magnetization is 6 A/m. Note that a geomagnetic field with a typical cyclicity of 5 m.y. shown here produces mixed anomalies (shown at right). b) A representative model (left diagram, same geometry as in (a)) that illustrates a possible behavior of the geomagnetic field within superchron inferred from some geodynamo numerical simulations. The predicted magnetization contrasts (calculated as in Figure 2.3) are shown in the right diagram. c) Models illustrating the effect of geomagnetic (and magnetization) variability (purple = 20%, green = 50%, black = 80% about 6 A/m mean). The predicted magnetization contrasts are shown in the right diagram. All models used these parameters: thickness of source layers is 1 km starting at constant depth of 5.6 km. Present inclination (Io= 53.8°); present declination (Do = 13.6°); remanent inclination (Ir= 20.4°); remanent declination (Dr = 17.2°). Pixels sizes are: 0.6 km perpendicular to spreading direction; 10 kyr along spreading direction.

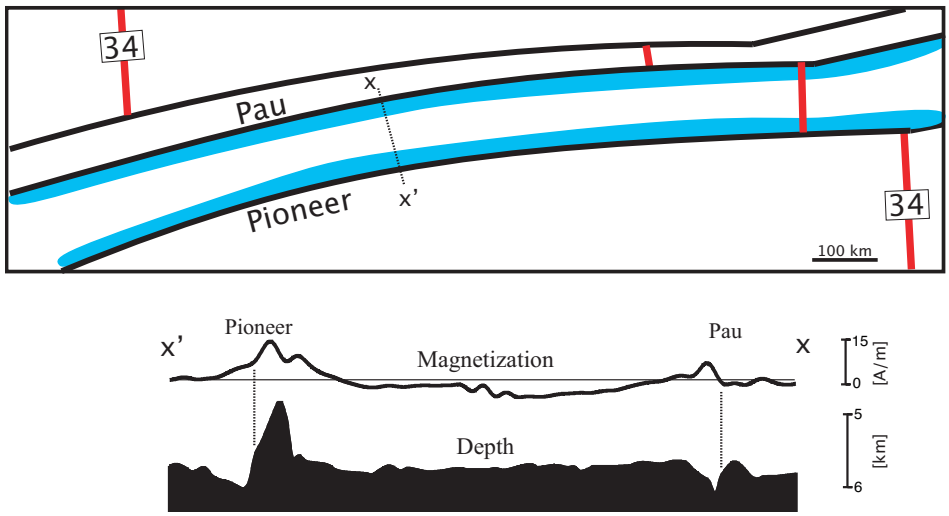

Figure 2.10: Cartoon illustration of the magnetization setting in the North Pacific Quiet Zone crust. Enhanced magnetization zones are marked with light blue. Red lines delineate the location of the Pacific-Farallon ridge at the end of the Quiet Zone (anomaly 34). A stable enhancement of magnetization prevailed at both ends of the segment that separate Pau and Pioneer FZs for more than 30 m.y. A representative bathymetric (shaded) and the corresponding magnetization profile are shown below.

Chapter 3

Post-spreading rifting in the Adare Basin, Antarctica: Regional Tectonic Consequences

Abstract. Extension during the middle Cenozoic (43–26 Ma) in the north-end of the West Antarctic rift system (WARS) is well constrained by seafloor magnetic anomalies formed at the extinct Adare spreading axis suggesting a southward decrease in relative motion. But how the rift system evolved during the Neogene to its present-day seemingly locked state is still poorly resolved. Here we present results of multichannel seismic reflection and seafloor mapping data acquired within and near the Adare Basin on geophysical cruise NBP0701 aboard the R/VIB Nathaniel B. Palmer. We have traced the ANTOSTRAT seismic stratigraphic framework from the northwest Ross Sea into the Adare Basin, verified and tied to DSDP drillsites 273 and 274. Our results reveal three distinct periods of tectonic activity. An early discrete deformational event took place shortly after spreading stopped. It reactivated a few normal faults, and uplifted the eastern side of the Adare Trough. There are no indications that this event is linked to deformation outside the basin. A prominent pulse of localized rifting in the early Miocene (~17 Ma) resulted in normal faulting that initiated tilted blocks. The overall trend of structures was NE-SW with little resultant E-W extension. The spatial distribution of faults links the event with the activity outside the basin.

It resulted in major uplift of the western flank of the Adare Trough and marks the last extensional phase of the Adare Basin. Recent volcanic vents (Pliocene to present-day) are distributed throughout the basin but tend to align with the early Miocene structures and the on-land Hallett volcanic province. This latest phase of tectonic activity also involves near vertical normal faulting (still active in places) with negligible horizontal consequences. The early Miocene extensional event found within the Adare Basin does not require a change in the relative plate motion of the WARS, but the lack of subsequent rifting, the 13 Ma Terror Rift formation, on-land normal faulting found in the northern Victoria Land, Neogene extension within the deep interior ice-filled troughs and basins of West Antarctica, and a northward age initiation of volcanism along the northern WARS, require a pronounced change in the kinematics of the rift. These observations indicate that extension increased southward, therefore suggesting that a major change in plate motion took place in the middle Miocene. The late Miocene pole of rotation might have been located north of the Adare Basin, with opposite opening sign compare to the Eocene-Oligocene pole. Interestingly, our proposed Neogene tectonic evolution of the Adare Basin is correlated with the detailed temporal kinematic framework of the Pacific-Antarctic ridge.

3.1 Introduction

The West Antarctic rift system (WARS) separates cratonic East Antarctica from younger blocks that assembled to form West Antarctica in the late Mesozoic (Heimann et al. (1994), Figure 3.1). Cenozoic rifting has probably influenced the denudation history of the Transantarctic Mountains (TAM), the uplifted rift flank of the WARS (e.g., Fitzgerald and Stump, 1997; ten Brink et al., 1997), and consequently influenced the growth of the Antarctic cryosphere (Behrendt and Cooper, 1991; Van der Wateren and Cloetingh, 1999). The WARS also plays an important role in the global plate circuit and has long been recognized as a missing link in many plate reconstruction models (e.g., Molnar et al., 1975). There is still considerable debate regarding the kinematic history of the rift for most of its

existence.

The Adare Basin, located north of the western Ross Sea (Figure 3.1), was formed along a seafloor spreading center (Cande et al., 2000) that was active between chrons C20 and C9 (middle Eocene to late Oligocene, 43 to 26 Ma, Cande and Kent (1995)). Structural continuity between the Adare Basin and Northern Basin (e.g., Cande and Stock, 2006) implies that the kinematic solutions calculated for the Adare seafloor spreading (Cande et al., 2000; Davey et al., 2006) provide crucial constraints for the Eocene - Oligocene motions of the entire rift system. The post-spreading extensional activity within the Adare Basin, as recorded by sediments, bathymetry, and offset of magnetic lineations, may therefore provide valuable insights on the Neogene kinematics of the WARS, a poorly resolved period in the history of the rift.

Here we present a grid of multichannel seismic (MCS) reflection data as well as bathymetric mapping results from geophysical cruise NBP0701 aboard the R/VIB Nathaniel B. Palmer. We first present a correlation of seismic stratigraphic units from the Northern Basin into the Adare Basin of the Ross Sea following the stratigraphic framework set by Brancolini et al. (1995), which was verified and tied to DSDP drillsites 273 and 274. Although our approach suffers from notable limitations, particularly for the oldest, late Oligocene parts of the section, it still yields important temporal constraints on the Neogene evolution of the Adare Basin. We then assess the tectonic evolution of the Adare Basin and identify three major events: 1) a localized fault-reactivation event that occured a few million years after spreading stopped, 2) an early Miocene localized extensional event charachtarizd by tilted blocks and normal faulting, and 3) a period of Pliocene to present-day extensive volcanism that, together with near-vertical normal faults, marks the last phase of deformational activity in the Adare Basin. We then discuss the implications of our results for the kinematics of the WARS during the Neogene. Finally, we conclude with a comparison of our results to the regional kinematic framework.

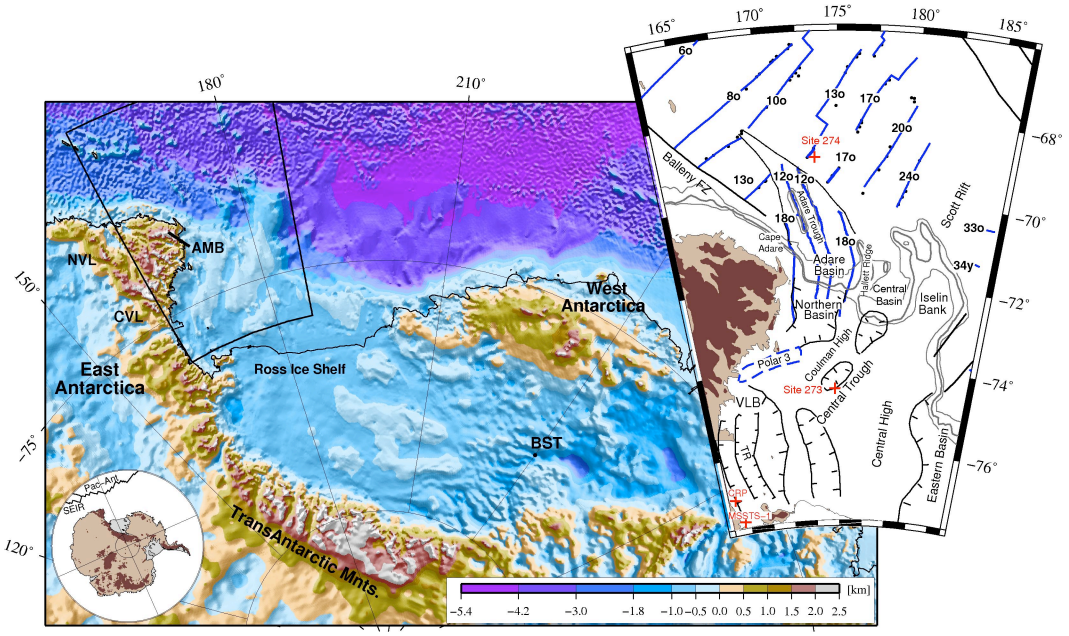

Figure 3.1: Tectonic setting and location map of the West Antarctic rift system. Elevation and bathymetry are based on the BEDMAP compilation of Lythe and Vaughan (2001). Large inset shows the main structural elements of the Adare Basin and western Ross Sea. Blue lines delineate magnetic lineations. Anomalies 18o and 12o run continuously from the Adare Basin into the Northern Basin (based on archival shipboard magnetic data and aeromagnetic data of Damaske et al., 2007). Dashed blue line denotes large magnetic anomaly (Polar 3). Locations of drillsites are shown with red crosses. NVL, Northern Victoria Land; AMB, Admiralty Mountains block; CVL, Central Victoria Land; BST, Bentley Subglacial Trench; SEIR, South East Indian Ridge; Pac-Ant, Pacific-Antarctic ridge; VLB, Victoria Land Basin; TR, Terror Rift. Gray lines delineate the 1000, 1500, and 2000 m contours.

3.2 Tectonic Setting and History of the West Antarctic Rift System

The middle Jurassic continental flood basalts of the Ferrar Group, found along the TAM, provide the first evidence for the break-up of Gondwanaland and the isolation of the Antarctic continent (Heimann et al., 1994). Paleomagnetic measurements suggest that there has been a total of 500 to 1000 km of transtensional motion between West and East Antarctica since middle Cretaceous (Divenere et al., 1994; Luyendyk et al., 1996). Reworked Cretaceous marine sediments (Truswell

and Drewry, 1984) and dredged mylonites (Siddoway et al., 2004) mark the late Mesozoic phase of broad subsidence and rifting of the Ross Sea sector that is linked to the progressive fragmentation of Gondwanaland. During the late Cretaceous and early Cenozoic, N-S trending basins (Eastern Basin, Central Trough, Victoria Land Basin, and its northern continuation - Northern Basin) and ridges (Coulman and Central Highs) were formed within the subdued Ross Embayment (Ross Sea and Ross Ice Shelf, Cooper et al. (1987), Figure 3.1). Extension north of the Ross Sea may have been partly accommodated by counterclockwise rotations of the Central Basin and Iselin Bank sector (Cande and Stock, 2004a).

Additional middle Cenozoic opening and subsidence was focused in the western Ross Sea (Northern Basin and Victoria Land Basins, NB and VLB, respectively, Cooper and Davey (1985); Davey and Brancolini (1995), Figure 3.1). Total extension within the VLB was estimated to be 95 km (Davey and De Santis, 2006). Fission track dating of basement apatite suggests that this phase of rifting was accompanied by an increase in denudation rates of the TAM (Fitzgerald et al., 1986; Gleadow and Fitzgerald, 1987).

The transition from the early Cenozoic diffuse extension to the localization of rifting in the western part of the Ross Sea has been recently explained by thermal evolution of the rift zone where progressive cooling and hardening have led to lithospheric necking along the East Antarctic plate boundary (Huerta and Harry, 2007). Alternatively, although not required by numerical models, localization of deformation may have been driven by changes in plate motions (Wilson, 1995) or by the impingement of a mantle plume (Behrendt et al., 1994). Based on extensive on-land and limited offshore seismic observations, major NW-SE dextral strike-slip intraplate faults in the northern Victoria Land (NVL) has been suggested to crosscut the N-S structures (e.g., Salvini et al., 1997; Rossetti et al., 2006; Storti et al., 2006, 2007). These studies have argued that, in-fact, NW-SE dextral strike-slip motion was the dominant mechanism of deformation within and near the Ross Sea sector since Eocene time. Our new data from the Adare Basin, as will be discussed later in the text, do not support this hypothesis.

Adjacent to the continental slope from the north, the Adare Basin is lo-

cated in-line with the NB and is characterized by resolvable linear marine magnetic anomalies (anomalies 11 to 18, Cande et al. (2000); Damaske et al. (2007)). These anomalies elucidate the fossil Adare spreading center, the slowest arm in a ridge-ridge-ridge triple junction (Cande et al., 2000). Seafloor spreading took place at constant and asymmetric spreading rates: 7.5 mm/yr and 5 mm/yr in the east and west flanks of the basin, respectively (Cande et al., 2000). Spreading accounted for 170 km of ENE-WSW plate separation. Continuous magnetic anomalies (Damaske et al., 2007), Bouguer gravity anomalies, and undisrupted sedimentary sequences across the shelf south of the Adare Basin (Cande and Stock, 2006) suggest that the opening of the basin was accompanied by the opening of the NB where massive and focused magmatic intrusions were likely to have been emplaced. Using gravity data and limited seismic reflection data, Muller et al. (2005) showed that the formation of the Adare Trough, an uplifted structure located within the Adare Basin (frequently misinterpreted as a remnant of the ridge axis, Figure 3.2), resulted, in-fact, from fault reactivation during the first 5 m.y. after spreading stopped. Muller et al. (2005) also concluded that no significant extension took place in the Adare Basin afterwards, i.e., during the Neogene.

The latest phase of extension in the Ross Sea was concentrated in the Terror Rift, a middle Miocene narrow rifted zone located within the VLB (Cooper et al. (1987), Figure 3.1). The Terror Rift has accommodated 10 to 15 km of extension (Henrys et al., 2007) since 13 Ma (Fielding et al., 2006, 2008). A pronounced middle Miocene extensional phase is also evident in the Admiralty Mountains block, located immediately southwest of the Adare Basin (Figure 3.1, Faccenna et al. (2008)). There, a total of 5 km of extension was accommodated along a set of NE-SW to N-S trending normal faults (Faccenna et al., 2008). Further south, sub-ice deep troughs and basins filled with thin layers of sediments (Figure 3.1, Anandakrishnan and Winberry (2004)) have been speculated to have formed underneath the Ross Ice Shelf (LeMasurier, 2008), suggesting Neogene formation. These tectonic events were accompanied by an extensive Neogene bimodal alkalic volcanic activity that is also found in the western Ross Sea (LeMasurier, 1990).

Present-day high heat-flow (Blackman et al., 1987; Della Vedova et al., 1991)

and low seismic velocities (Watson et al., 2006) observed within the western Ross Sea have been attributed to the late Cenozoic rifting and thinning of the West Antarctic lithosphere. Yet, lack of seismic activity (Behrendt et al., 1991) and minor present-day displacements (Donnellan and Luyendyk, 2004; Zanutta et al., 2008) testify that the rift system is currently nearly locked. How the Neogene rifting evolved into the present-day state of inactivity of the WARS still remains to be resolved and is the focus of this work.

3.3 Data Collection and Processing

We collected a grid of more than 2,700 km of two-dimensional MCS reflection data together with multibeam bathymetric mapping (using Simrad EM 120) within the Adare basin and across the shelf (Figure 3.2) during a recent geophysical cruise (NBP0701). The typical line spacing was 20 km. Our new MCS dataset is complemented by ~500 km archival MCS data (available through the Antarctic Seismic Data Library System, http://sdls.ogs.trieste.it/), amounted to a total of 3,200 km of reflection profiles that allow us to tie the seismic grid to the closest DSDP drillsites 274 and 273 (Figure 3.2). Additional data collected during the cruise, including sonobuoy refraction, gravity, and dredged rocks, will be discussed elsewhere.

Seismic reflection data were acquired with a 1200 m oil-filled streamer. For most of the profiles, the seismic energy source was an array of six generator-injector air guns with a total capacity of 22.1 liters. In shallower water of the Ross Sea shelf, we used an array of six Bolt air guns with a total capacity of 34.8 liters. Data were recorded on 47 (out of 48) channels. The data were 8 second records with 0.002 second sample rate and a shot spacing of approximately 28 meters (43 meters for the lines collected on the shelf). Processing of the data included velocity semblance analysis every kilometer on common depth point (CDP) gathers. Subsequent processing included stacking and F-K migration. Exponential gain ($\alpha = 0.5$) was finally applied to increase imaging of the deep structures. For the profiles that crossed the shelf we applied a Time Variant Butterworth Filter and

a parabolic Radon transform (Hampson, 1986) prior to stacking, to reduce the energy of multiples. This resulted in resolvable primary arrivals as deep as ~2.2 seconds two-way travel time. The final seismic results, together with the archival data, were then imported into Kingdom Suite software for interpretation. Paper prints were also used for interpretation and served as a quality control.

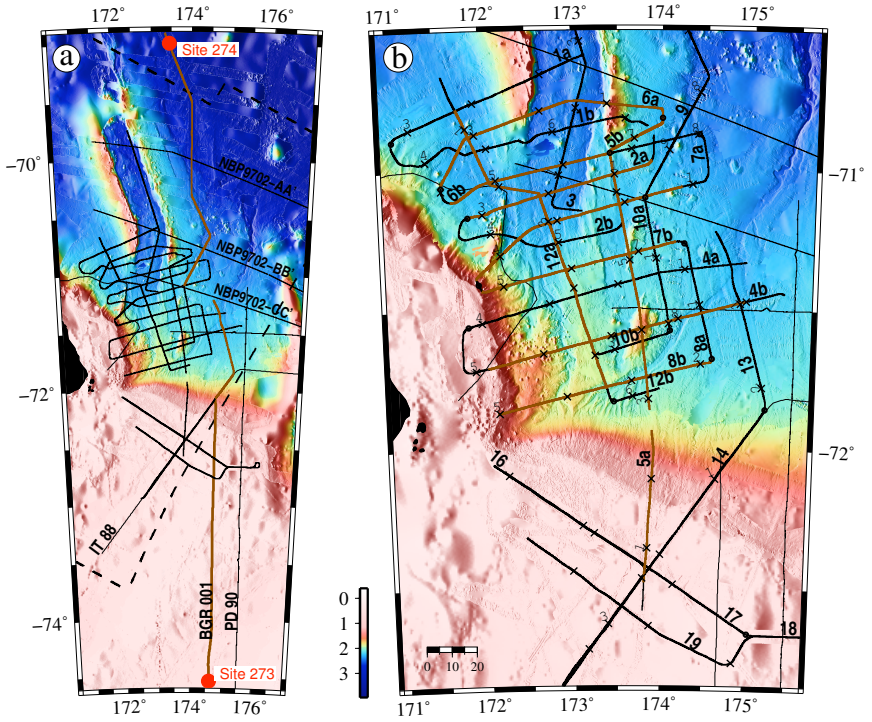

Figure 3.2: Bathymetric maps of the Adare and Northern Basins. Locations of archival seismic reflection profiles are shown with thin black lines. MCS profiles collected during NBP0701 cruise are delineated with thick black lines. Brown lines highlight the sections of the profiles shown within this manuscript. a) Locations of the tie lines from DSDP drillsites 273 and 274. The boundaries of the aeromagnetic survey conducted as part of GANOVEX IX 2005/06 (Damaske et al., 2007) are shown with dashed black lines. Note that Line 14 of NBP0701 runs along the archive Line IT 88. b) Close-up map showing NBP0701 MCS grid lines. Black crosses indicate the location of every thousandth shot point, labeled every two thousand shot points. The profiles presented in this manuscript are ordered as follow: first we show the tie lines (Figures 3.4-3.6) then the profiles are shown with respect to their latitudinal locations, starting from the north (Figure 3.7, Line 6a) and ending at the south (Figure 3.13, Line 8b). Two additional N-S profiles are presented in Figures 3.14-3.15.

We also made use of aeromagnetic data collected recently as part of GANOVEX

IX 2005/06 (see Figure 3.2a for location of survey, Damaske et al. (2007)). We have identified marine magnetic anomalies (anomalies 12o, 13o, 16y, and 18o) along a total of ~25,000 km of the GPS-navigated magnetic profiles. These picks are used here to delineate the age setting of the Adare crust and to locate and constrain post-spreading deformation. A seperate study (Granot et al., in preparation) uses this dense concentration of picks to refine the kinematics of the Adare Basin and WARS during the Eocene-Oligocene interval.

3.4 Stratigraphic Framework

The sedimentary sequence of the Ross Sea has been extensively imaged by numerous seismic reflection surveys. Brancolini et al. (1995) conducted the first comprehensive seismic stratigraphic study across the Ross Sea. They used single- and multi-channel seismic reflection data compiled by the Antarctic Offshore Acoustic Stratigraphy (ANTOSTRAT) project to identify eight acoustic sequences (RSS1 to RSS8, from old to young) separated by key reflectors that were interpreted as major unconformities (RSU1 to RSU6, from youngest to oldest, see Figure 3.3a). This division was defined in the Northern Basin along a type section that crosses the shelf-edge and enters the Adare Basin (Line IT 88, Figure 3.2a; for cross sectional view please see Figure 4 in Brancolini et al., 1995). The ANTOSTRAT sequence was correlated by Brancolini et al. (1995) to the DSDP Leg 28 Ross Sea holes (270-273) and drillsites MSSTS-1 and CIROS-1 (Figure 3.1).

Further efforts in the last decade have been focused on the seismic sequence within the VLB that was correlated with more recent drillsites (CRP and ANDRILL sites; e.g., Davey et al. (2000); Fielding et al. (2008); Johnston et al. (2008)). Bart and Anderson (2000) described in detail the late Neogene NB stratigraphy based on a single-channel seismic reflection survey. Recent studies have shown that the correlation of events across basement highs made between the various Ross Sea depocenters is problematic, especially for the old parts of the sequence (e.g., correlation of RSU6 between VLB and NB, Davey et al. (2000)). Furthermore, the oldest seismic sequence that was directly sampled in the NB area

(DSDP Site 273) is the early Miocene RSS4, making the age of the oldest parts of the sequence uncertain (Figure 3.3b).

The stratigraphy of the Adare Basin has thus far been studied using a sparse set of MCS seismic lines. Brancolini et al. (1995) traced their stratigraphic facies from the NB down the continental slope and into the Adare Basin along a single MCS line (Line IT 88, Figure 3.2a). Three east-west MCS lines collected during the NBP9702 cruise were used by Keller (2004) and subsequent studies (Muller et al., 2005; Whittaker and Muller, 2006) to trace the sedimentary units across the Adare Trough. These studies used the sequence framework as defined at DSDP Site 274, located north of the Adare Basin (Hayes et al. (1975b), Figure 3.3b). Keller (2004) and the later workers correlated horizons across prominent volcanic features and large-offset normal faults that led, in places, to ambiguous results. Moreover, the temporal resolution of these interpretations is highly dependent on the depositional history at DSDP Site 274 where a thin sedimentary sequence contains a major unconformity between lithological units 3 and 4 of Hayes et al. (1975b) and seismic units SU2 and SU3 of Keller (2004) (Figure 3.3b). This unconformity has eliminated most of the Oligocene and early Miocene strata. The present study draws on these previous studies and uses the newly acquired dataset, together with the archival seismic digital data, to tie the seismic framework as defined by Brancolini et al. (1995) into and across the Adare Basin.

Our correlation approach benefits from the relatively simple and continuous seismic characteristics that prevail from DSDP Site 273 toward the Adare Basin above RSU4a (e.g., Figures 3.4 and 3.5). The newly acquired seismic lines that cross the shallow Ross Sea shelf area allow us to confidently interpret horizons as primary arrivals down to 2.2-2.3 seconds two-way travel time (Figures 3.4 and 3.5). This depth typically encompasses the upper four unconformities (RSU1 to RSU4). We could not see basement in the shelf region, so it is not identified on any of the NBP0701 shelf lines. We correlated the deeper parts (deeper than RSU4) of the sequence into the Adare Basin following the correlation made by Brancolini et al. (1995) as defined along their type section (Line IT 88, note that our Line 14 follows the same exact track, Figure 3.2). As discussed later in the text, using basic

seismic relationships (e.g., onlap and disappearance of seismic units on known age basement) we were able to confirm some of the assigned ages of Brancolini et al. (1995).

To avoid unnecessary difficulties in our correlation, we do not correlate the ANTOSTRAT units across the entire NB but limit our interpretation to the area north of DSDP Site 273, where tie lines are available to link the stratigraphy into the Adare Basin (Figure 3.2a). A complementary tie line from DSDP Site 274 to the Adare Basin (Line 9, Figure 3.6) provides further constraints to the correlation presented here. Our correlation contributes to the on-going effort to create an updated regional seismic correlation across the Ross Sea and outer shelf area (ROSSMAP project, Davey and Sauli (2007)).

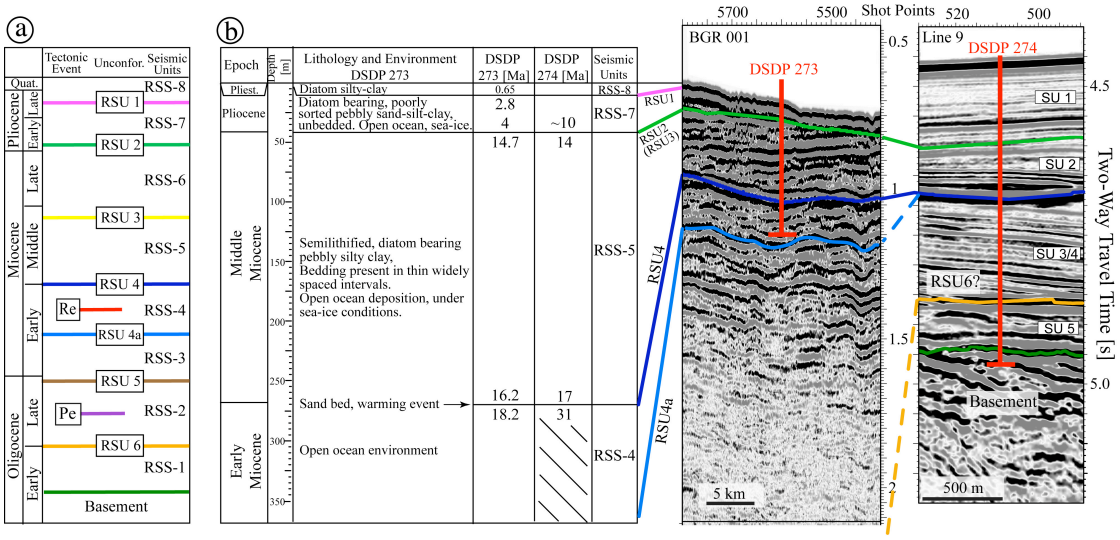

Figure 3.3: Seismic stratigraphic framework. a) General stratigraphic framework as defined by ANTOSTRAT (Brancolini et al., 1995) where the Ross Sea seismic sequences (RSS1-8) are divided by the Ross Sea unconformities (RSU6-1). The onset of the two extensional events described here are marked by Pe ("Purple event") and Re ("Red event"). b) Correlation of DSDP Site 273 stratigraphic column with DSDP Site 274 and the ANTOSTRAT sequences. The seismic units (SU1-5) that were used in previous stratigraphic studies of the Adare Basin (e.g., Keller, 2004) are shown within the section of Line 9. Description of the lithologies found within Site 273 follows Hayes et al. (1975a). Ages above and below the unconformities for both DSDP sites are from Savage and Ciesielski (1983) and Hayes et al. (1975b).

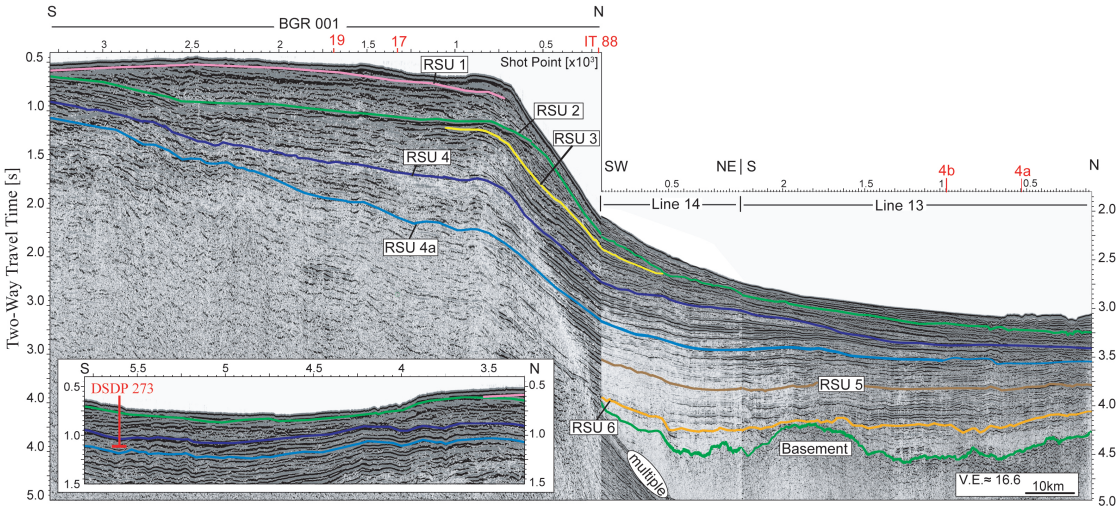

Figure 3.4: A mosaic tie line to DSDP Site 273 (BGR 001, Line 14, and Line 13 from south to north). Inset shows the southern-most part of BGR 001. The resolvable depth in the imaged shelf extends down to ~2.2 seconds and therefore we interpret only unconformities above RSU4a. RSU5 and RSU6 were traced (and re-checked) across the shelf using IT 88 profile following Brancolini et al. (1995) and correlated into the Adare Basin from the crossing point. As for all of the seismic profiles shown in this manuscript, interpreted ANTOSTRAT seismic unconformities overlay the time migrated, exponentially gained seismic profiles. Intersections with other seismic profiles and drillsites are labeled with red. Vertical exaggeration (V.E.) are based on mean seismic velocity of 1800 m/s.

3.4.1 Seismic Sequences in the Northern and Adare Basins

The studied sedimentary sequence was deposited in diverse and evolving environments causing a pronounced variability in the seismic characteristics both spatially and temporally. These characteristics vary from the relatively simple, horizontally layered sequence within the shelf area (i.e., NB), to the outer slope where typically the seismic units display wedge-like prograding-slope strata (Figures 3.4 and 3.5). Pronounced variability is found within the Adare Basin where an early Miocene tectonically-controlled topography (discussed later in the text) modulated the depositional pattern and resulted in three major domains; west, east, and center. "Center" is defined as inside the Adare Trough and along the locus of deformation to the south-southwest of the trough. The lithologies found in DSDP Leg 28 drillholes and the seismic patterns shown in the MCS data suggest

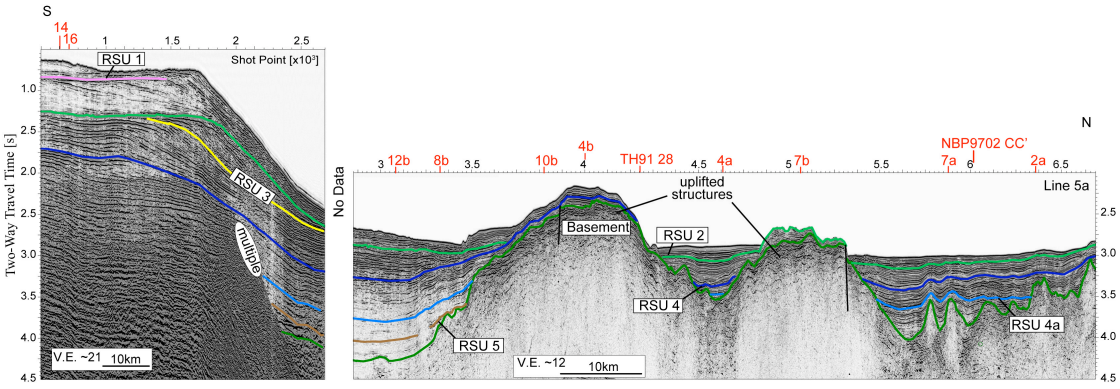

Figure 3.5: Line 5a running across the Northern Basin, shelf-edge, and the Adare Basin. Prograding clinoforms are notable above RSU3 across the outer shelf. The sedimentary sequence in the Adare Basin (SPs 3000-6500) onlaps onto the two uplifted structures indicating seafloor spreading-related formation.

that the entire sequence was transported and deposited within the Adare Basin through a combination of down-slope gravity currents and deep water bottom currents resulting in turbidites and contourite drift deposits, respectively.

Several pieces of evidence suggest that the majority of the filling sequence was transported into the basin, throughout the Neogene, from the south (i.e., NB); propagating and continuous reflectors found down slope from the NB (Figures 3.4 and 3.5), the onlapping of most of the strata onto the western shelf-edge (i.e., east of Cape Adare, Figures 3.10-3.13), and the spatial distribution of sediment thicknesses within and near the basin show a clear pattern of transport from the south (Figure 3.17). This property implies that the sequence in the Adare Basin is sensitive to the tectonic and climatic events that shaped the north-western Ross Sea.

The topography of the Adare Basin crust, prior to the post-spreading tectonic deformational events, could be characterized by a relatively low relief (up to 0.3 second two-way travel time, Figure 3.4). In contrast, two major uplifted crustal structures located along the youngest oceanic crust (Figure 3.2 and Figure 3.5 SPs 4000 and 5000) confined the transported sediments to the western and eastern sides of the basin (Figure 3.17).

In the following section we present a summary of the seismic sequence as

defined by Brancolini et al. (1995). We expand their description to the Adare Basin as we make use of their seismic framework to constrain the timing of the tectonic events in the Adare Basin (Figure 3.3a). Using four across-shelf (N-S) profiles and numerous across-basin (E-W) profiles (Figure 3.2) we are able to independently confirm their interpretation down to RSU4 at crossing points within both the Northern and the Adare Basins. The age of RSU6 was verified independently using its onlapping position on oceanic crust of known age. The relationship between RSU2 and volcanism of known age constrains the maximum age of the unconformity. We are least confident of the age of RSU5, because no drillsite is available and we were unable to find an independent age constraint.

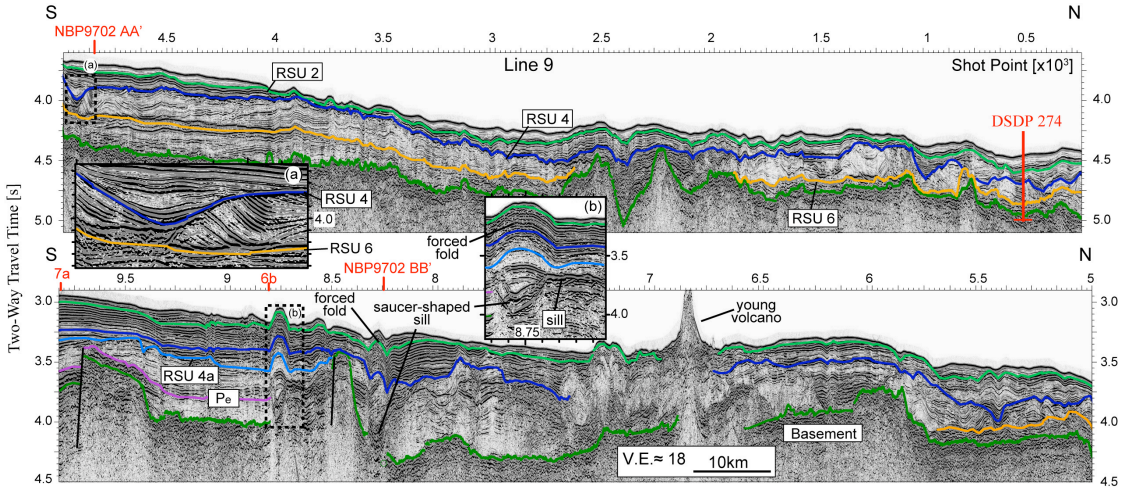

Figure 3.6: Tie line (Line 9) to DSDP Site 274, running east of the Adare Trough. RSU6 is truncated onto basement toward the Adare Trough (SP 5700). Igneous activity near SP 6800, together with complex sedimentary structures, prevent us from interpreting RSU4 at that location. Inset (a) is a close-up of RSU4 located above a block that underwent soft deformation (e.g., slumping). Inset (b) is a close-up of a saucer-shaped sill and its resultant forced fold. The entire overlying sequence is folded.

Seismic Sequence 1: Basement to RSU6

Seismic Sequence RSS1 onlaps the acoustic basement and is separated from RSS2 by a prominent unconformity (RSU6) that can be traced continuously from the NB, down the continental slope, and within the southern and westernmost parts

of the Adare Basin (Figure 3.7 and Figure 4 of Brancolini et al., 1995). Basement is characterized by strong low frequency reflectors that strongly attenuate seismic energy (for example see Figures 3.6 and 3.7, SPs 100-900). Identification of the basement-sediment contact was mostly straightforward. We did not attempt to interpret the contact in places of volcanic activity (e.g., Figure 3.9, SP 2650), or in places with thick sedimentary sequences where the signal was severely attenuated (e.g., Figure 3.8, SPs 6050-6250). Sub-parallel reflectors characterize unit RSS1 and in places it is tilted by normal faults (e.g., Figure 3.8, SPs 4900-5100).

RSU6 has never been directly sampled within the NB, and consequently its age was speculated by Brancolini et al. (1995) to be of middle Eocene to early Oligocene. However, drilling in the southwest of VLB demonstrated that the RSU6 age is ~17 Ma in the VLB area and, therefore, the miscorrelation of this unconformity between the basins is now widely accepted (Davey et al., 2000). RSU6 is found across most of the southern parts of the Adare Basin, except the youngest parts, where the unconformity onlaps the ~28 Ma oceanic crust (Figures 3.12; ages are estimated using interpolation between magnetic anomaly picks, following the geomagnetic time scale of Cande and Kent (1995), see Figure 3.18). This suggests that the age of RSU6 as defined in the NB is near 28 Ma (early Oligocene) and therefore confirms the age assigned by Brancolini et al. (1995) and the miscorrelation of RSU6 between the NB and VLB.

The upper boundary of the lowermost seismic unit (SU5) of DSDP Site 274 (Figure 3.3b, and Figure 3.6, SPs 300-5700) corresponds to a prominent unconformity with chert below and silty clay-rich layers above (Hayes et al., 1975b). No biostratigraphic markers are available for this part of the drillhole to constrain its age. Yet, the drillsite is located on crust of a known age (near anomaly 13o, ~33.5 Ma, Cande and Kent (1995)) and the oldest, although uncertain, known sediment age (~31 Ma, Hayes and Frakes (1975)) is located above this unconformity suggesting that the unconformity is of early Oligocene age. This age is broadly consistent with the age of RSU6 as defined at the NB and therefore we speculate that the unconformity that overlies SU5 at Site 274 corresponds with RSU6. This assignment has no effect on our overall correlation as this unconformity onlaps basement

and disappears south of the drillsite within the tie line (Line 9), before it is traced outward to other profiles (see Figure 3.6, SP 5700).

The lack of evidence for prominent subglacial erosion in the NB indicates that RSS1 was deposited under a temperate climate with rivers and wet-based mountain glaciers (Brancolini et al., 1995).

Seismic Sequence 2: RSU6 to RSU5

Seismic Sequence RSS2 tends to show sub-horizontal and continuous reflectors over the Northern and Adare Basins (e.g., Figure 3.4). In places where RSS1 is missing, this sequence onlaps the basement (Figure 3.5). A major faulting event took place in the Adare Basin during the deposition of RSS2 (the onset of which is marked by the purple unconformity hereafter termed the Purple event (Pe), Figure 3.3a and Figures 3.7-3.13). We define this horizon to mark the onset of faulting, below which the seismic reflectors are parallel, having uniform thickness. The Pe, which is overlain by divergent and/or onlapping reflectors (Figure 3.7c), is a time-horizon that helps us correlate the top of RSS2 (RSU5) across faults and seismic discontinuities. We interpreted this horizon only in places where we observed this stratigraphic pattern and did not trace the event outward. The upper part of the sequence onlaps onto the Purple event without an appearance of any syn-faulting divergent reflectors (e.g., Figure 3.11, SPs 5100 and 6100-6400), suggesting that this tectonic event produced major seafloor relief over a relatively short time interval. A major unconformity confined to the westernmost side of the Adare Basin is found within RSS2 (black unconformity in Figure 3.11a, and Figures 3.9-3.14). This unconformity result from reorientation of current activity. The nature of the purple and black unconformities will be discussed further later in the text.

RSS2 has not been directly sampled in the Northern and Central Basins area and was estimated to have occurred between 30 and 22 Ma (Brancolini et al., 1995). This time interval is missing from DSDP Site 274 and therefore, this unit is probably missing northeast of the Adare Trough, as confirmed in our tie line (Figure 3.6). De Santis et al. (1995) suggested that RSS2 was deposited in an open marine environment with humid and temperate climate conditions. Localized and

near-shore grounding events (Brancolini et al., 1995) suggest that glaciers were probably present in the TAM and maybe in other land areas.

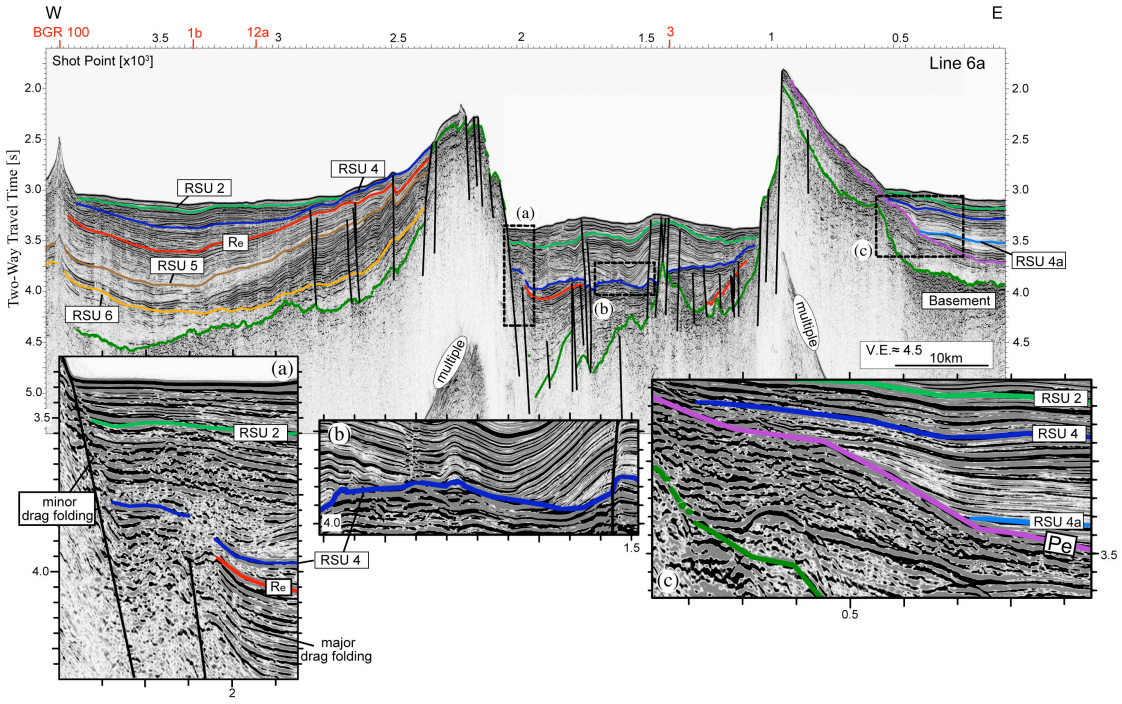

Figure 3.7: Line 6a, the northernmost profile across the Adare Trough illustrating the asymmetric structure of the two flanks of the trough. Inset (a) is a close-up of the buried section of the main normal faults that border the western Adare Trough flank. Early Miocene faulting is most evident by drag-folded strata below the red unconformity. The overlying strata shows relatively minor drag folding. Inset (b) is a close-up of RSU4 located at the center of the extended zone. Below the unconformity are strong reflectors with chaotic to parallel reflector patterns suggesting re-worked sedimentation. Above RSU4 are levee-channel complexes suggesting gravity-contolled deposition. Inset (c) is a close-up of the base of the eastern flank. The purple unconformity marks the uplift of the flank with younger strata onlapping on top.

Seismic Sequence 3: RSU5 to RSU4a

In the NB and the Adare Basin, Seismic Sequence 3 (RSS3) downlaps on RSS2 and is generally conformable with the overlying and underlying units (Figures 3.4, 3.12 and 3.13). Based on ages for DSDP Site 273, Savage and Ciesielski (1983) have estimated the ages of RSS3 to range between 21 and 18.5 Ma. The

low reflectivity and the uniform stratification of the sequence with buried channels offshore the VLB (Brancolini et al., 1995), suggest that the sequence was deposited in an open marine environment with advance and retreat of subpolar glaciers into the continental shelf.

Seismic Sequence 4: RSU4a to RSU4

This seismic unit is found throughout most of the Northern and Adare Basins. It contains sub-parallel, continuous, and well-defined reflectors (Figures 3.4, 3.11-3.13). A major rifting event took place during the deposition of RSS3. This event is characterized by normal faulting that initiated, in places, differential block tilting and accompanying subsidence (Figures 3.8-3.11). This extensional event (onset of which is marked by red line hereafter termed the Red event (Re)) is typically associated with thick syn-rifting depositional sequence that is underlain by a sequence of strong reflectors (Figure 3.8, SPs 5300-5400 and Figure 3.9, SPs 1500-2500). These strong reflectors exhibit, in places, chaotic structure that may suggest re-worked sedimentation (e.g., Figure 3.9, SPs 1900-2300).

The top-most part of the sequence (RSU4) is defined by a pronounced change from these strong reflectors to a less- or non-reflective sequence (e.g., Figure 3.7a). In places, RSU4 is marked by an angular unconformity (e.g., Figure 3.7a and Figure 3.8, SP 5480). Along the eastern side of the Adare Basin, significant relief (up to 0.3 second two-way travel time) of RSU4 is associated with non-faulted but internally deformed strata (e.g., Figure 3.9a). These structures might have been resulted from soft sediment deformation that formed as a result of seismic activity associated with the red extensional event. Within and south of the Adare Trough, a change in the acoustic character across RSU4 together with its consistent appearance over tens of kilometers suggest that RSU4 is associated with a regional change in the sedimentation processes that might have resulted from a tectonically-induced change in seafloor topography (e.g., developed depression) or to a regionally climatic event. The nature of the Red event will be discussed further later in the text.

RSS4 has been sampled at DSDP Sites 273, 272 and 274. In Site 273 it

contains semi-lithified, diatom-bearing pebbly silty clay (Figure 3.3b). The top (RSU4) of the unit in Site 273 is made from a sand bed, which resulted, probably, from seafloor currents (Brancolini et al., 1995). The sequence was probably deposited under an open-water environment that was followed by a change in ocean circulation and possibly the initiation of sea ice (Savage and Ciesielski, 1983). Brancolini et al. (1995) assigned tentative ages to RSS4 between 18.34 and 16.5 Ma. Based on the biostratigraphic ages across the unconformity found at core 19, DSDP Site 274 (17 to 30 Ma, Hayes et al. (1975b)), we assigned the RSU4 unconformity to the depth of 180.5 m at Site 274 (4.7 second two-way travel time in Figures 3.3b and 3.6).

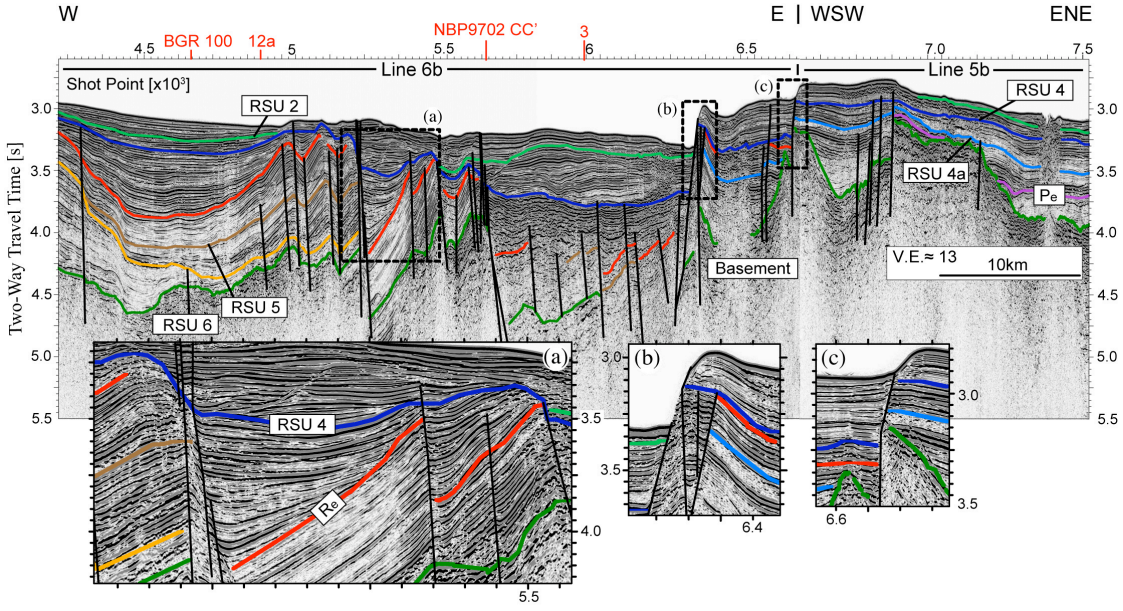

Figure 3.8: Mosaic of Lines 6b and 5b located immediately south of the Adare Trough. Inset (a) is a detail of a block-faulted area, located south of the terminated west flank of the Adare Trough. Note the onset of the early Miocene faulting event (Red event, Re), and the thick continuous syn-faulting package that is overlain by RSU4. Extensional motion ceased subsequent to RSU4. Inset (b) is a close-up of growth normal fault that bounds the early Miocene depression from the east. Red unconformity marks the onset of faulting, but developed seafloor scarp, younger drag folding, tilted and thickening of strata away from the fault suggest that faulting was, and still is, active continuously since the early Miocene. Note the large seafloor scarp (260 meters). Inset (c) is a detail of a steep growth (and active) normal fault creating a seafloor scarp.

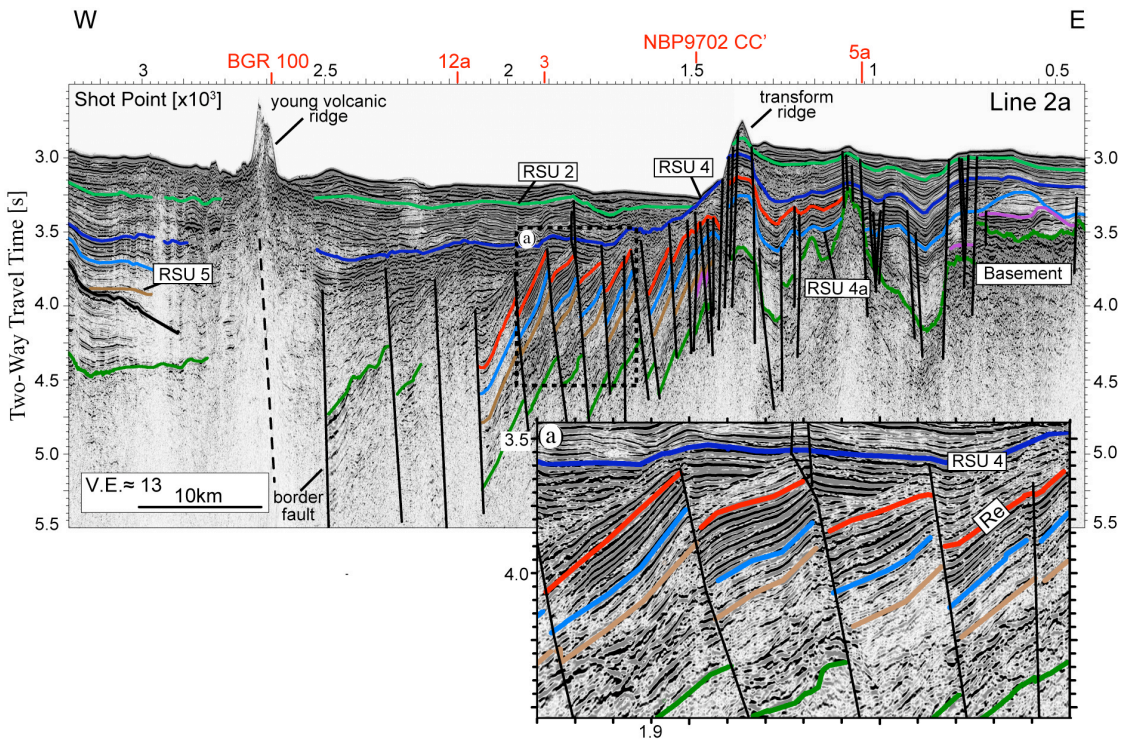

Figure 3.9: Line 2a crossing the morphological trough south of the Adare Trough. The trough is bounded on the east by a transform ridge and by an active volcanic ridge on the west. Inset (a) is a close-up of tilted blocks bounded by easterly dipping normal faults. Faulting initiated at the Red event, prior to the middle Miocene RSU4 unconformity. Note the pronounced change in seismic characteristics across RSU4.

Seismic Sequence 5: RSU4 to RSU3/RSU2?

RSS5 is mostly non-reflective, with irregular and cross-cutting reflections in the Central and Northern Basins (Brancolini et al., 1995). This sequence has been sampled by DSDP Site 273 where it contains semi-lithified, pebbly silty clay (Figure 3.3, Hayes et al. (1975a)). It was also sampled at DSDP Site 274 where it contains silty clay with scattered pebbles of highly varied lithologies that occur along the NVL (Hayes et al., 1975b). Grains coarser than silt size are not observed above the middle of the sequence at Site 274, suggesting that the morphological Adare Trough may have developed sufficiently in the middle Miocene to be an effective trap for the gravity-controlled coarse sediments that were transported from the shelf and would have had to flow northeast across the Adare Trough to

the location of Site 274. The youngest age below RSU3 at Site 273 is 14.7 Ma (Savage and Ciesielski, 1983).

As will be discussed further later in the text, RSS6 is missing for most of the study area and RSU2 and RSU3 in the Adare Basin cannot be distinguished as separate seismic events. Within the Adare Trough, RSS5 displays a distinctive pattern of continuous parallel to sub-parallel or wedging low-amplitude reflections (Figure 3.7, SPs 1100-2000). These reflectors create channel-levee complexes (resembling the Amazon Fan-like complexes of Manley and Flood, 1988) indicating that sediment deposition was controlled by gravity currents. Downlap terminations that propagate northward along seismic Line 3 (Figure 3.15, SPs 2100 to 2700) suggest that the axes of these channels trend along the trough with a northerly direction of flow. The spatial extent of this gravity-controlled facies includes the morphological Adare Trough and the depressed region, located south-southwest of the trough (e.g., Figures 3.7-3.8, 3.15; see also dashed gray line in Figure 3.17b). The seismic properties of these deposits are highly variable over even a few kilometers. Generally, this unit is cut by near-vertical normal growth faults that typically display minor offsets and therefore resulted in a negligible extensional effect (e.g., Figures 3.7b and 3.8a). To conclude, RSS5 highlights the end of the pronounced extensional activity in the Adare Basin.

Seismic Sequence 6: RSU3 to RSU2

In the western Ross Sea RSS6 is observed only across the NB shelf break and is missing entirely from the rest of the NB (Figure 3.5, SPs 1200 to 2600 and Brancolini et al. (1995)). The steep slopes and rapid downlap of RSS6 near the base of the slope north of the NB suggest that the sequence was deposited during a sea-level low stand. The age of this sequence is mostly speculative as it is missing from the shelf DSDP sites. Brancolini et al. (1995) have tentatively assigned RSS6 ages between 14 to 4 Ma. The last 10 million year of strata sampled at DSDP Site 274 (Figure 3.3b, Savage and Ciesielski (1983)) show no biostratigraphic hiatus, suggesting that either the ages of RSS6 in the Adare Basin are 14 to 10 Ma or that the unit is not resolvable in the deep sea. We could not confidently identify RSS6

in the Adare Basin.

Seismic Sequence 7: RSU2 to RSU1

RSS7 is found across the entire study area and forms the uppermost observable strata. Typically, it exhibits uniformly stratified seismic reflectors (e.g., Figures 3.8-3.9), although in places multiple internal unconformities are observed (e.g., Figure 3.13a). RSS7 was sampled by DSDP Sites 273 and 274. In Site 273 it includes glacial-marine strata (sea-ice conditions) dated between 4 and 2.8 Ma (Savage and Ciesielski, 1983). Similar strata are found in Site 274, although no equivalent bounding unconformities were detected (Hayes et al., 1975b). In the western Ross Sea, the base of the sequence (RSU2) is marked by a sharp change in the erosional pattern, having wide and deep erosional troughs, similar to the morphology of the present-day seafloor. This observation provides the first clear evidence for full polar and ice sheet conditions (Brancolini et al., 1995).

In the Adare Basin, RSS7 is frequently penetrated by magmatic material (Figure 3.10, SPs 2600 and 4200). Several volcanic localities sampled during the NBP0701 cruise have been dated between 0.2 to 4.9 Ma (Panter and Castillo, 2008). In places, RSU2 onlaps on similar volcanic features (e.g., Figure 3.9, SPs 2600-2750, and Figure 3.13a).

Seismic Sequence 8: RSU1 to seafloor

RSS8 is an isolated and typically thin sequence. In the NB a strong basal reflector that corresponds with RSU1 defines its base (Figures 3.4 and 3.5). At DSDP Site 273, the sequence consists of 0.8 m of marine sediments with ages ranging from 0.65 Ma to present day (Savage and Ciesielski, 1983). No distinct appearance is found for RSS8 within the Adare Basin, suggesting that the unit thins below seismic resolution north of the shelf. DSDP Site 274 shows no indication of an RSU1 unconformity (Hayes et al., 1975b), providing further evidence for the thinning and possible absence of RSS8 in the Adare Basin.

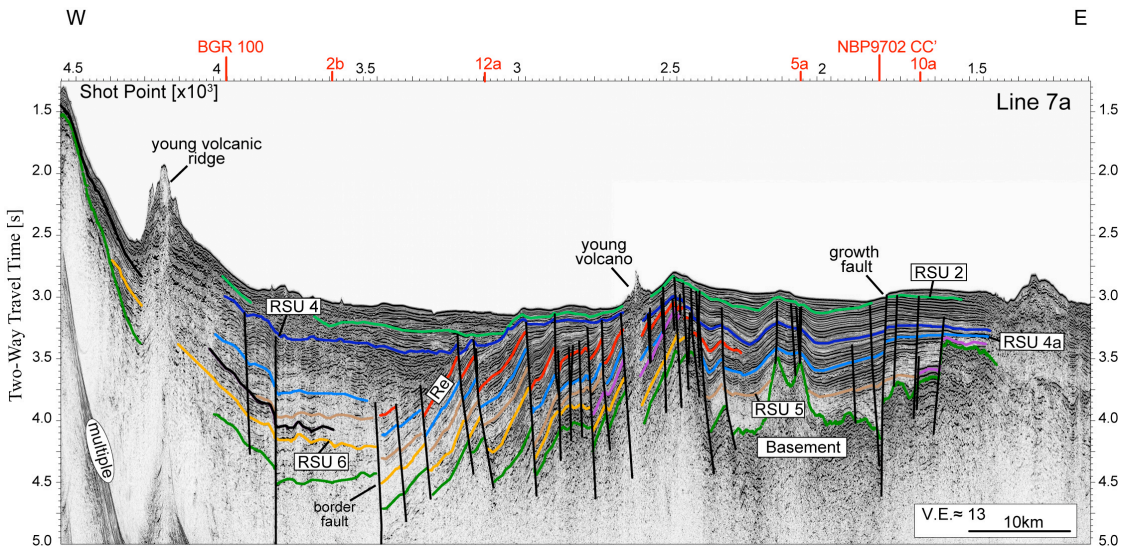

Figure 3.10: Line 7a across the morphological trough southwest of the Adare Trough. Note the increasing subsidence toward the border fault (SP 3500). Recent volcanism and minor active growth faulting are indicated.

3.5 Discussion

We will focus our discussion on the complex tectonic history of the Adare Basin in the temporal context of the following events: the early phase of post-spreading deformation (Purple event), the major early Miocene rifting event (Red event), and the recent volcanic activity and vertical faulting. We will then evaluate the results in the broad regional context.

3.5.1 Late Oligocene Deformational Event [Purple Event]

The earliest evidence for onset of brittle deformation (Purple event) is shown by tilting of deep strata along a few prominent normal faults that strike NNW-SSE, parallel to the Adare spreading axis (e.g., Figures 3.11b, and 3.16), and are located within the center and eastern side of the Adare Basin (see dashed purple line in Figure 3.17c). The faults dip toward the paleo-spreading axis and therefore seem to reactivate pre-existing structures. The typical vertical component of slip across the faults ranges between 0.2 and 0.5 second two-way travel time (Figure 3.11, SPs 6400, 7050, and 7350). The onset of faulting is found between RSU6

(~28 Ma) and RSU5 (~21 Ma, e.g., Figure 3.11, SPs 5300 and 6100-6400), and we therefore assign it to be of late Oligocene age, at ~24 Ma. This speculative age coincides with a major unconformity found in the CRP drillcore (Wilson et al., 2000).

Tilted strata also overlie the eastern flank of the Adare Trough (Figure 3.7c). We could not identify similar deep tilted strata near the western flank of the trough. In fact, with the new reflection dataset, we have correlated the seismic sequence across the Adare Trough is bounding faults by using the E-W profiles located south of the trough (Figure 3.2b, and Figures 3.8-3.9) and then using the N-S profiles (Figures 3.14-3.15). In this way we have traced the sequence back into and west of the trough. The resulting correlation indicates that the major onset of faulting of the western Adare Trough flank is significantly younger than the purple unconformity found along the eastern flank and could not have taken place at the same time. This suggests that the Adare Trough formed in an asymmetric fashion, where the eastern flank (southern-part) of the trough developed shortly after spreading ceased (i.e., late Oligocene). We note however that the purple unconformity is found south of the western flank (Figure 3.11b). There, deep tilted strata juxtaposed against east-dipping normal fault. This may indicates that fault re-activation during the Purple event may have been symmetric but cannot be detected along the western flank of the Adare Trough. The north part of the eastern flank is deeper than the southern edge (Figure 3.2). Although based on a limited amount of data collected across the northern part of the trough, we believe that the northeastern flank represents the original shape of the trough, immediately after seafloor spreading ceased, and did not undergo significant uplift during the Purple event. Lack of sufficient MCS data led previous studies (Muller et al., 2005; Whittaker and Muller, 2006) to conclude, solely based on gravity and flexural modeling, that the Adare Trough formed in a single event that took place shortly after spreading stopped. The new seismic data reveal that the formation of the trough was a rather complex process, both spatially and temporally.

The asymmetric uplift of the trough may be related to the original asymmetry in seafloor spreading. This may have produced contrasting mechanical crustal

properties across the trough, causing a post-spreading asymmetric response to induced stresses. The sum of the calculated heaves (horizontal separation across a fault) along the reactivated faults indicates that the Purple event resulted in a total of 1-2 km of extension over a distance of ~140 km, across the center of the Adare Basin.

A striking stratal relationship is found along the western continental slope (e.g., Figures 3.11a and 3.12). There, an angular unconformity separates the deepest strata that pinches out eastward against an overriding younger strata that onlaps onto the unconformity. This event could have resulted from an important reorientation of bottom current flows, where an oblique SW to NE flow was replaced by a S to N flow. We could not confirm whether this unconformity correlates with the purple unconformity, although we note that both unconformities are located in a similar position within the sedimentary package.

The underlying mechanism that generated the Purple event, whether it is linked to motion within the WARS or formed independently, is of great interest. Similarity of seismic properties above and below the purple unconformity (e.g., Figure 3.11) suggest that the event was not associated with a pronounced change in the depositional environment. The throw along the faults diminishes southward without a resolvable throw found close to the southern continental slope (see Figure 3.13 vs. Figures 3.11-3.12). On the other hand, younger extensional motions, as we will discuss later in the text, show distinct linkage to faulting outside the basin and resulted in remarkably different extensional structures. We conclude that the Purple event was isolated from the late Oligocene kinematics within the WARS.

A number of independent observations provide important constraints on the tectonic process that resulted in the Purple event. The apparently abrupt cessation of seafloor spreading, without a slowdown in spreading rate toward the end (Cande et al., 2000), might have left residual magma and heat in the Adare Basin. The temporal proximity of the Purple event to the end of seafloor spreading might suggests that the excess magma and heat could have led to reactivation of faults. Local mantle convection has been suggested in the Gulf of Suez as a key component in shaping rift systems (Steckler, 1985) and an analogous process may

have been partly responsible for the creation of the Purple event.

3.5.2 Early Miocene Rifting [Red Event]

Evidence for the main phase of Neogene rifting (Red event) is found buried south and southwest of the Adare Trough. This event, whose onset is marked by the red unconformity, initiated of a series of similarly tilted fault blocks bounded by normal faults (Figures 3.7-3.11). The dips of the divergent reflectors above the red unconformity (Figure 3.8a) display a continuous evolution, from dips subparallel to the red horizon (i.e., the bottom reflector) to the sub-horizontal reflectors at the top of this package. These syn-faulting growth strata indicate that faulting was continuous during this tectonic interval. In general, normal faults are steep (>70°, using seismic velocity of 1800 m/s, Figure 3.16a) but show large variability in dip. Typically, these faults dip eastward creating westward-tilting in half graben (e.g., Figure 3.9b, and Figure 3.10, SPs 2500-3500). The tilt blocks form an en-echelon pattern with an overall trend of NE-SW, from just south of the Adare Trough to the Cape Adare and Hallett volcanic province (Figures 3.16-3.18). The southwestern border of these structures reaches the slope of the western continental shelf.

The onset of the Red event is stratigraphically located between unconformities RSU4a (~18.5 Ma) and RSU4 (~16.5 Ma) (e.g., Figure 3.8, SPs 5200-5500, and Figure 3.9, SPs 1500-2000). We therefore speculate that deformation began at ~17 Ma (early Miocene). Growth strata are buried under RSU4 suggesting that all of the extensional activity ended prior to 18 Ma. We note that the lack of drillsites within the Adare Basin, and the possibility of time transgressive unconformities, lead to some age uncertainties. Yet, since the ages above RSU4 at both DSDP 273 and 274 Sites are similar (Figure 3.3b), the Red event cannot be significantly younger than 17 Ma.

Evidence for faulting and uplift is found along the western flank of the Adare Trough (e.g., Figure 3.7, SPs 2400-3000). Strata below the red unconformity are also tilted within the trough, adjacent to the westerly bounding faults (Figure 3.7a), suggesting that the western flank of the Adare Trough uplifted during the early Miocene tectonic event. This uplift coincided with prominent subsidence on

its west flank (Figure 3.7, SPs 3000-3800, and Figure 3.17). Vertical offset of RSU4 (~0.5 second two-way travel time) across the eastern flank suggests that up to ~450 m of uplift took place along the flank. Uplift of the flanks of the Adare Trough is consistent with the change in lithology within DSDP Site 274, where particles coarser than silt size are absent above the middle Miocene sequence (Hayes et al., 1975b), suggesting that the trough became an effective trap for sediments. This marks the last prominent uplift in the region of the trough. Younger motion along the bounding faults produced minor drag folding of the strat above the red unconformity (Figure 3.7a).

The tilted blocks south of the Adare Trough formed a narrow depression where sediments continued to be accommodated, but nevertheless resulted in the NE-SW trend of the present day morphological trough (Figure 3.16). These blocks are the cause of the disappearance of the Adare Trough to the south (Figure 3.18). They are bounded on the west by border faults (Figures 3.9-3.11) along which the throw is the greatest. This structural asymmetry led to basins deepening westward, with thicker basin fill sequences toward the west (i.e., towards the border faults, see Figure 3.17a). The spatial correlation between the faulting of the Red event and the filling sediment thickness (Figures 3.17a,b) suggests that rifting dominated the pattern of sedimentation.

The spatial distribution of normal faults indicates a close association between the Adare rifting and the tectonics of the WARS, at least for its northern Victoria Land sector. The early Miocene rifting event marks a westward shift and localization of deformation within the Adare Basin, concentrating extension within a narrow (20 to 30 km wide) deformed zone (i.e., necking) that cross cuts the basin (Figures 3.17c and 3.18). The landward trend of the rift suggests that deformation continued beyond the Adare Basin only to the southwest, probably on, or very close to, Cape Adare. Indeed, recent land-based structural mapping of Faccenna et al. (2008) showed that a set of NE-SW-striking eastward-dipping normal faults were active during the Miocene in the northernmost block of Victoria Land (Admiralty Mountains block, Figure 3.1). This set of faults could have been kinematically linked with the deformation accommodated within the Adare Basin,

transferring the motion southward, possibly into the Terror Rift. This structural setting hosted the younger volcanic activity (discussed further in the next section; see also Ferraccioli et al. (2008)). The lack of a southward continuation of faulting within the Adare Basin implies that no deformation was accommodated within the center part of the NB during the Neogene, as supported by the study of Brancolini et al. (1995).

The structural segments that created the en-echelon fault pattern of the Red event are separated by small transfer zones (ridge and accommodation zones, Figure 3.16), along which there is up to 5 km of horizontal separation (Figure 3.16). A sparse set of seismic reflection data were used by Storti et al. (2007) to interpret flower structures in the Adare Basin suggesting that a major strike-slip fault crosscut the basin along a NW-SE trend (termed the Cape Adare Fault by Salvini et al. (1997)). We find no seismic nor bathymetric evidence for a through going strike-slip fault, although minor strike-slip features might be located near the transfer zones. The marked continuity of seismic reflectors and seismic properties along our N-S profiles (Figures 3.4-3.6) provides further support for the lack of strike-slip motion in the Adare Basin and on the continental slope. This observation agrees well with the continuity of the magnetic lineations that straddle the Adare Basin and NB without disruption (Figure 3.1 and Damaske et al. (2007)). We conclude that no major strike-slip faulting has occurred in the Adare Basin since seafloor spreading started (~43 Ma).

Two dominant trends of normal faults are observed during the Red event. NNW-SSE (350°-170°, Figure 3.16) faults are located along the Adare Trough while N-S striking faults are found in the central part of the basin (Figure 3.16). The early Miocene direction of extension was therefore between ENE-WSW (80°-260°) and E-W presumably leading to, on some of these faults, minor strike-slip motion. The amount of extension that was accommodated during the Red event was calculated using the reflection data and verified independently by seafloor magnetic anomalies. An approximation of the extension along each of the seismic profiles that crosscut the extended zone was calculated using the sum of the heaves and, where tilted blocks are developed, using the apparent dips of the bounding

faults and the tilted beds (using mean velocities of 1800 m/s, Twiss and Moores (1992)). Our calculation along seven profiles shows that the amount of extension in the early Miocene was between 3 and 5 km.

The Eocene seafloor magnetic anomalies provide an independent constraint on the total amount of post-spreading extension of the Adare Basin (i.e., the combined effect of the Purple and Red events). The West Antarctic plate isochrons (i.e., east side of the basin), located outside the deformed zone, serve as a reference for the pre-Neogene crustal setting. We have rotated back anomalies 12o and 13o using the anomaly 18o rotation pole of Davey et al. (2006), using the northern-end of the East Antarctic anomalies, located outside the deformed zone, to constrain the degree of rotation (Figure 3.16b). Each anomaly was rotated using a single rotation angle (1.26° and 2.4° for anomalies 12o and 13o, respectively). The resulting mismatches between the rotated and unrotated anomalies, along two trajectories straddling the deformed zone, confirms that the total amount of E-W extension, since the cessation of seafloor spreading, could not have been larger than ~5 km (see inset in Figure 3.16b). This result is in broad agreement with our seismic results and with the previous flexural uplift models for the Adare Trough of Muller et al. (2005). We conclude that the total amount of extension in the Adare Basin was smaller than 7 km (Purple and Red events, combined), all of which occurred prior to the middle Miocene.

3.5.3 Recent Volcanism and Vertical Faulting [Pliocene to present-day]

Prominent volcanic activity and near-vertical normal faults define the most recent tectonic activity in the Adare Basin. Based on the seismic reflection and bathymetric data, we have mapped 257 surface volcanic features (Figure 3.16a). Volcanism in the Adare Basin typically forms individual volcanic knolls (e.g., Figures 3.11, SP 6400 and Figure 3.15, SP 3900). Some of the volcanic bodies have coalesced to build a volcanic ridge oriented NE-SW, following the general trend of the early Miocene deformed zone (Figure 3.16a). Part of the volcanism follows the trend of reactivated normal faults to form NNW-SSE chains, while other volcanic

centers follow the major bounding faults of the Adare Trough (Figure 3.16a). Elsewhere, magma intruded at depth, forming sub-horizontal sills and saucer-shaped like sills that are always associated with forced folds and faults located immediately above the intrusions (e.g., Figure 3.6a).

Preliminary results from a recent geochemical study of dredged rocks from the Adare Basin (Panter and Castillo, 2007) reveal striking similarities between the lithological and isotopic signatures of the Adare volcanism and the on-land WARS volcanism. The spatial spread of submarine volcanism (Figure 3.16a) within the Adare Basin seems to points in the general direction of the Cape Adare volcanic ridge and the Hallett volcanic province. We therefore deduce that the volcanic activity within the Adare Basin is closely associated with the volcanic activity of the WARS.

The age of volcanism is constrained by both the seismic stratigraphic relationships and direct sampling of volcanic material. All of the volcanic knolls are exposed above the seafloor surface and penetrate nearly the entire stratigraphic column (i.e., no fully buried knolls are observed). In places, strata younger than RSU2 onlap onto these volcanic features (e.g., Figure 3.9 SP 2750 and Figure 3.13a) suggesting a volcanic age older than 4 Ma. The entire stratigraphic section is folded above the imaged saucer-shaped igneous sills (e.g., Figure 3.5, SP 8750), without an onlapping pattern of younger reflectors on top, suggesting that they intruded the sedimentary sequence very recently (Hansen and Cartwright, 2006). Preliminary ages (using $^{40}Ar/^{39}Ar$) of seven dredged volcanic sites, spread across large distances, range from 0.2 to ~5 Ma (Panter and Castillo, 2008), further confirming Pliocene ages for the Adare volcanism. Although older volcanic activity in the Adare Basin is possible, we regard this option as unlikely as no such buried volcanic knolls, nor older intrusions, have been detected along the ~3,200 km of MCS data. Volcanism in the Hallett volcanic province ranges from 12.4 Ma (south of Cape Adare, Nardini et al. (2003)) to 10-11 Ma for Cape Adare (Mortimer et al., 2007). The younger offshore ages indicate that the initiation of volcanism in the northern part of the WARS migrated northward, from the middle Miocene initiation at 73°S to the Pliocene initiation at 70°S.

Pliocene to present-day brittle deformation is commonly found in areas that were active during the Red event. This activity is characterized by near vertical normal faults that have, typically, minor throw (less than 0.1 seconds, e.g., Figure 3.7b), although in a few places slip reaches 0.5 seconds (e.g., Figure 3.8b and 3.8c). Pronounced seafloor scarps (50 to 350 m) accompany many of these faults (e.g., Figure 3.8b and 3.8c). Growth faulting is also common (e.g., Figure 3.8c), reactivating Neogene structures. The near-vertical orientation of these faults implies that this phase of deformation accommodated negligible extension compare with the early Neogene deformation. A detailed analysis of the Neotectonic activity in the Adare Basin will be presented elsewhere (Stock et al. in preparation).

3.5.4 Regional Synthesis

Implications for the Neogene Kinematics of the WARS

The Neogene tectonic history of the Adare Basin as documented in this study has important implications for the kinematics of the WARS. We first make use of the Eocene-Oligocene kinematic framework (i.e., location of the pole of rotation) as a starting point to evaluate the Neogene motion of the WARS, assuming the rift system continued to extend in a coherent fashion. The cessation of spreading in the Adare Basin at 26 Ma must have been associated with a sharp decrease in the WARS rate of extension, as no prominent extension is observed in the western Ross Sea basins and Adare Basin immediately after (this study and Cooper et al., 1987). Utilizing the Eocene-Oligocene East-West Antarctica pole of rotation (located near the South Pole; Davey et al. (2006)), and our 3-5 km of early Miocene extension in the Adare Basin (the portion of the motion that appears to be linked with the regional framework), we predict that the extensional motion in the VLB sector should have been minimal (2-3 km) in the same period of time. A series of well constrained studies have shown that the VLB in the late Oligocene and early Miocene was indeed characterized by thermal subsidence without significant rifting (Hall et al., 2007; Henrys et al., 2007; Fielding et al., 2008). This kinematic confirmation implies that the position of the pole of rotation of the WARS was relatively stable from the Eocene until the middle Miocene.

One of the most intriguing implications of this study is the difference in timing of extension in the Adare Basin compared to region further south. The Adare Basin did not extend in the middle Miocene, a period when the Terror Rift accommodated 10 to 15 km of extension (Henrys et al., 2007; Fielding et al., 2008). If the Eocene-Oligocene pole of rotation still prevailed, and the rift system still accommodated extension throughout its length in a coherent fashion, then 13 to 20 km of extension in the Adare Basin since the middle Miocene is expected. We regard this scenario as unreasonable and conclude that sometime in the middle Miocene (17-13 Ma) a major change in the kinematics of the WARS took place. At this moment, we cannot constrain the exact location of the middle Miocene and younger pole of rotation. Yet, near zero extension in the Adare Basin, 5 km of extension in the NVL (Admiralty Mountains block), and 10 to 15 km of extension in the Terror Rift suggest an increase of rifting southward since the middle Miocene. The apparent northward propagation in the age of volcanic activity in the late Neogene is consistent with this hypothesis (i.e., volcanism occurs first where the crust is more stretched).

A recent study has suggested that deep sub-ice troughs and basins located in the deep interior (e.g., Bentley Subglacial Trench, Figure 3.1, LeMasurier (2008)) have formed under ice-sheet conditions, implying Neogene formation. The kinematic evolution of these features is currently poorly understood, yet their Neogene formation suggests that major Neogene rifting took place along most of the WARS length, probably with a southerly increasing magnitude. Therefore, the East-West Antarctica pole of rotation may have been located somewhere north of the Adare Basin since the middle Miocene (with opposite sense of motion compared to the Eocene-Oligocene motion). Alternatively, the nature of deformation in the WARS may have changed from coherent rifting (as in the Eocene-Oligocene period) to fragmented and kinematically isolated basins. The seemingly continuous Miocene faulting along the axis of the WARS for hundreds of kilometers suggests, however, that the latter hypothesis is probably invalid. Geodetic (Donnellan and Luyendyk, 2004; Zanutta et al., 2008) and seismicity measurements (Behrendt et al., 1991) show that there is currently no significant motion across the WARS, suggesting

that our hypothesized middle Miocene shift of the pole might have been the precursor to the unification of East and West Antarctica into a coherent plate.

The uplift of the TAM has been linked to the extensional motion accommodated within the rift system by isostatic uplift of the rift flank (e.g., ten Brink et al. (1997), but see other possible models therein). Neogene evolution of the TAM is marked by contrasting denudation ages of its building blocks. Using cosmogenic isotopes, Van der Wateren et al. (1999) showed that the NVL block was uplifted in the middle Miocene (minimum age of ~11 Ma, Figure 3.1) whereas the block located west of the Terror Rift, within central Victoria Land (Figure 3.1), was uplifted in the Pliocene (minimum age of ~4 Ma). Although these contrasting ages may have resulted from different glacial histories, variations in the characteristics of the crust, and/or dextral transtension that divided the continent into confined blocks (Wilson, 1995; Salvini et al., 1997), they can also be partly explained by the two distinct rifting histories of the northernmost part of the WARS (i.e., Adare Basin) vs. the WARS central part (i.e., Terror Rift). In this scenario, early Miocene rifting in the northwestern WARS was followed by the middle Miocene uplift phase of the TAM northern block, and the middle Miocene opening of the Terror Rift was followed by the Pliocene uplift of the central TAM.

A possible interplay between the tectonics of the WARS and climate has been suggested previously (e.g., Behrendt and Cooper, 1991; Van der Wateren and Cloetingh, 1999). Crustal stretching may have promoted denudation of the TAM which in turn provided part of the boundary conditions for ice sheet growth and consequent increase in erosion rates. This then have resulted in an increase in the supply of larger clasts of sediments into the rift system. It also have created regional unconformities. Thus far, lack of drill cores within the Adare Basin precludes making any firm suggestion as to the time elapsed between the rifting phase (Red event) and the successive unconformity (RSU4), and also precludes investigating lithological changes across the unconformity and their likely relationship to climatic events.

Comparison with the regional tectonic framework

The suggested relative plate motion between the East and West Antarctic plates since the cessation of seafloor spreading has a negligible effect on the fit of the global plate circuit models (for instance, on the fit of the predicted track of the Hawaiian hot spot) and hence, for that purpose, the Antarctic plates can be treated as a single plate since chron C9. The proposed middle Miocene and younger motion within the WARS has, however, an important consequence on the predicted motion of the Alpine fault, New Zealand. Preliminary predictions of the motion along the fault, calculated using the Australia-East Antarctica-West Antarctica-Pacific plate circuit for Neogene time suggest that a decrease in the orthogonal motion across the fault would result from the extension within the WARS. The increase of extension southward during the Miocene implies that, possibly, significant motion (either extension or strike-slip, depending on the location) was accommodated in the southern parts of the rift system (e.g., within the sub-ice troughs and offshore structures of the Bellingshausen Sea (Muller et al., 2007)).

Rifting history of the WARS should be associated with changes in plate motions of the adjacent plates. Cessation of spreading in the Adare Basin and the sharp drop in the amount of rifting in the WARS at 26 Ma was accompanied by a major plate reorganization south of New Zealand; the spreading direction on the Pacific-Australia ridge rotated significantly and was eventually replaced by oblique transform motion along the Macquarie ridge complex (Sutherland, 1995; Massell et al., 2000; Keller, 2004).

Neogene seafloor spreading along the Antarctic-Pacific ridge is marked by several well constrained major changes in plate motion (Croon et al., 2008). These events occurred at 27 Ma (chrons C9o-C9y), 23 Ma (chrons C6C-C6B), and 16 Ma (chrons C5Cy-C5b) and may have been related to the cessation of spreading along the Adare spreading ridge, the late Oligocene (Purple) deformational event, and the younger, early Miocene (Red) rifting event, respectively. A continuous change in plate motion since 16 Ma along the Pacific-Antarctic ridge suggests that the demise of rifting along the WARS was a gradual rather than an abrupt phenomenon. The nicely correlated ages of changes in plate motion between the

Antarctic-Pacific ridge and the Adare Basin provides an independent confirmation for our suggested Neogene temporal framework. The relative plate motions along the Antarctic-Australia ridge (South East Indian Ridge, SEIR, Figure 3.1), and between the Pacific and Australia plates (along and near New Zealand) have been generally steady since 20 Ma (Cande and Stock, 2004b). However, a significant change in plate motion has been detected around 6-8 Ma which triggered the formation of the Macquarie Plate and which probably related to changes in the Pacific-Antarctic plate motions (Cande et al., 1995). At this point, the kinematics of the SEIR is known with insufficient resolution to make a comparison with the WARS tectonics.

3.6 Conclusions

Newly acquired seismic reflection and swath bathymetry data in the Adare Basin and the adjacent Ross Sea shelf reveal three major tectonic events. Based on correlation of the Ross Sea seismic stratigraphy of Brancolini et al. (1995) (ANTOSTRAT) from the Northern Basin into the Adare Basin we deduce the following:

1. A pulse of discrete normal faulting took place shortly after the cessation of spreading. The event is located between the RSU6 and RSU5 unconformities, estimated at ~24 Ma. Faulting resulted in negligible extension (less than 2 km) and did not seem to extend outside the basin. Part of the eastern flank of the Adare Trough was uplifted during this event, probably reactivating a preexisting low-relief trough. We speculate that this phase of deformation resulted from the thermal relaxation of seafloor spreading that may have been linked with changes in the regional stress regime accompanying a reorganization of plate motion on the Pacific-Antarctic ridge.

2. A major localized early Miocene (between RSU4 and RSU4a, ~17 Ma) rifting event produced half grabens composed of west-tilted blocks and east-dipping normal faults that accommodated a total of 3-5 km of extension. Faulting resulted in the uplift of the western flank of the Adare Trough, and subsidence south and

southwest of the trough. The tilted blocks comprise an en-echelon structural array with an overall NE-SW direction that starts south of the Adare Trough and approaches Cape Adare. Faulting reached the shelf edge, indicating that this event was probably linked with tectonic activity outside the basin (most likely with faulting in the NVL, Faccenna et al. (2008)). We find no indication for major strike-slip motion in the Adare Basin.

No motion is observed in the VLB during this interval (Fielding et al., 2008), as expected given its proximity to the Eocene-Oligocene pole of rotation. Hence, we conclude that the pole of rotation between East and West Antarctica remained in the same location until (and including) the early Miocene. This event marks the last prominent extension activity in the Adare Basin.

3. Penetrating the entire sedimentary sequence, igneous activity and steep normal faults mark the youngest phase (Pliocene to present-day) of tectonic activity in the Adare Basin. Preliminary geochemical analyses of dredged basalts (Panter and Castillo, 2007), and the overall SW-NE spatial distribution of volcanic centers within and outside the Adare Basin indicate an intimate link to the Miocene volcanic activity found on land southwest of the basin. Steep normal faults produced prominent seafloor scarps but resulted in only a minor extensional component. At this stage, in terms of horizontal motion, the Adare Basin is nearly locked.

The lack of extension in the Adare Basin coeval with the middle Miocene opening of the Terror Rift (Fielding et al., 2008), on land Miocene normal faulting in the NVL sector (Faccenna et al., 2008), an extensional phase in the interior deep sub-ice troughs and basins (LeMasurier, 2008), and a northward age propagation of the initiation of volcanic activity suggests that the pole of rotation between East and West Antarctica might have relocated north of the Adare Basin (with an opposing sense of motion relative to the Eocene-Oligocene pole). This requires an important middle Miocene (17-13 Ma) change in the relative plate motion between East and West Antarctica. Finally, good temporal correlation between these tectonic events and the kinematic framework of the adjacent Antarctic-Pacific ridge provides an independent confirmation of the time frame presented here.

Lack of evidence for strike-slip faulting in our seismic reflection data confirms that no major NW-SE dextral strike-slip faulting took place in the Adare Basin during the Neogene.

3.7 Acknowledgments

We would like to thank Captain Watson, the crew, and the Raytheon staff of the R/VIB Nathaniel Palmer for their dedicated work during cruise NBP0701. Also, we thank Neal Driscoll, Donna Blackman, Jeff Gee for helpful discussions, Paul Henkart for the continuous help with SIOSEIS, and Chris Sorlein for introducing us to SPW software. Detlef Damaske is thanked for making the aeromagnetic data available for us. Interpretation of the seismic profiles was done with Kingdom Suite, a contribution of Seismic Micro-Technology. This project was funded by NSF grant OPP04-40959 (SIO) and OPP04-40923 (Caltech).

This chapter is being prepared for submission to *Geochemistry, Geophysics, Geosystems*, R. Granot, S. C. Cande, J. M. Stock, F. J. Davey, R. W. Clayton, Post-spreading rifting in the Adare Basin, Antarctica: Regional Tectonic Consequences. I processed, interpreted, and analyzed all of the seismic reflection data. I also picked the anomalies from the aeromagnetic dataset collected as part of GANOVEX IX 2005/06 (courtesy of Detlef Damaske). Principal investigators were Steve Cande and Joann Stock who also supervised this study. Fred Davey contributed to the seismic interpretation and general tectonic understanding. Rob Clayton helped processing the seismic data during the NBP0701 cruise.

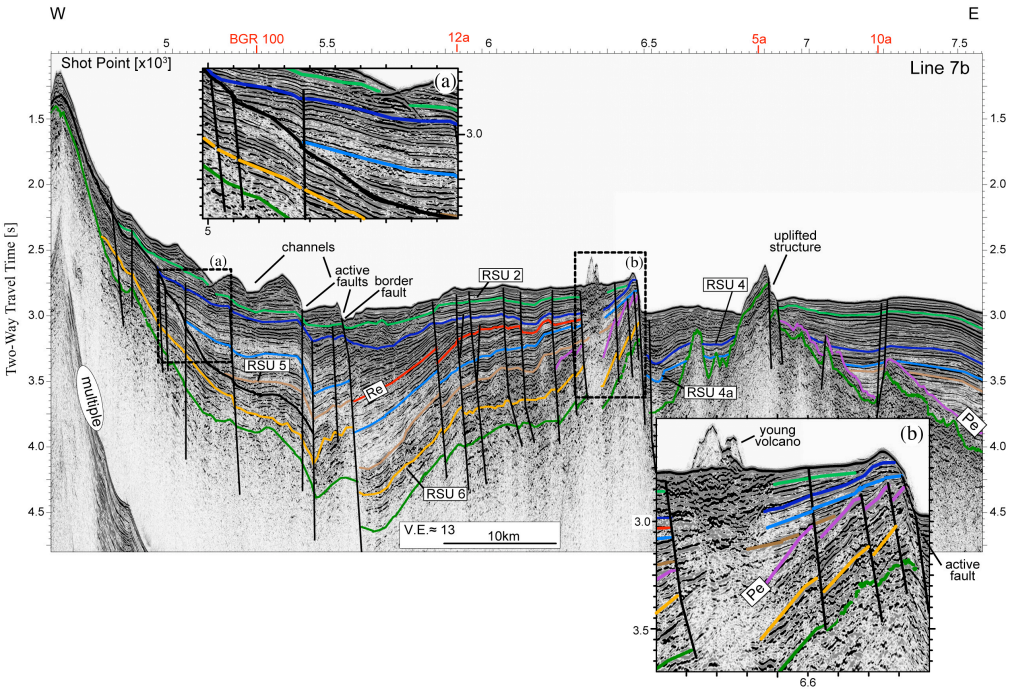

Figure 3.11: Line 7b crossing the center of the Adare Basin. This profile illustrates the three Neogene tectonic events of the Adare Basin. Evidence for early faulting (Purple event, Pe) is found across the entire profile (onset is marked by the purple unconformity). Additional major tilting event is found higher within the stratigraphic column (SPs 5500-5900, marked by red unconformity). Active volcanism, faulting, and the border fault are also pointed out. Inset (a) is a close-up showing an unconformity, marked by the thick black line, that separates eastward pinching out strata from an onlapping strata. This unconformity reflects a reorientation of deep water flow. Inset (b) is a close-up showing the tilting and faulting of the deep strata below the purple unconformity. The purple unconformity here marks an angular unconformity that resulted from tectonic tilting. Young volcanism and steep normal faulting is also evident.

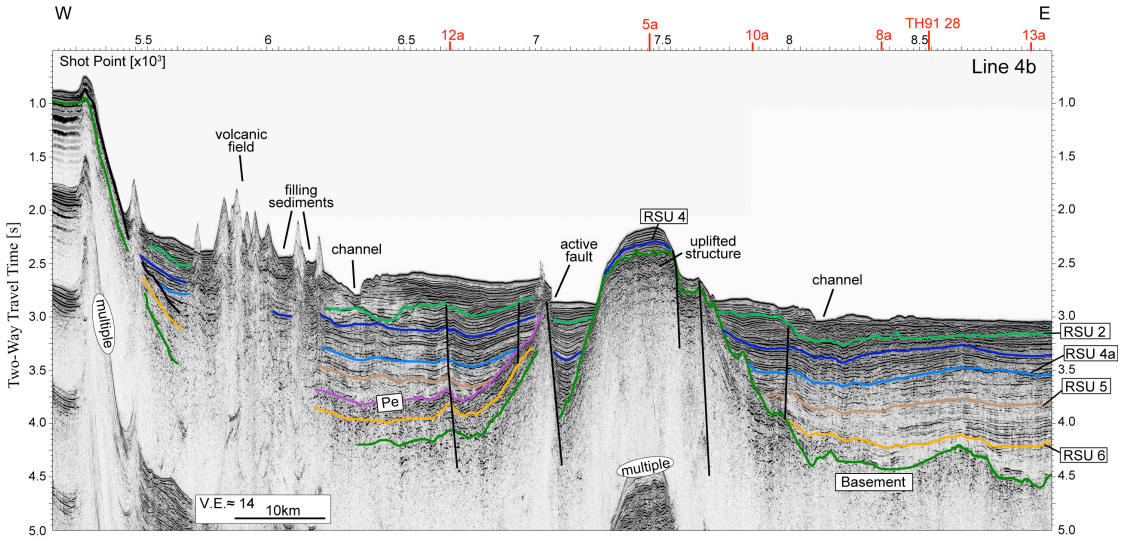

Figure 3.12: Line 4b crossing the southern Adare Basin. The purple unconformity can be traced across most of the basin while there are no indications for significant younger, Red event, faulting. Note the disappearance of RSU6 at the youngest-most part (i.e., center) of the basin. Young volcanism, channels, and uplifted structure are pointed out.

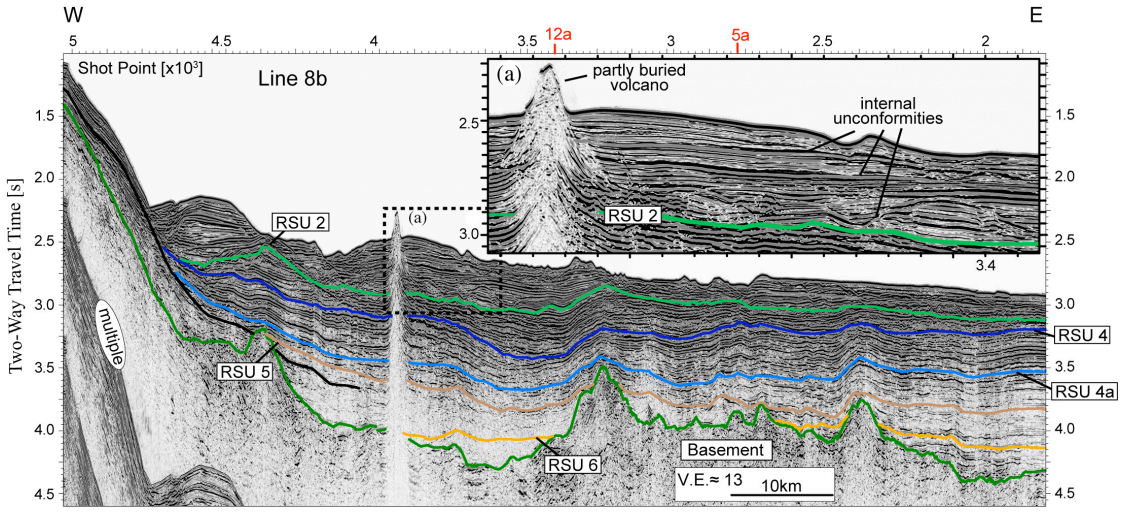

Figure 3.13: The southernmost crossing of the Adare Basin (Line 8b). Lack of faulting and continuous sub-horizontal reflectors indicate that post-spreading, Neogene, faulting found within the central and northern parts of the Adare Basin did not continue into the southern part of the basin and therefore into the central part of the Northern Basin. Inset (a) is a close-up of the Pliocene strata overlying RSU2 showing internal unconformities. Note that the volcano is partly buried under the Pliocene strata.

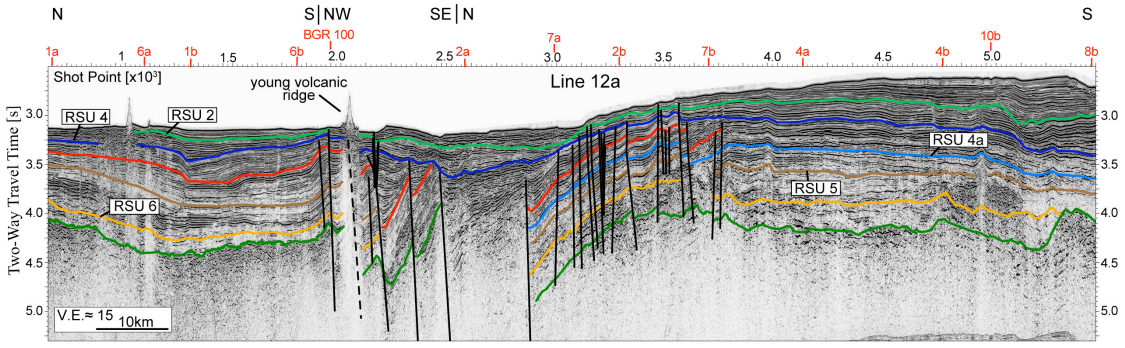

Figure 3.14: Line 12a, a N-S profile that runs along the western side of the basin. Note the localized zone of normal faulting and tilted blocks accompanied by depression (SPs 1900-3700). The red unconformity marks the initiation time of these structures.

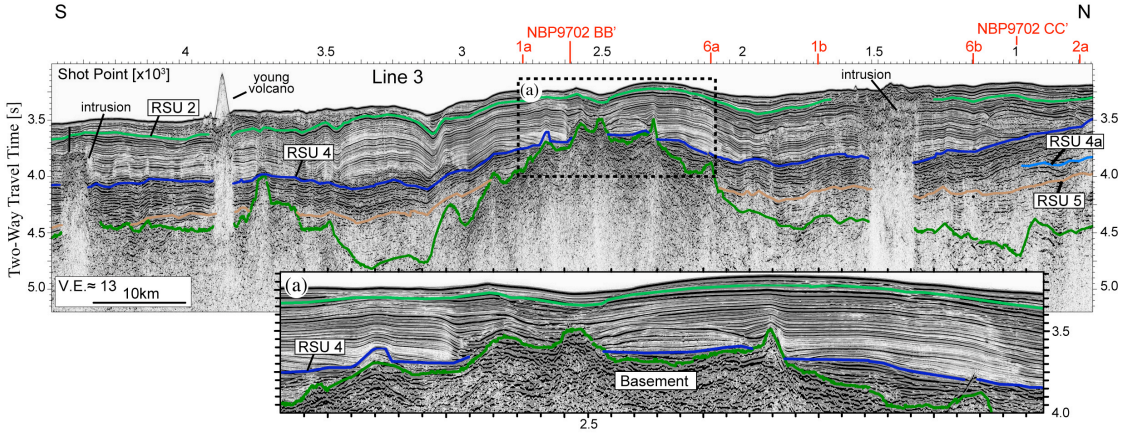

Figure 3.15: Line 3, a N-S profile located within the southern part of the Adare Trough. Inset (a) is a close-up showing the contrasting seismic properties of the seismic sequence across RSU4. Note the northward propagation of the seismic unit above RSU4.

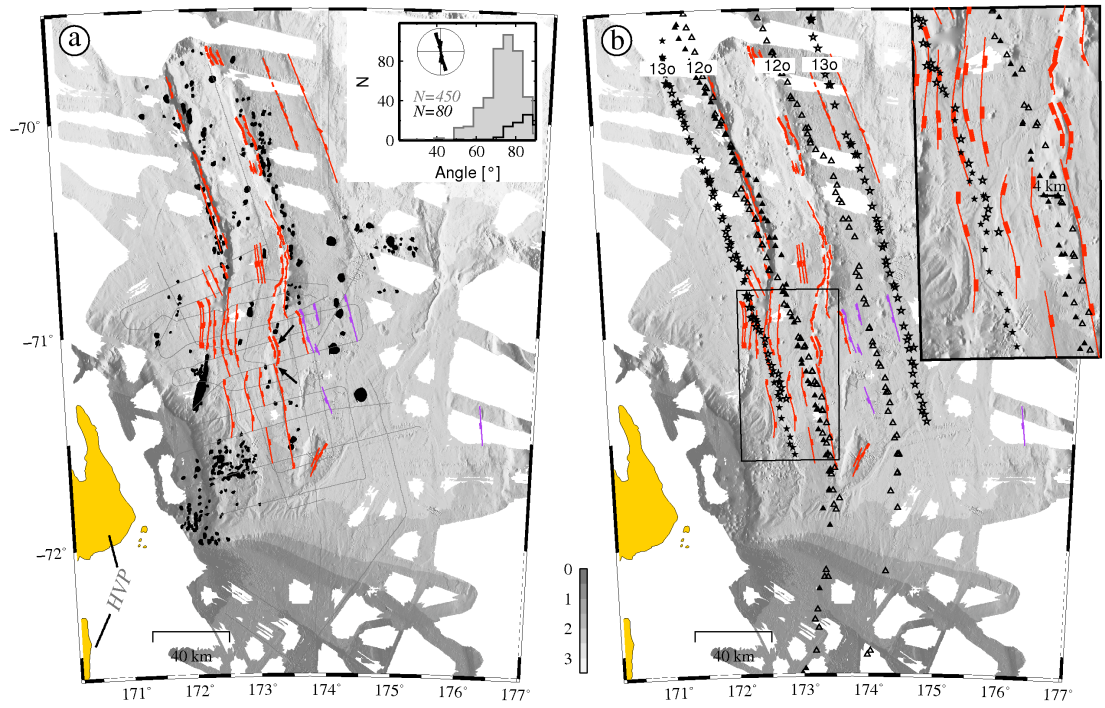

Figure 3.16: Summary maps showing the mapped faults, volcanic features, and magnetic anomaly picks. a) Structural map showing the faults that were interpreted on more than one seismic profile (red lines) and volcanic activity that reached the seafloor (black) mapped using a combination of seismic and multibeam bathymetry data. Purple faults were active only in the late Oligocene deformational event whereas red faults were active during the younger, early Miocene, faulting event. Rectangular tabs mark the downthrown sides of the faults. Inset shows histograms with the apparent dip of all 450 interpreted faults (gray), and black histogram shows the true dip of the 80 faults that were interpreted on more than one seismic line. Strikes of these 80 faults are shown in the rose diagram with the maximum radius representing 30 fault segments. Typical strike of faults in the Adare Basin is N10°W. The black arrows point toward the transfer ridge (north arrow) and accommodation zone (south arrow). b) Magnetic anomaly picks projected onto the structural map shown in Figure 3.15a. Anomalies 13o and 12o picks are shown with stars and triangles, respectively. Empty (shaded) are the unrotated (rotated) picks. Rotations were made using the East-West Antarctica anomaly 18o rotation pole of Davey et al. (2006), with rotation angles of 1.26° and 2.4° for anomalies 12o and 13o, respectively. These angles are constrained by the northern sections of the isochrons, presumed to be outside the deformed zone. The misfit between the rotated and unrotated anomalies in the deformed zone suggests that the total extensional, at the locations of the anomalies, could not have been larger than ~5 km.

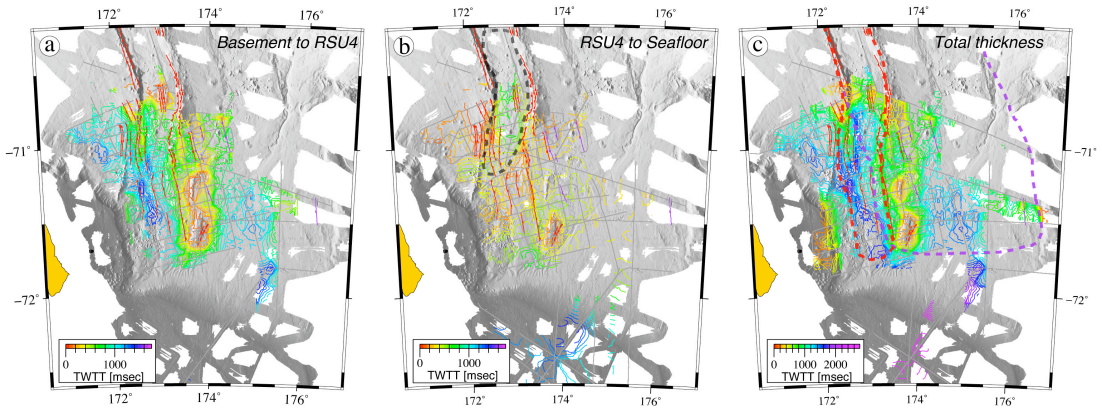

Figure 3.17: Isopach maps showing the cumulative thickness of the sedimentary packages from (a) basement to RSU4, (b) RSU4 to seafloor, and (c) total thickness. Also shown are the mapped faults. Contours (every 70 msec two-way travel time) were calculated based on an interpolated 1 km by 1 km grid of sediment thickness with a search radius of 16 km. Background (gray scale) shown is the bathymetry where multi-beam data available. Subsidence and fault-controlled sedimentation is apparent between the formation of the Adare Basin and RSU4. Younger sedimentation is controlled by the morphology of the basin (b). The dashed gray line denotes the spatial extent of the gravity-controlled facies, deposited above RSU4 (b). The spatial extent of the Purple and Red events are shown with dashed purple and red lines, respectively (c).

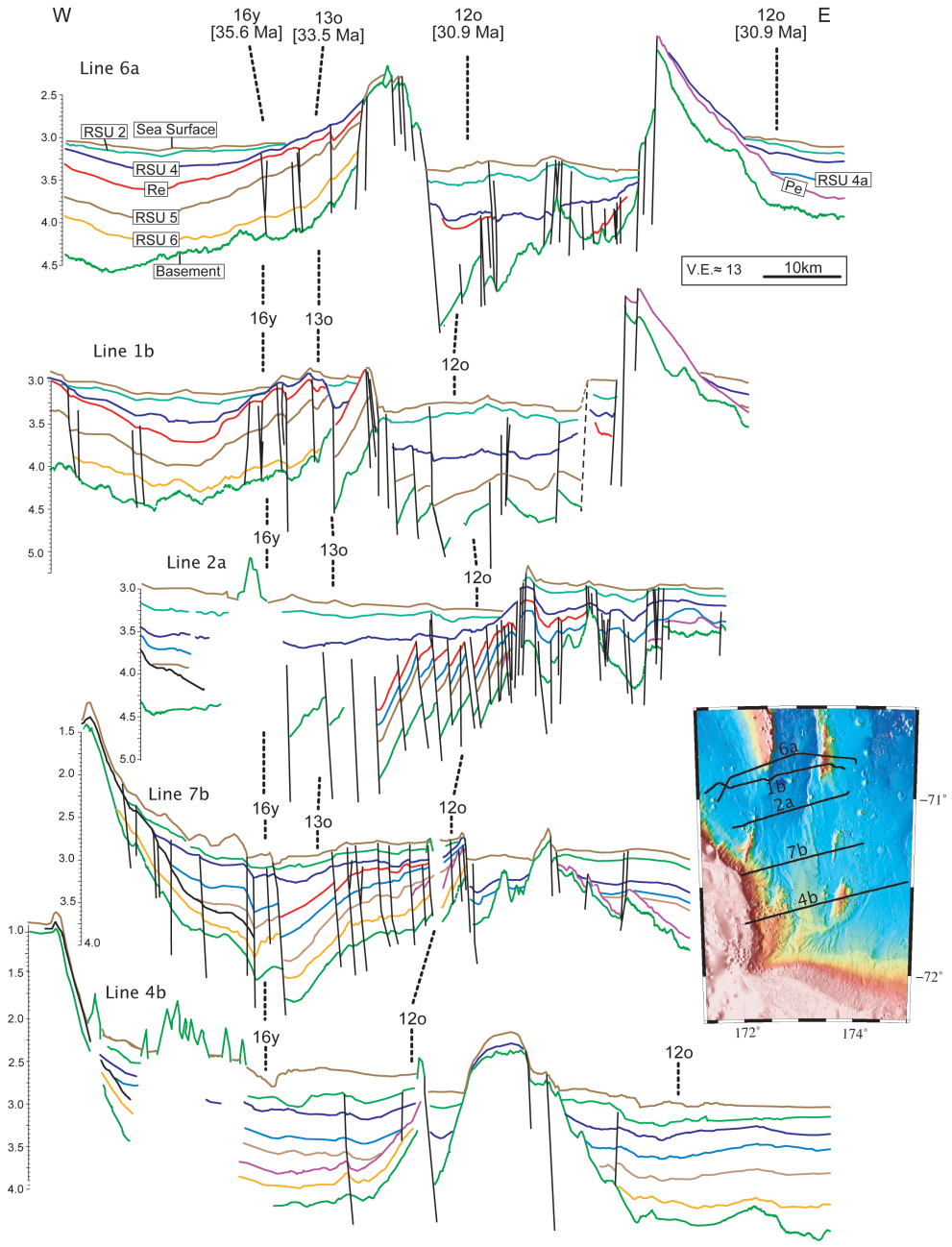

Figure 3.18: Schematic illustration of representative profiles ordered from north (top) to south (bottom) and horizontally aligned according to their crossings with anomaly 16y of the East Antarctic plate (35.6 Ma, Cande and Kent (1995)) that crosses along the western part of the Adare Basin. Note the westward spatial propagation of the lower Miocene rifting event (i.e., Red event) from north to south. Also, note the disappearance of prominent faulting toward the south-end of the Adare Basin. Inset map shows the location map of these profiles.

Bibliography

Anandakrishnan, S., and Winberry, J. P., 2004: Antarctic subglacial sedimentary layer thickness from receiver function analysis. *Global Planet. Change*, **42**(1-4), 167–176.

Atwater, T., Sclater, J., Sandwell, D., Severinghaus, J., and Marlow, M., 1993: *Fracture zone traces across the North Pacific Cretaceous Quiet Zone and their tectonic implications*, volume The Mesozoic Pacific: Geology, Tectonics, and Volcanism, Geophysical Monograph 77, 137–154. American Geophysical Union.

Bart, P. J., and Anderson, J. B., 2000: Relative temporal stability of the Antarctic ice sheets during the late Neogene based on the minimum frequency of outer shelf grounding events. *Earth Planet. Sci. Lett.*, **182**(3-4), 259–272.

Barth, G. A., 1994: Oceanic crust thickens approaching the Clipperton fracture zone. *Mar. Geophys. Res.*, **16**(1), 51–64.

Batiza, R., Niu, Y. L., Karsten, J. L., Boger, W., Potts, E., Norby, L., and Butler, R., 1996: Steady and non-steady state magma chambers below the East Pacific Rise. *Geophys. Res. Lett.*, **23**(3), 221–224.

Bazin, S., Harding, A. J., Kent, G. M., Orcutt, J. A., Tong, C. H., Pye, J. W., Singh, S. C., Barton, P. J., Sinha, M. C., White, R. S., Hobbs, R. W., and Van Avendonk, H. J. A., 2001: Three-dimensional shallow crustal emplacement at the 9°03'n overlapping spreading center on the East Pacific Rise: correlations between magnetization and tomographic images. *J. Geophys. Res.*, **106**(B8), 16101–16117.

Behrendt, J. C., Blankenship, D. D., Finn, C. A., Bell, R. E., Sweeney, R. E., Hodge, S. M., and Brozena, J. M., 1994: CASERTZ aeromagnetic data reveal late Ceonozoic flood basalts (?) in the West Antarctic rift system. *Geology*, **22**(6), 527–530.

Behrendt, J. C., and Cooper, A., 1991: Evidence of rapid Cenozoic uplift of the shoulder escarpment of the Cenozoic West Antarctic rift system and a speculation on possible climate forcing. *Geology*, **19**(4), 315–319.

Behrendt, J. C., Lemasurier, W. E., Cooper, A. K., Tessensohn, F., Trehu, A., and Damaske, D., 1991: Geophysical studies of the West Antarctic rift system. *Tectonics*, **10**(6), 1257–1273.

Blackman, D. K., Von Herzen, R. P., and Lawver, L. A., 1987: Heat flow and tectonics in the western Ross Sea, Antarctica. In *The Antarctic continental margin: geology and geophysics of the western Ross Sea*. Circum-Pacific Res. Council.

Bonatti, E., Ligi, M., Brunelli, D., Cipriani, A., Fabretti, P., Ferrante, V., Gasperini, L., and Ottolini, L., 2003: Mantle thermal pulses below the Mid-Atlantic Ridge and temporal variations in the formation of oceanic lithosphere. *Nature*, **423**(6939), 499–505.

Bowers, N. E., Cande, S. C., Gee, J. S., Hildebrand, J. A., and Parker, R. L., 2001: Fluctuations of the paleomagnetic field during chron C5 as recorded in near-bottom marine magnetic anomaly data. *J. Geophys. Res.*, **106**(B11), 26379–26396.

Brancolini, G., Cooper, A. K., and Coren, F., 1995: Seismic facies and glacial history in the western Ross Sea (Antarctica). In *Geology and Seismic Stratigraphy of the Antarctic Margin, Antarctic Research Series*, editors A. K. Cooper, P. F. Barker, and G. Brancolini, volume 68, 209–234. American Geophysical Union, Washinghton D. C.

Cande, S. C., and Kent, D. V., 1992: Ultrahigh resolution marine magnetic anomaly profiles: a record of continuous paleointensity variations? *J. Geophys. Res.*, **97**(B11), 15075–15083.

Cande, S. C., and Kent, D. V., 1995: Revised calibration of the geomagnetic polarity timescale for the Late Cretaceous and Cenozoic. *J. Geophys. Res.*, **100**(B4), 6093–6095.

Cande, S. C., Raymond, C. A., Stock, J., and Haxby, W. F., 1995: Geophysics of the Piman Fracture Zone and Pacific-Antarctic plate motions during the Cenozoic. *Science*, **270**(5238), 947–953.

Cande, S. C., and Stock, J. M., 2004a: Cenozoic reconstructions of the Australia-New Zealand-South Pacific sector of Antarctica. In *The Cenozoic Southern Ocean: Tectonics, Sedimentation and Climate Change Between Australia and Antarctica*, editors N. F. Exon, J. K. Kennett, and M. J. Malone, volume 151, 5–18. Geophysical Monograph Series, American Geophysical Union, Washinghton D. C.

Cande, S. C., and Stock, J. M., 2004b: Pacific-Antarctic-Australia motion and the formation of the Macquarie Plate. *Geophys. J. Int.*, **157**(1), 399–414.

Cande, S. C., and Stock, J. M., 2006: Constraints on the timing of extension in the Northern Basin, Ross Sea. In *Antarctica: Contributions to Global Earth Science*, editors D. Futterer, D. Damaske, G. Kleinschmidt, H. Miller, and F. Tessensohn, chapter 6.5, 319–326. Springer, New York.

Cande, S. C., Stock, J. M., Muller, R. D., and Ishihara, T., 2000: Cenozoic motion between East and West Antarctica. *Nature*, **404**(6774), 145–150.

Carbotte, S., and Macdonald, K., 1992: East Pacific Rise 8°-10°30'n: evolution of ridge segments and discontinuities from SeaMARC ii and three-dimensional magnetic studies. *J. Geophys. Res.*, **97**(B5), 6959–6982.

Carbotte, S. M., Small, C., and Donnelly, K., 2004: The influence of ridge migration on the magmatic segmentation of mid-ocean ridges. *Nature*, **429**(6993), 743–746.

Chen, Y. S., 1988: Thermal model of oceanic transform faults. *J. Geophys. Res.*, **93**(B8), 8839–8851.

Collete, S. M., Slootweg, A., Verhoef, J., and Roest, W., 1984: Geophysical investigations of the floor of the Atlantic-Ocean between 10° and 38°n (Kroonvlag Project). *Proc. Kon. Ned. Ak. Wet.*, **87**, 1–76.

Cooper, A. K., and Davey, F. J., 1985: Episodic rifting of Phanerozoic rocks in the Victoria Land Basin, western Ross Sea, Antarctica. *Science*, **229**(4718), 1085–1087.

Cooper, A. K., Davey, F. J., and Behrendt, J. C., 1987: Seismic stratigraphy and structures in the Victoria Land Basin, Western Ross Sea, Antarctica. In *The Antarctic continental margin: geology and geophysics of the western Ross Sea*, editors A. K. Cooper, and F. J. Davey, volume Earth Science Series Vol 5B, 27–76. Circum-Pacific Council for Energy and Mineral Resources.

Cronin, M., Tauxe, L., Constable, C., Selkin, P., and Pick, T., 2001: Noise in the quiet zone. *Earth Planet. Sci. Lett.*, **190**(1-2), 13–30.

Croon, M. B., Cande, S. C., and Stock, J. M., 2008: Revised Pacific-Antarctic plate motions and geophysics of the Menard Fracture Zone. *Geochem. Geophys. Geosyst.*, **9**. doi:10.1029/2008GC002019.

Damaske, D., Läufer, A. L., Goldmann, F., Möller, H. D., and Lisker, F., 2007: Magnetic anomalies north-east of Cape Adare, northern Victoria Land (Antarctica), and their relation to onshore structure. In *Antarctica: A Keystone in a Changing Wworld; Online Proceedings for the Tenth International Symposium on Antarctic Earth Sciences*, editors A. K. Cooper, and C. Raymond, USGS OF-2007-1047, Short Research Paper 016. U. S. Geological Survey. doi: 10.3133/of2007-1047.srp016.

Davey, F., and Sauli, C., 2007: Antarctic sedimentary basins: key to understanding glacial processes. *EOS*, **88**(39), 384–385.

Davey, F. J., and Brancolini, G., 1995: The late Mesozoic and Cenozoic structural setting of the Ross Sea region. In *Geology and Seismic Stratigraphy of the Antarctic Margin, Antarctic Research Series*, editors A. K. Cooper, P. F. Barker, and G. Brancolini, volume 68, 167–182. American Geophysical Union, Washinghton D. C.

Davey, F. J., Brancolini, G., Hamilton, R. J., Henrys, S. A., Sorlien, C. C., and Bartek, L. R., 2000: A revised correlation of the seismic stratigraphy at the Cape Roberts drill sites with the seismic stratigraphy of the Victoria Land Basin. *Terra Antarct.*, **7**(3), 215–220.

Davey, F. J., Cande, S. C., and Stock, J. M., 2006: Extension in the western Ross Sea region-links between Adare Basin and Victoria Land Basin. *Geophys. Res. Lett.*, **33**. doi:10.1029/2006GL027383.

Davey, F. J., and De Santis, L., 2006: A multi-phase rifting model for the Victoria Land Basin, western Ross Sea. In *Antarctica: Contributions to Global Earth Sciences*, editors D. Futterer, D. Damaske, G. Kleinschmidt, H. Miller, and F. Tessensohn, 303–308. Springer-Verlag, Berlin Heidelberg New York.

De Santis, L., Anderson, J. B., Brancolini, G., and Zayatz, I., 1995: Seismic record of late Oligocene through Miocene glaciation on the central and eastern continental shelf of the Ross Sea. In *Geology and Seismic Stratigraphy of the Antarctic Margin, Antarctic Research Series*, editors A. K. Cooper, P. F. Barker, and G. Brancolini, volume 68, 235–260. American Geophysical Union, Washinghton D. C.

Della Vedova, B., Pellis, G., Lawver, L. A., and Brancolini, G., 1991: Heatflow and tectonics of the western Ross Sea. In *Recent Progress in Antarctic Earth Science, Proceedings of the Sixth International Symposium on Antarctic Earth Science*, editors Y. Yoshida, K. Kaminuma, and K. Shiraishi, 627–637.

Detrick, R. S., and Lynn, W. S., 1975: Origin of high-amplitude magnetic anomalies at intersection of Juan de Fuca Ridge and Blanco Fracture Zone. *Earth Planet. Sci. Lett.*, **26**(1), 105–113.

Divenere, V. J., Kent, D. V., and Dalziel, I. W. D., 1994: Mid-Cretaceous paleomagnetic results from Marie Byrd Land, West Antarctica - a test of post 100 Ma relative motion between East and West Antarctica. *J. Geophys. Res.*, **99**(B8), 15115–15139.

Donnellan, A., and Luyendyk, B. P., 2004: GPS evidence for a coherent Antarctic plate and for postglacial rebound in Marie Byrd Land. *Global Planet. Change*, **42**(1-4), 305–311.

Dyment, J., ArkaniHamed, J., and Ghods, A., 1997: Contribution of serpentinized ultramafics to marine magnetic anomalies at slow and intermediate spreading centres: insights from the shape of the anomalies. *Geophys. J. Int.*, **129**(3), 691–701.

Emmermann, R., 1985: *Basement geochemistry, Hole 504B*, volume 69, 183–199. Init. Rep. Deep Sea Drill. Proj.

Faccenna, C., Rossetti, F., Becker, T. W. B., Danesi, S., and Morelli, A., 2008: Recent extension driven by mantle upwelling beneath the Admiralty Mountains (East Antarctica). *Tectonics*, **27**(4). doi:10.1029/2007TC002197.

Faugeres, J. C., Stow, D. A. V., Imbert, P., and Viana, A., 1999: Seismic features diagnostic of contourite drifts. *Mar. Geol.*, **162**(1), 1–38.

Ferraccioli, F., Armadillo, E., Zunino, A., Bozzo, E., Rocchi, S., and Armienti, P., 2008: Magmatic and tectonic patterns over the Northern Victoria Land sector of the Transantarctic Mountains from new aeromagnetic imaging. *Tectonophysics*. doi:10.1016/j.tecto.2008.11.028.

Fielding, C. R., Whittaker, J., Henrys, S. A., Wilson, T. J., and Naish, T. R., 2008: Seismic facies and stratigraphy of the Cenozoic succession in McMurdo Sound, Antarctica: implications for tectonic, climatic and glacial history. *Palaeogeogr. Palaeoclimatol. Palaeoecol.*, **260**(1-2), 8–29.

Fielding, R. C., Henrys, S. A., and Wilson, T. J., 2006: Rift history of the western Victoria Land Basin: a new perspective based on integration of cores with seismic reflection data. In *Antarctica: Contributions to Global Earth Sciences*, editors D. Futterer, D. Damaske, G. Kleinschmidt, H. Miller, and F. Tessensohn, 309–318. Springer-Verlag, Berlin Heidelberg New York.

Fitzgerald, P. G., Sandiford, M., Barrett, P. J., and Gleadow, A. J. W., 1986: Asymmetric extension associated with uplift and subsidence in the Transantarctic Mountains and Ross Embayment. *Earth Planet. Sci. Lett.*, **81**, 67–78.

Fitzgerald, P. G., and Stump, E., 1997: Cretaceous and Cenozoic episodic denudation of the Transantarctic Mountains, Antarctica: new constraints from apatite fission track thermochronology in the Scott Glacier region. *J. Geophys. Res.*, **102**(B4), 7747–7765.

Gee, J., and Kent, D. V., 1997: Magnetization of axial lavas from the southern East Pacific Rise (14°-23°s): geochemical controls on magnetic properties. *J. Geophys. Res.*, **102**(B11), 24873–24886.

Gee, J. S., and Kent, D. V., 2007: *Treatise on Geophysics, Vol. 5*, chapter Source of oceanic magnetic anomalies and the geomagnetic polarity timescale, 455–507. Elsevier.

Glatzmaier, G. A., Coe, R. S., Hongre, L., and Roberts, P. H., 1999: The role of the Earth's mantle in controlling the frequency of geomagnetic reversals. *Nature*, **401**(6756), 885–890.

Gleadow, A. J. W., and Fitzgerald, P. G., 1987: Uplift history and structure of the Transantarctic Mountains: new evidence from fission track dating of basement apatites in the Dry Valleys area, southern Victoria Land. *Earth Planet. Sci. Lett.*, **82**(1-2), 1–14.

Granot, R., Tauxe, L., Gee, J. S., and Ron, H., 2007: A view into the Cretaceous geomagnetic field from analysis of gabbros and submarine glasses. *Earth Planet. Sci. Lett.*, **256**(1-2), 1–11.

Gregg, P. M., Lin, J., Behn, M. D., and Montesi, L. G. J., 2007: Spreading rate dependence of gravity anomalies along oceanic transform faults. *Nature*, **448**(7150), 183–188.

Hall, C. E., and Gurnis, M., 2005: Strength of fracture zones from their bathymetric and gravitational evolution. *J. Geophys. Res.*, **110**(B1). doi: 10.1029/2004jb003312.

Hall, J., Wilson, T., and Henrys, S., 2007: Structure of the central Terror Rift, western Ross Sea, Antarctica. In *Antarctica: A Keystone in a Changing Wworld; Online Proceedings for the Tenth International Symposium on Antarctic Earth Sciences*, editors A. K. Cooper, and C. Raymond, USGS OF-2007-1047, Short Research Paper 108. U. S. Geological Survey. doi:10.3133/of2007-1047.srp108.

Hampson, D., 1986: Inverse velocity stacking for multiple elimination. *J. Canadian Soc. Explor. Geophys.*, **22**(1), 44—55.

Hansen, D. M., and Cartwright, J., 2006: The three-dimensional geometry and growth of forced folds above saucer-shaped igneous sills. *J. Struc. Geol.*, **28**(8), 1,520–1,535.

Hayes, D. E., and Frakes, L. A., 1975: General synthesis, Deep Sea drilling project Leg 28. *Init. Rep. Deep Sea Drill. Proj.*, **28**, 919–942. doi: 10.2973/dsdp.proc.28.136.1975.

Hayes, D. E., Frakes, L. A., Barrett, P. J., Burns, D. A., Chen, P., Ford, A. B., Kaneps, A., Kemp, E. M., McCollum, D. W., Piper, D. J. W., Wall, R. E., and Webb, P. N., 1975a: Site 273. *Init. Rep. Deep Sea Drill. Proj.*, **28**, 335–367. doi:10.2973/dsdp.proc.28.109.1975.

Hayes, D. E., Frakes, L. A., Barrett, P. J., Burns, D. A., Chen, P., Ford, A. B., Kaneps, A., Kemp, E. M., McCollum, D. W., Piper, D. J. W., Wall, R. E., and Webb, P. N., 1975b: Site 274. *Init. Rep. Deep Sea Drill. Proj.*, **28**, 369–433. doi:10.2973/dsdp.proc.28.110.1975.

He, H. Y., Pan, Y. X., Tauxe, L., Qin, H. F., and Zhu, R. X., 2008: Toward age determination of the M0r (Barremian-Aptian boundary) of the Early Cretaceous. *Phys. Earth Planet. Inter.*, **169**(1-4), 41–48.

Heimann, A., Fleming, T., Elliot, D., and Foland, K., 1994: A short interval of Jurassic continental flood-basalt volcanism in Antarctica as demonstrated by $^{40}Ar/^{39}Ar$ geochronology. *Earth Planet. Sci. Lett.*, **121**(1-2), 19–41.

Heller, P. L., Anderson, D. L., and Angevine, C. L., 1996: Is the middle Cretaceous pulse of rapid sea-floor spreading real or necessary? *Geology*, **24**(6), 491–494.

Henrys, S., Wilson, T., Whittaker, J. M., Fielding, C., Hall, J., and Naish, T., 2007: Tectonic history of mid-Miocene to present southern Victoria Land Basin, inferred from seismic stratigraphy in McMurdo Sound, Antarctica. In *Antarctica: A Keystone in a Changing Wworld; Online Proceedings for the Tenth International Symposium on Antarctic Earth Sciences*, editors A. K. Cooper, and C. Raymond, USGS OF-2007-1047, Short Research Paper 049. U. S. Geological Survey. doi:10.3133/of2007-1047.srp049.

Hosford, A., Tivey, M., Matsumoto, T., Dick, H., Schouten, H., and Kinoshita, H., 2003: Crustal magnetization and accretion at the Southwest Indian Ridge near the Atlantis ii fracture zone, 0-25 Ma. *J. Geophys. Res.*, **108**(B3). doi: 10.1029/2001JB000604.

Huerta, A. D., and Harry, D. L., 2007: The transition from diffuse to focused extension: modeled evolution of the West Antarctic rift system. *Earth Planet. Sci. Lett.*, **255**(1-2), 133–147.

Johnston, L., Wilson, G. S., Gorman, A. R., Henrys, S. A., Horgan, H., Clark, R., and Naish, T. R., 2008: Cenozoic basin evolution beneath the southern McMurdo Ice Shelf, Antarctica. *Global Planet. Change*, **62**(1-2), 61–76.

Keller, W. R., 2004: *Cenozoic plate tectonic reconstructions and plate boundary processes in the Southwest Pacific.* Ph.D. thesis, Calif. Inst. of Technol., Pasadena, Calif.

Langmuir, C. H., and Bender, J. F., 1984: The geochemistry of oceanic basalts in the vicinity of transform faults: observations and implications. *Earth Planet. Sci. Lett.*, **69**(1), 107–127.

Langmuir, C. H., Bender, J. F., and Batiza, R., 1986: Petrological and tectonic segmentation of the East Pacific Rise, 5°30'-14°30' n. *Nature*, **322**(6078), 422–429.

LeMasurier, W. E., 1990: Late Cenozoic volcanism on the Antarctic Plate; an overview: volcanoes of the Antarctic Plate and southern oceans. In *Antarctic*

Research Series, editors W. E. LeMasurier, J. W. Thomson, and P. E. Bakeret, 1–17. American Geophysical Union, Washinghton D. C.

LeMasurier, W. E., 2008: Neogene extension and basin deepening in the West Antarctic rift inferred from comparisons with the East African rift and other analogs. *Geology*, **36**(3), 247–250.

Luyendyk, B., Cisowski, S., Smith, C., Richard, S., and Kimbrough, D., 1996: Paleomagnetic study of the northern Ford Ranges, western Marie Byrd Land, West Antarctica: motion between West and East Antarctica. *Tectonics*, **15**(1), 122–141.

Lythe, M. B., and Vaughan, D. G., 2001: BEDMAP: a new ice thickness and subglacial topographic model of Antarctica. *J. Geophys. Res.*, **106**(B6), 11335–11351.

Macdonald, K. C., Fox, P. J., Perram, L. J., Eisen, M. F., Haymon, R. M., Miller, S. P., Carbotte, S. M., Cormier, M. H., and Shor, A. N., 1988: A new view of the mid-ocean ridge from the behavior of ridge-axis discontinuities. *Nature*, **335**(6187), 217–225.

Macmillan, S., and Maus, S., 2005: International geomagnetic reference field - the tenth generation. *Earth Planet. Space*, **57**(12), 1135–1140.

Manley, P. L., and Flood, R. D., 1988: Cyclic sediment deposition within the Amazon Deep-sea Fan. *Am. Assoc. Pet. Geol. Bull.*, **72**(8), 912–925.

Massell, C., Coffin, M., Mann, P., Mosher, S., Frohlich, C., Duncan, C., Karner, G., Ramsay, D., and Lebrun, J., 2000: Neotectonics of the Macquarie Ridge Complex, Australia-Pacific plate boundary. *J. Geophys. Res.*, **105**(B6), 13457–13480.

Menard, H. W., and Atwater, T., 1969: Origin of fracture zone topography. *Nature*, **222**(5198), 1037–1040.

Molnar, P., Atwater, T., Mammerickx, J., and Smith, S., 1975: Magnetic anomalies, bathymetry and the tectonic evolution of the South Pacific since the late Cretaceous. *Geophys. J. R. Astron. Soc.*, **40**, 383–420.

Morgan, J. P., and Parmentier, E. M., 1984: Lithospheric stress near a ridge-transform intersection. *Geophys. Res. Lett.*, **11**(2), 113–116.

Mortimer, N., Dunlap, W. J., Isaac, M. J., Sutherland, R. P., and Faure, K., 2007: Basal Adare volcanics, Robertson Bay, North Victoria Land, Antarctica: late Miocene intraplate basalts of subaqueous origin. In *Antarctica: A Keystone in a Changing Wworld; Online Proceedings for the Tenth International Symposium*

on Antarctic Earth Sciences, editors A. K. Cooper, and C. Raymond, USGS OF-2007-1047, Short Research Paper 016. U. S. Geological Survey.

Muller, R. D., Cande, S. C., Stock, J. M., and Keller, W. R., 2005: Crustal structure and rift flank uplift of the Adare Trough, Antarctica. *Geochem. Geophys. Geosyst.*, **6**. doi:10.1029/2005GC001027.

Muller, R. D., Gohl, K., Cande, S. C., Goncharov, A., and Golynsky, A. V., 2007: Eocene to Miocene geometry of the West Antarctic rift system. *Australian J. Earth Sci.*, **54**(8), 1033–1045. doi:10.1080/08120090701615691.

Nardini, I., Armienti, P., Rocchi, S., and Burgess, R., 2003: $^{40}Ar/^{39}Ar$ chronolgy and petrology of the Miocene rift-related volcanism of the Daniell Peninsula (northern Victoria Land, Antarctica). *Terra Antarct.*, **10**(1), 39–62.

Panter, K. S., and Castillo, P., 2007: Petrogenesis and source of lavas from seamounts in the Adare Basin, western Ross Sea: implications for the origin of Cenozoic magmatism in Antarctica. In *Antarctica: A Keystone in a Changing Wworld; Online Proceedings for the Tenth International Symposium on Antarctic Earth Sciences*, editors A. K. Cooper, and C. Raymond, USGS OF-2007-1047, Short Research Paper 069. U. S. Geological Survey.

Panter, K. S., and Castillo, P., 2008: Petrology and source of lavas from seamounts in the Adare Basin, Western Ross Sea: implications for the origin of Cenozoic magmatism in Antarctica. *89(53), Fall Meet. Suppl., Abstract V11F-05.*

Parker, R. L., and Huestis, S. P., 1974: Inversion of magnetic anomalies in presence of topography. *J. Geophys. Res.*, **79**(11), 1587–1593.

Pick, T., and Tauxe, L., 1993: Geomagnetic palaeointensities during the Cretaceous normal superchron measured using submarine basaltic glass. *Nature*, **366**(6452), 238–242.

Pockalny, R. A., Smith, A., and Gente, P., 1995: Spatial and temporal variability of crustal magnetization of a slowly spreading ridge: Mid-Atlantic ridge (20°-24° n). *Mar. Geophys. Res.*, **17**(3), 301–320.

Rea, D. K., and Dixon, J. M., 1983: Late Cretaceous and Paleogene tectonic evolution of the North Pacific Ocean. *Earth Planet. Sci. Lett.*, **65**(1), 145–166.

Riisager, P., Riisager, J., Zhao, X. X., and Coe, R. S., 2003: Cretaceous geomagnetic paleointensities: Thellier experiments on pillow lavas and submarine basaltic glass from the Ontong Java Plateau. *Geochem. Geophys. Geosyst.*, **4**. doi:10.1029/2003gc000611.

Rossetti, F., Storti, F., Busetti, M., Lisker, F., Di Vincenzo, G., Laufer, A. L., Rocchi, S., and Salvini, F., 2006: Eocene initiation of Ross Sea dextral faulting and implications for East Antarctic neotectonics. *J. Geol. Soc. Lon.*, **163**, 119–126.

Rubin, K. H., and Sinton, J. M., 2007: Inferences on mid-ocean ridge thermal and magmatic structure from MORB compositions. *Earth Planet. Sci. Lett.*, **260**(1-2), 257–276.

Ryan, D. A., and Sarson, G. R., 2007: Are geomagnetic field reversals controlled by turbulence within the Earth's core? *Geophys. Res. Lett.*, **34**(2). doi:10.1029/2006gl028291.

Salvini, F., Brancolini, G., Busetti, M., Storti, F., Mazzarini, F., and Coren, F., 1997: Cenozoic geodynamics of the Ross Sea region, Antarctica: crustal extension, intraplate strike-slip faulting, and tectonic inheritance. *J. Geophys. Res.*, **102**(B11), 24669–24696.

Sandwell, D. T., 1984: Thermomechanical evolution of oceanic fracture zones. *J. Geophys. Res.*, **89**(B13), 1401–1413.

Sandwell, D. T., and Smith, W. H. F., 1997: Marine gravity anomaly from geosat and ERS 1 satellite altimetry. *J. Geophys. Res.*, **102**(B5), 10039–10054.

Savage, M. L., and Ciesielski, P. F., 1983: A revised history of glacial sedimentation in the Ross region. In *Antarctic Earth Science*, editors R. L. Oliver, P. R. James, and J. B. Jago, 555–559. Cambridge University Press, Cambridge.

Selkin, P. A., and Tauxe, L., 2000: Long-term variations in palaeointensity. *Philos. Trans. R. Soc. Lond. A*, **358**(1768), 1065–1088.

Sempere, J. C., 1991: High-magnetization zones near spreading center discontinuities. *Earth Planet. Sci. Lett.*, **107**(2), 389–405.

Siddoway, C. S., Baldwin, S. L., Fitzgerald, P. G., Fanning, C. M., and Luyendyk, B. P., 2004: Ross Sea mylonites and the timing of intracontinental extension within the West Antarctic rift system. *Geology*, **32**(1), 57–60.

Sinton, J. M., Smaglick, S. M., Mahoney, J. J., and Macdonald, K. C., 1991: Magmatic processes at superfast spreading mid-ocean ridges: glass compositional variations along the East Pacific Rise 13 °-23 °s. *J. Geophys. Res.*, **96**(B4), 6133–6155.

Sinton, J. M., Wilson, D. S., Christie, D. M., Hey, R. N., and Delaney, J. R., 1983: Petrologic consequences of rift propagation on oceanic spreading ridges. *Earth Planet. Sci. Lett.*, **62**(2), 193–207.

Steckler, M. S., 1985: Uplift and extension at the Gulf of Suez: indications of induced mantle convection. *Nature*, **317**(6033), 135–139.

Storti, F., Rossetti, F., Laufer, A. L., and Salvini, F., 2006: Consistent kinematic architecture in the damage zones of intraplate strike-slip fault systems in North Victoria Land, Antarctica and implications for fault zone evolution. *J. Struc. Geol.*, **28**(1), 50–63.

Storti, F., Salvini, F., Rossetti, F., and Morgan, J. P., 2007: Intraplate termination of transform faulting within the Antarctic continent. *Earth Planet. Sci. Lett.*, **260**(1-2), 115–126.

Sutherland, R., 1995: The Australia-Pacific boundary and Cenozoic plate motions in the SW Pacific: some constraints from Geosat data. *Tectonics*, **14**(4), 819–831.

Tarduno, J. A., and Cottrell, R. D., 2005: Dipole strength and variation of the time-averaged reversing and nonreversing geodynamo based on Thellier analyses of single plagioclase crystals. *J. Geophys. Res.*, **110**(B11). doi: 10.1029/2005jb003970.

Tarduno, J. A., Cottrell, R. D., and Smirnov, A. V., 2001: High geomagnetic intensity during the Mid-Cretaceous from Thellier analyses of single plagioclase crystals. *Science*, **291**(5509), 1779–1783.

Tarduno, J. A., Cottrell, R. D., and Smirnov, A. V., 2006: The paleomagnetism of single silicate crystals: recording geomagnetic field strength during mixed polarity intervals, superchrons, and inner core growth. *Rev. Geophys.*, **44**(1). doi:10.1029/2005rg000189.

Tauxe, L., 2006: Long-term trends in paleointensity: the contribution of DSDP/ODP submarine basaltic glass collections. *Phys. Earth Planet. Inter.*, **156**(3-4), 223–241.

Teagle, D. A. H., Alt, J. C., Umino, S., Miyashita, S., Banerjee, N. R., Wilson, D. S., and Scientists, E. ., 2006: Expedition 309/312 summary. *Proc. IODP*, **309/312**, 1–127.

ten Brink, U. S., Hackney, R. I., Bannister, S., Stern, T. A., and Makovsky, Y., 1997: Uplift of the Transantarctic Mountains and the bedrock beneath the East Antarctic ice sheet. *J. Geophys. Res.*, **102**(B12), 27603–27621.

Tivey, M. A., and Tucholke, B. E., 1998: Magnetization of 0-29 Ma ocean crust on the Mid-Atlantic Ridge, 25°30' to 27°10'n. *J. Geophys. Res.*, **103**(B8), 17807–17826.

Toomey, D. R., Jousselin, D., Dunn, R. A., Wilcock, W. S. D., and Detrick, R. S., 2007: Skew of mantle upwelling beneath the East Pacific Rise governs segmentation. *Nature*, **446**(7134), 409–414.

Truswell, E. M., and Drewry, D. J., 1984: Distribution and provenance of recycled palynomorphs in surficial sediments of the Ross Sea, Antarctica. *Mar. Geol.*, **59**(1-4), 187–214.

Twigt, W., Verhoef, J., Rohr, K., Mulder, T. F. A., and Collette, B. J., 1983: Topography, magnetics and gravity over the Kane Fracture Zone in the Cretaceous Magnetic Quiet Zone (African Plate). In *Proc. Kon. Ned. Ak. Wet.*, volume 86, 181–210.

Twiss, R. J., and Moores, E. M., 1992: *Structural Geology*. Freeman, New York.

Ulmer, P., and Trommsdorff, V., 1995: Serpentine stability to mantle depths and subduction-related magmatism. *Science*, **268**(5212), 858–861.

Van der Wateren, F. M., and Cloetingh, S. A. P. L., 1999: Feedbacks of lithosphere dynamics and environmental change of the Cenozoic West Antarctic rift system. *Global Planet. Change*, **23**(1-4), 1–24.

Van der Wateren, F. M., Dunai, T. J., Van Balen, R. T., Klas, W., Verbers, A. L. L. M., Passchier, S., and Herpers, U., 1999: Contrasting Neogene denudation histories of different structural regions in the Transantarctic Mountains rift flank constrained by cosmogenic isotope measurements. *Global Planet. Change*, **23**(1-4), 145–172.

Vogt, P. R., and Byerly, G. R., 1976: Magnetic anomalies and basalt composition in Juan de Fuca-Gorda Ridge area. *Earth Planet. Sci. Lett.*, **33**(2), 185–207.

Vogt, P. R., and Johnson, G. L., 1973: Magnetic telechemistry of oceanic crust. *Nature*, **245**(5425), 373–375.

Watson, T., Nyblade, A., Wiens, D. A., Anandakrishnan, S., Benoit, M., Shore, P. J., Voigt, D., and Vandecar, J., 2006: P and S velocity structure of the upper mantle beneath the Transantarctic Mountains, East Antarctic craton, and Ross Sea from travel time tomography. *Geochem. Geophys. Geosyst.*, **7**(7). doi:10.1029/2005GC001238.

Wessel, P., and Kroenke, L. W., 2008: Pacific absolute plate motion since 145 Ma: an assessment of the fixed hot spot hypothesis. *J. Geophys. Res.*, **113**(B6). doi:10.1029/2007JB005499.

Wessel, P., and Smith, W. H. F., 1998: New, improved version of the generic mapping tools released. *EOS, Trans. AGU*, **79**, 579. doi:10.1029/98EO00426.

Whittaker, J. M., and Muller, R. D., 2006: Seismic stratigraphy of the Adare Trough area, Antarctica. *Mar. Geol.*, **230**(3-4), 179–197.

Wilson, G. S., Bohaty, S., Fielding, C. F., Florindo, F., Hannah, M. J., Harwood, D. M., McIntosh, W., Naish, T. R., Robertson, A. P., Sagnotti, L., Scherer, R. P., Strong, C. P., Verosub, K. L., Villa, G., Watkins, D. K., Webb, P. N., and Woolfe, K. J., 2000: Chronostratigraphy of CRP 2/2A, Victoria Land Basin, Antarctica. *Terra Antarct.*, **7**, 647–654.

Wilson, T. J., 1995: Cenozoic transtension along the Transantarctic Mountains West Antarctic rift boundary, southern Victoria Land, Antarctica. *Tectonics*, **14**(2), 531–545.

Zanutta, A., Vittuari, L., and Gandolfi, S., 2008: Geodetic gps-based analysis of recent crustal motions in victoria land (Antarctica). *Global Planet. Change*, **62**(1-2), 115–131.

Zhao, X. X., Riisager, P., Riisager, J., Draeger, U., Coe, R. S., and Zheng, Z., 2004: New palaeointensity results from Cretaceous basalt of Inner Mongolia, China. *Phys. Earth Planet. Inter.*, **141**(2), 131–140.

Zhu, R. X., Pan, Y. X., He, H. Y., Qin, H. F., and Ren, S. M., 2008: Palaeomagnetism and $^{40}Ar/^{39}Ar$ age from a Cretaceous volcanic sequence, Inner Mongolia, China: implications for the field variation during the Cretaceous normal superchron. *Phys. Earth Planet. Inter.*, **169**(1-4), 59–75.